TAKING THE TWINKLE OUT OF THE STARS: An Adaptive Wavefront Tilt Correction Servo and Preliminary Seeing Study for SUSI.

Thesis submitted for the degree of
Doctor of Philosophy

by

Theo ten Brummelaar

Chatterton Astronomy Department
University of Sydney
Australia

Contents

ABSTRACT

The Sydney University Stellar Interferometer (SUSI) at Narrabri N.S.W. operates at optical wavelengths and has a baseline of up to 640m. In order to form fringes with this instrument the distortion introduced into the wavefront by the atmosphere must be corrected. In SUSI this is done by restricting the aperture to r_0 or less, thereby sampling a basically flat but tilted wavefront. Adaptive optics are then used to adjust for angle of arrival.

The tilt correction servo consists of a 'pyramid' detector system and piezoelectrically controlled tilt mirrors. With a sample frequency of 1000 Hz the system measures image position and re-centres the star image. The system holds the two beams of the interferometer parallel with a standard deviation of 0.164 ± 0.025 arcseconds which, with an aperture size of 0.06 metres, implies less than a 2% loss in the visibility measurements made by SUSI. The system has been used up to magnitude 6.5 stars and is predicted to have a limiting magnitude of 7.5 and possibly as high as 8.5.

By investigating the mirror positions required to centre the image a direct measurement of the first order Zernike polynomial expansion of the wavefront is obtained. Using this data it is possible to investigate atmospheric turbulence theory, and in particular the tilt power spectra. The system therefore not only corrects for the tilt introduced by the atmosphere but will supply a good estimate of seeing conditions using the same optical path through the atmosphere as the visibility measurements of the interferometer.

A preliminary investigation of seeing at the Narrabri site was undertaken, resulting in a median r_0 value of $7.1 \stackrel{\times}{\div} 1.3$cm at a wavelength of 500nm. This value is consistent with similar seeing studies on other observatory sites. As well as collecting this seeing data, predictions based on Kolmogorov turbulence for the power spectra and behaviour of wavefront tilt were tested and confirmed.

DECLARATION OF ORIGINALITY

To the best of my knowledge, this thesis contains no copy or paraphrase of work due to any other person, except where duly acknowledged. None of the work has been presented for any degree at the University of Sydney or elsewhere.

Theo ten Brummelaar

PUBLICATIONS

Some of the material in this thesis is based on the following publications:

- ten Brummelaar, T., "An Active Wavefront Tilt Correction Servo for SUSI", *Proceedings: High Resolution Imaging by Interferometry II*, **Ed: F. Merkle**, E.S.O. (Garching), in press.
- Davis, J., Tango, W.J., Booth, A.J., Minard, R.A., ten Brummelaar, T. and Shobbrook, R.R., "An Update on SUSI", *Proceedings: High Resolution Imaging by Interferometry II*, **Ed: F. Merkle**, E.S.O. (Garching), in press.

ACKNOWLEDGEMENTS

This thesis would never have been finished if not for the support and encouragement offered to me by my family, friends and the members of the Chatterton Astronomy department. There are too many people to give a complete list, however, there are some names that I must mention here.

I gratefully acknowledge the support of a Commonwealth Postgraduate Scholarship, my parents and my wife who, between them, supported me during the time it took to write this thesis. The SUSI project is funded jointly by the Australian Research Council and the University of Sydney. The support of the Pollock Memorial Fund and the Science Foundation for Physics within the University of Sydney is also gratefully acknowledged.

Thanks are due to my supervisor Dr. W.J. Tango, who built the original prototype tilt servo and offered advice and friendship throughout my time within the department. Stephen Owens and Hank Bennis helped a great deal with the design and construction of the electronics while Dr. A.J. Booth and Dr. R.A. Minard aided in software development. Some of the other people roped into the project were; Prof. J. Davis and Dr. R.R. Shobbrook, who collected some data in Narrabri, Peter Krockenberger and Sallie Cruise, who did the proof reading and Mel Broe, who took the photographs.

This thesis would have been much more difficult to complete if not for the efficient and reliable computer network set up and administered by David Dawes. I must also thank my two 'room mates' Michael Hrynevych and Peter Lawson, who were sometimes the only people left who were willing to talk about the thesis or, at least, offer a good reason to go to the 'Duck and Swan'. Finally I should acknowledge the staff of the Australia Telescope National Facility in Narrabri, who were always friendly and helpful and who provided excellent accommodation and entertainment.

List of Figures

List of Tables

Chapter 1

INTRODUCTION

The effects of the atmosphere on astronomical seeing have been documented since the time of the ancient Greeks; scintillation was a phenomenon mentioned by Aristotle in his treatise on 'The Heavens'. As soon as the telescope was invented, the variable appearance of stars and planets was of great concern. Newton, in his treatise on optics (Newton (1730 (Re-printed 1952)), Book I, Part I, Prop VIII) wrote:

If the theory of making Telescopes could at length be fully brought into Practice, yet there would be certain Bounds beyond which Telescopes could not perform. For the Air through which we look upon the Stars, is in perpetual Tremor ... The only Remedy is a most serene and quiet Air, as may perhaps be found on the tops of the highest Mountains above the grosser Clouds.

Newton also goes on to point out that the time scale of these 'trembling motions' is beyond the time response of the human eye and observes that differences in behaviour exist between large and small aperture telescopes. While his suggested strategy for telescope sites has been followed, and it has been found being 'above the grosser clouds' can improve telescope performance, the mountains themselves can introduce shear winds and cause more turbulence than one will find at ground level. Furthermore, it is common for the domes or buildings housing the telescopes to cause as much disturbance to observation as the entire atmosphere. Much more work remains to be done in these areas; as Coulman (1987) points out, the effects of a turbulent atmosphere are still of major concern in astronomical observations.

The best way to avoid such atmospheric interference problems is to place the instrument completely outside of the atmosphere, that is, place it into orbit. While one will have no atmospheric trouble with such devices, their cost is

beyond the budget of most research institutes at present and they are expensive and difficult to repair in the event of a failure.

1.1 Active and Adaptive Optics

It is a well known fact that the effects of image blurring are a function of aperture diameter, and for small telescopes ($D < 10$cm) the image is essentially diffraction limited. Thus, the simplest method of avoiding atmospheric turbulence is to limit the aperture size of the telescope so it is sampling a relatively undistorted wavefront. This has the obvious disadvantage of reducing the light gathering power and resolution of the instrument.

Another method is to employ an optical system to correct for any wavefront aberrations. These systems are known as *active* or *adaptive* optics. The distinction between these two types is unclear in the literature. In the context of physical optics, a system is said to be adaptive if it contains negative feedback while an active system is open loop. In astrophysical circles the distinction is based on bandwidth, an adaptive system having a larger bandwidth than an active one; active systems are used for relatively static corrections. As the tilt servo described in this thesis is adaptive under both definitions this term will be used herein.

While the first pratical suggestion for an adaptive optics system for use in astronomy was some forty years ago (Babcock, 1953) and the other forms of adaptive optical systems have been studied for some years (for example the work by Rhodes and Goodman (1973), Muller and Buffington (1974) and Buffington et al (1978)) it has only been in recent times that prototype systems have been built and shown to produce diffraction limited images (Merkle et al (1990) and Roddier et al (1991)). The book by Tyson (1991) contains an excellent review of adaptive optic techniques.

1.2 Stellar Interferometry

In order to achieve higher sensitivity astronomers have been constructing larger and larger aperture telescopes. Telescopes of the 4-5 metre class exist on many sites and the next generation of 8-10 metre class telescopes are being designed and constructed now. These new telescopes are being built with very large apertures not only to increase sensitivity but also to achieve higher resolution. While

larger apertures normally imply greater resolution, the atmosphere will always impose a limit. Although these new instruments are to be built in locations known for excellent seeing conditions and will employ active and adaptive optics, it is thought they will achieve diffraction limited images only in the infrared. Even with apertures of up to 10 metres, telescopes will not be able to resolve most stellar objects or even match the resolution of the larger radio telescopes.

Instead of making a telescope (or telescopes) of very large aperture, using several small aperture telescopes to form an interferometer allows much greater resolution. A small telescope will be less affected by seeing than a large one, for example, the wavefront entering a telescope of aperture less than 20cm can be assumed to be essentially flat but tilted. Adaptive optics, such as those to be described in this thesis, can be used to remove this tilt. With the tilt removed the beams from two telescopes can be combined to form fringes. Recording the visibility of these fringes over a range of baselines is equivalent to sampling the Fourier transform of the brightness profile of the source.

The telescopes making up the interferometer can be placed far apart to form baselines bigger than any existing or proposed telescope aperture. With such a device the techniques developed for radio interferometry can be used, resulting in very high resolution measurements and images. A number of interferometer experiments have been performed using non-redundant masks (for example the MAPPIT project (Bedding et al, 1992) and the work by Wilson et al (1992)) demonstrating that phase closure can be achieved and diffraction limited images produced. Even with a single baseline many useful astronomical results can be obtained.

Early attempts at constructing stellar interferometers, for example the work by Michelson in the 1920's, while having some success in resolving large diameter stars, were abandoned due to instabilities in the instrument structure and atmospheric distortion of the wavefront. A number of years later it was found one could bypass atmospheric turbulence effects by measuring the correlation of light intensity, as the Narrabri Intensity Interferometer did, instead of light amplitude. This instrument successfully measured the diameters of thirty two stars (Hanbury Brown et al, 1974). Unfortunately intensity interferometry implies an extremely poor sensitivity compared to amplitude interferometry, so large apertures (albeit low quality optics) are required. A review of these and other early developments in stellar interferometry can be found in Tokovinin and Shcheglov (1979).

The advent of modern lasers, piezo electric actuators and computer con-

trol systems, along with a better theoretical understanding of the nature of turbulence, means a large baseline amplitude stellar interferometer has now become possible. In 1975 the Chatterton Astronomy department began a feasibility study for constructing such a device which resulted in a prototype instrument with a baseline of 11.4m (Davis and Tango (a), 1985). The prototype successfully redetermined the angular diameter of Sirius (Davis and Tango, 1986) and led to a proposal to construct a long baseline Michelson interferometer called the Sydney University Stellar Interferometer (SUSI) (Davis and Tango (b), 1985).

1.3 The Sydney University Stellar Interferometer

SUSI is a Michelson stellar interferometer operating at optical wavelengths. At present a north/south baseline with 12 fixed siderostats provides baselines ranging from 5 to 640 metres and provision has been made for a future east/west baseline. Refer to figure (1.1) for a diagram of the main optical components of SUSI. Starlight is steered into the optical system by flat mirrors of 20cm diameter using an Alt/Azimuth mount. These mirrors, called siderostats, are placed upon large concrete piers that go several metres into the ground to the underlying bedrock. The aperture diameter is chosen to be small so the light entering the system can be assumed to be basically flat, although tilted. The wavefront tilt servo described in this thesis is then used to remove this tilt. There are twelve siderostats distributed along the baseline. Since the worst air turbulence is located at ground level the light enters a vacuum system immediately after the siderostat and is directed into the enclosure containing the rest of the interferometer optics. A more detailed description of the components relevant to the tilt correction servo is given in Chapter (3); here we just give an overview of the interferometer layout. A description of the design of SUSI can be found in Davis et al (a) (1992) and Davis et al (b) (1992).

Once inside the enclosure the beams are sent through the beam reducing telescope (BRT) to bring their diameter down to a size suitable for use with standard optical components. The BRT reduces the diameter by a factor of three which also multiplies any tilt error by a factor of three. The beams then pass through an atmospheric refraction corrector (ARC), similar to those often used on standard astronomical telescopes, and on to the 70m long optical path length compensator (OPLC). The OPLC is required since the vector pointing to the star will not always be normal to the baseline and the optical path lengths in

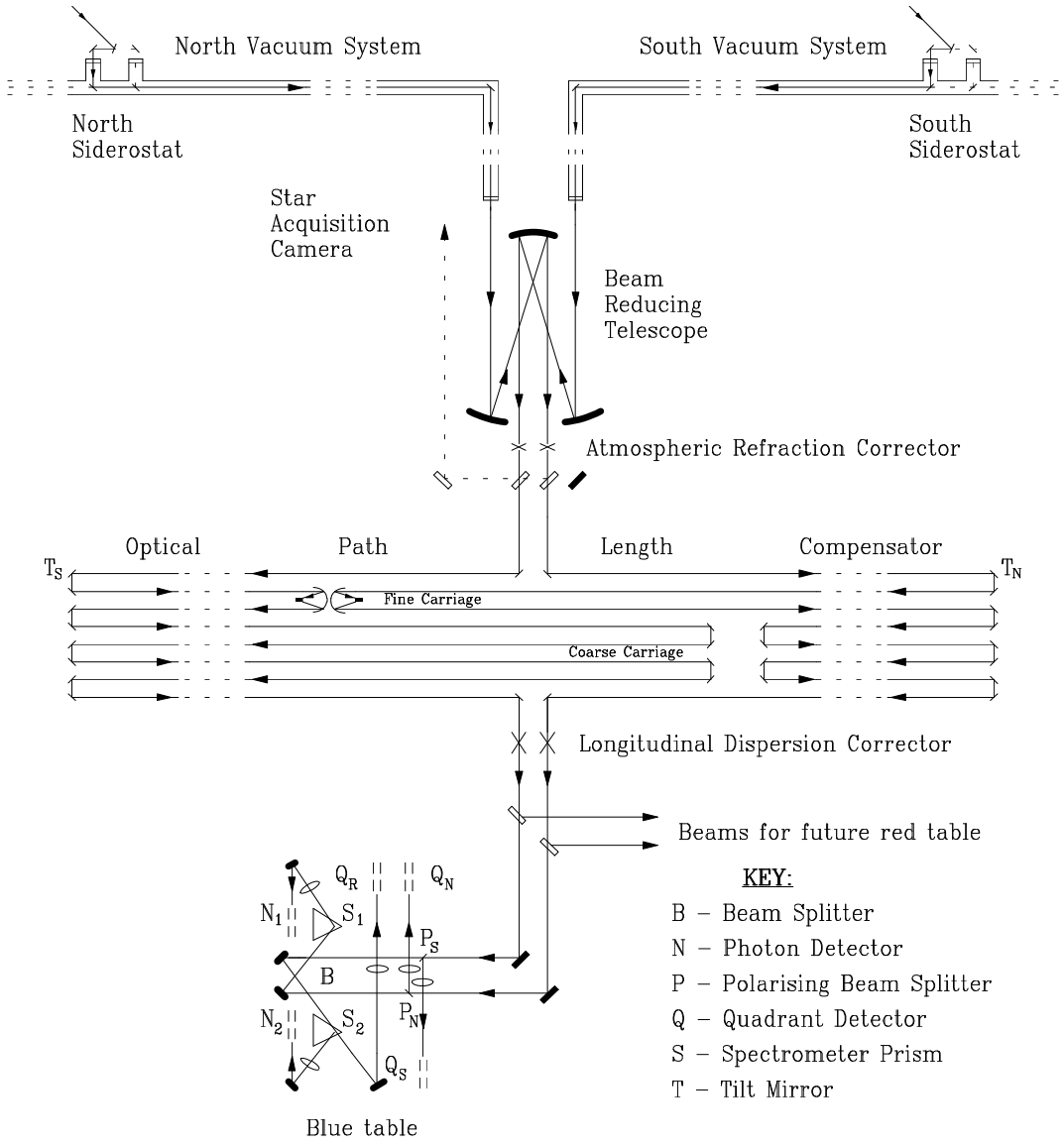

Figure 1.1: A diagram (not to scale) of all the major optical components, except the laser metrology system (LMS), of SUSI. After being guided into the vacuum system by the siderostats and passing through the beam reducing telescope (BRT) the star light is corrected for atmospheric dispersion (ARC) and then either enters the optical path length compensator (OPLC) or is diverted towards the star acquisition camera. The coarse carriage of the OPLC (not yet commissioned) is set once before an observational run to correct for gross phase error while the fine carriage moves in order to track the fringes. The adaptive tilt mirrors are at either end of the OPLC enclosure. Since the path length compensation is performed in air the longitudinal dispersion corrector (LDC) is added to the optical chain after the OPLC. The light is then directed onto the optical table where polarising beamsplitters divert half the light to the quadrant detectors of the tilt servo and the other half towards the main beamsplitter. The two beams leaving the beam splitter are sent through spectrometer prisms and then imaged onto slits and photomultipliers. Note that one of these beams can be diverted to the reference quadrant detector for interferometer alignment.

the two beams will therefore be different. The coarse carriage (not commissioned at time of writing) will only be used for the large baselines and will be set once at the beginning of an observational run. The fine carriage (Gilliand, 1992) moves continuously throughout a run to track the fringes. Stepper motors are used to move the fine carriage along the OPLC track while the reflectors used are *cat's eyes* which can be adjusted by piezo electric actuators. The adaptive tilt mirrors are placed at either end of the OPLC and are used to correct for wavefront tilt in the two beams.

Having passed through the OPLC and tilt mirrors, the two beams are in phase and parallel. However, since the path length compensation is performed in air while the 'real' path length difference is in the vacuum beyond the atmosphere, the beams are sent through a longitudinal dispersion corrector (LDC) before reaching the optical table (Tango, 1990) where they are combined to form fringes. The first of these tables uses optical components from the prototype instrument and is optimised for blue light. Only a subset of the optical components on this table is shown in figure (1.1), however most of those left out are used for interferometer alignment and not astronomical observation. Provision has also been made for a future red light table.

After reaching the optical table, beamsplitters are used to divide each beam into two orthogonally polarised parts. One polarisation is sent to the tilt servo quadrant detectors while the other goes on to the main beamsplitter in which fringes are formed. Three quadrant detectors are placed on the optical table. Two are used for tilt correction in the north and south beams while the third, reference, detector is used for interferometer alignment. One of the beams leaving the main beamsplitter can be diverted towards the reference quadrant detector. The other two detectors can be remotely motor driven in order to ensure they are optically superimposed onto the reference detector. It is also possible, during optical alignment, to insert a spatially filtered blue laser into the beamsplitter and to autocollimate using the siderostats.

At present, a simple narrow bandwidth spectrograph arrangement consisting of prisms, lenses, slits and photomultipliers is used for fringe detection. It is planned to use array photon counting systems in the near future to allow simultaneous measurement of visibility over a larger bandwidth.

1.4 Tilt Servo Requirement Specification

The basic function of the tilt correction servo is to keep the interfering beams of the two arms of SUSI parallel. If the difference in beam tilt is too large, losses in signal to noise ratio will occur in the visibility measurements of the interferometer. The r.m.s. visibility loss caused by tilt error when the beams are combined is given by Buscher (1988) as

$$\eta = 1 - 1.8\langle(\theta/\theta_0)^2\rangle \tag{1.1}$$

where θ is the differential tilt error and θ_0 is the angular radius of the Airy disc formed by the stellar image. Thus in order to ensure these losses are less than 5% the tilt servo must keep the two beams to within 0.167 the size of the Airy disc radius. Assuming the positions of the two beams at any given time are independent variables with a normal distribution (see section 5.1), each beam needs to be stable to within 0.118 of the size of the Airy disc. At present, the aperture diameters available for visibility measurement in SUSI range from 3cm to 12cm. The largest apertures will only be used whenever seeing conditions are good and for faint objects, while the smaller apertures are used to reduce the effect of residual wavefront errors on visibility measurements. For example, to keep visibility losses due to tilt less than 5% for an aperture diameter of 6cm, the tilt servo must keep the beams parallel to within 0.31", which requires a single beam stability of 0.22". The analysis in Chapter 4 will demonstrate that the tilt servo exceeds this criterion.

The servo must track a star image to this precision with a large enough bandwidth to cover the spectrum of tilt caused by the atmosphere. The servo should not be sensitive to frequencies higher than this as the only tilt changes it will be responding to are those caused by photon noise. Choosing a servo bandwidth is a compromise between complete coverage of the tilt spectra and the amplification of photon noise. A method for estimating the required bandwidth must therefore be found. As will be demonstrated in Chapter 2 the range of frequencies required is of the order of tens of hertz extending as far as perhaps 100 hertz. The sample time of the tilt servo must therefore be quite small, at least 10ms or less, although longer sample times will be possible during times of relatively good seeing. This requirement of high speed has implications for the detectors used, the electronics and the computational hardware and algorithms. Chapters 3 and 4 will cover these and other related issues.

A further requirement of the tilt servo is that its limiting magnitude should be as large as possible. If the tilt servo fails, the entire interferometer will

fail; the tilt servo defines the limiting magnitude of SUSI (see section (3.3.1)). The tilt correction system must also operate in the optical waveband of the rest of the instrument. Both these criteria have implications for the glass, coatings, detection system and electronics to be discussed in Chapter 3.

The final requirement of the tilt servo is being capable of logging mirror and detector positions for analysis of seeing conditions and atmospheric turbulence. This is a function of the computer control system. Some results obtained by the tilt system while tracking stellar sources and methods for data reduction are presented in Chapter 5.

Chapter 2

ATMOSPHERIC TURBULENCE THEORY

The atmosphere appears to be in an unpredictable and complex state of turbulent flow. The usual approach, first formulated by Reynolds, is to describe these flows using ensemble averages rather than in terms of individual components. He defined a nondimensional quantity, now known as the Reynolds number, that characterises a turbulent flow. It is defined

$$R = \frac{UL}{\nu_{\text{mol}}}, \tag{2.1}$$

where U and L are the typical velocity and length for the flow and ν_{mol} is the kinematic molecular viscosity. A low Reynolds number indicates the flow is *laminar*, that is regular and smooth in space and time, while a large Reynolds number signifies a highly turbulent flow. Between these extremes the fluid will undergo a series of unstable states. The atmosphere is difficult to study because it has a Reynolds number of the order of 10^6.

In the classical theory, proposed by Lev Landau, the number of the unstable states between laminar and fully turbulent flow would be very large, even infinite. Recent work in the area of chaos theory shows, however, that the final state of full blown turbulence can arise after only a few such transitions. To use this chaos theory in experimental practice, the *strange attractor*, the curve in phase space toward which the system evolves, must be of small dimension. It is also easier to analyse a system which contains temporal, rather than spatial, chaos. New experimental evidence exists (Jorgenson et al., 1991) of a strange attractor for wavefront tilt with a dimension of approximately 5, and it has been suggested (Jorgenson and Aitken, 1992) that wavefront tilt could be predicted over small time periods using neural network methods. While this should en-

able adaptive optics systems to predict wavefront shape and thereby improve performance, the theory is new and undeveloped. Furthermore, as the sample time of the wavefront tilt correction system described herein is small (1ms), and consequently the inherent delay of the servo is also small, we do not require prediction of tilt evolution. Chaos theory has not been investigated further.

In order to establish bandwidths for the tilt servo we must gain an understanding of the temporal properties of the wavefront entering a telescope. To do this we will use the normal approach of studying the spatial properties first and then moving to the temporal domain by using the *Taylor Hypothesis of frozen turbulence*. The Taylor hypothesis means we assume that a frozen piece of turbulence is blown past the aperture by the prevailing wind. The temporal characteristics of the wavefront entering the telescope will therefore be a function of the spatial distribution of turbulent cells, the speed of the prevailing wind and the size of the aperture.

The description of atmospheric turbulence theory to follow is largely based on the review by Coulman (1985), which contains an excellent discussion of the meteorology of seeing and observational work, and the more mathematically detailed review by Roddier (1981). Both papers feature large and comprehensive reference lists. Another extensively referenced summary of turbulence theory as it applies to astronomical seeing and adaptive optics can be found in Tyson (1991). The article by Frisch and Orszag (1990) is a good introduction to the concepts involved in turbulence theory in general, while a review of turbulence theory as it applies to imaging systems in particular is given by Fried (1979). The book by Stull (1991), while not specifically concerned with astronomical application, is a good standard text on the meteorology of the boundary layer and basic turbulence theory. The final section dealing with the power spectra of the Zernike expansion coefficients (section (2.3.2)) is original to this thesis.

2.1 Basic Formulation of Turbulence Theory

Simply stating that the atmosphere is turbulent does not imply it will affect optical propagation. It is possible to have a fluid in which strong mechanical turbulence will affect optical propagation very little, for example, an incompressible fluid. It is changes in the refractive index of the air, and not turbulence in itself, that causes changes in optical propagation. Hence the requirement to relate atmospheric turbulence to refractive index changes. We will model this coupling as temperature fluctuations driven by temperature differentials

throughout the atmosphere. Mixing of 'parcels' of warm and cool air comes as a result of the turbulent nature of the atmosphere. While the exact pattern of temperature distribution varies enormously with location, season and time of day, it is reasonable to suppose that if we can understand the velocity distribution, we can say something about the temperature distribution. Simple gas law theory states that the temperature is inversely proportional to density, and therefore to refractive index. In this way, knowledge of the temperature distribution will lead us towards an understanding of wave propagation in a turbulent atmosphere.

2.1.1 Turbulence and the Inertial Subrange

The standard model for atmospheric turbulence, first published by Taylor (1921) and Richardson (1922) and later expanded (Taylor (1935), Kolmogorov (b) (1941) and Kolmogorov (c) (1941)), states that energy enters the flow at low spatial frequencies as a direct result of the non-linearity of the Navier-Stokes equation governing fluid motion. This forms eddies of large size which have a scale length L_0 and spatial frequency $\kappa_{L_0} = 2\pi/L_0$. This outer scale length varies according to local conditions, ranging from the distance to the nearest physical boundary when close to the ground up to the thickness of the largest turbulent eddies, that is about 100m. Measurements of L_0 range from 2m (Nightingale and Buscher, 1991) to the controversial figure of greater than 2km (Colavita et al, 1987).

These large eddies are unstable and break up into smaller eddies, corresponding to a different scale length and a higher spatial frequency. These 'second generation' eddies are also unstable and will break up into still smaller eddies. Since the scale length associated with these eddies decreases the Reynolds number associated with the flow defined in equation (2.1) must also be decreasing. When the Reynolds number is low enough, the turbulent break up of the eddies stops and the kinetic energy of the flow is lost as heat via viscous dissipation. This imposes a highest possible spatial frequency on the flow beyond which little or no energy is available to support turbulence. We shall denote this, the inner scale length, as l_0 and its corresponding spatial frequency as $\kappa_{l_0} = 2\pi/l_0$. The inner scale length varies from a few millimetres near the ground up to about 1 cm high in the atmosphere. This turbulent cascade is neatly described by Richardson (1922) in the couplet:

Big whirls have little whirls that feed on their velocity
And little whirls have lesser whirls and so on to viscosity.

All of the analysis to follow assumes we are working between these two scale lengths, that is if $\mathbf{r}$ is the vector between two points of interest then the magnitude of $\mathbf{r}$, written r, must be such that $l_0 < r < L_0$. This is known as the *inertial subrange* and is of fundamental importance to all the work to come. We can say nothing about higher spatial frequencies than κ_{l_0} as there should be little or no turbulent behaviour in this range. Secondly, as we have defined a strict lower bound of κ_{L_0} we can know nothing about very low spatial frequencies. It is therefore impossible to calculate the contribution of these very low frequencies to the velocity, or refractive index, distribution. Thirdly, while we will assume that all distances we work with will be within this inertial subrange, we cannot know what the relevant scale lengths really are at any one time or location. The air inside a dome, just above the ground or near some other kind of obstacle will not have the same inertial subrange as the rest of the atmosphere, although the general effect would be to reduce the upper scale length L_0 and add higher spatial frequency components to the flow. While it is possible to derive useful predictions for turbulence within the inertial subrange, it is important to remember these assumptions have been made, and that the results derived only hold within the inertial subrange.

2.1.2 Structure Functions and Passive Additives

Since the method we are using is one of studying ensemble averages rather than detailed properties, the natural approach would be to try and find a correlation or covariance function of refractive index. Unfortunately, the effect of establishing a lower bound to spatial frequencies is that the unknown contribution of the very low frequencies allows the variance to rise towards infinity. This is a mathematical problem rather than a physical one as there are no observable consequences of an infinite variance. It is for this reason that it is normal to use *structure functions*, which do not suffer from this problem, rather than correlation functions. The velocity structure function is defined as

$$D_v(\mathbf{r}) = \langle |\mathbf{v}(\boldsymbol{\rho} + \mathbf{r}) - \mathbf{v}(\boldsymbol{\rho})|^2 \rangle \tag{2.2}$$

where $\mathbf{v}(\mathbf{r})$ is the flow velocity at position $\mathbf{r}$ and the angular brackets denote an ensemble average over the repeated parameter $\boldsymbol{\rho}$. Structure functions are related to the covariance function via

$$D_v(\mathbf{r}) = 2[B_v(\mathbf{0}) - B_v(\mathbf{r})] \tag{2.3}$$

and the covariance is defined

$$B_v(\mathbf{r}) = \langle v(\boldsymbol{\rho}) v(\boldsymbol{\rho} + \mathbf{r}) \rangle. \tag{2.4}$$

To obtain an expression for this structure function a few more assumptions need to be made (Kolmogorov (a), 1941):

1. Within the inertial subrange average quantities are invariant, while detailed structures need not be.

2. Motions on a small scale are locally isotropic, thus the vector notation can be replaced by a scalar one. Many expressions need only contain the magnitude of the displacement r rather than the vector $\mathbf{r}$.

3. The rate of production of turbulent energy is equal to the rate of viscous dissipation ϵ_0.

4. The velocity of motions of scale length r is a function of r and ϵ_0 of the form $V \propto \epsilon_0^a r^b$.

Dimensional analysis[1] then yields

$$V \propto \epsilon_0^{\frac{1}{3}} r^{\frac{1}{3}}. \tag{2.5}$$

Noting that the structure function has the same dimensions as V^2 we see the velocity structure function $D_v(\mathbf{r})$ must be proportional to the distance between the points r to the power of two thirds. Adding a constant of proportionality C_v^2, referred to as the *structure constant*, we find the structure function can be written

$$D_v(\mathbf{r}) = C_v^2 r^{\frac{2}{3}}, \tag{2.6}$$

where r is the magnitude of the vector $\mathbf{r}$. This implies that there is no characteristic scale length within the inertial subrange.

Up to this point we have only discussed the velocity distribution. We need to couple this to the refractive index distribution via temperature, density and water vapour variations. In order to perform this operation the idea of a *conserved passive additive* (Tatarski (1961) and Tatarski (1971)) is required. A passive additive is a quantity that does not affect the dynamics of the flow. A conserved additive will not disappear through some chemical reaction in the flow. Any conserved passive additive will also follow the two thirds power law derived above for the velocity structure function. While temperature is not

[1]Dimensional analysis is the process of ensuring that both sides of an expression have the same physical dimensions. In this case ϵ_0 has the dimensions ML^2T^{-3} (where M stands for mass, L for length and T for time), V has the dimensions LT^{-1} and r has dimension L. If we assume the mass component is incorporated into the constant of proportionality, the values of a and b must both be 1/3.

strictly a passive additive, since a temperature gradient can affect the flow, Tatarski argued that it is still reasonable to consider temperature variations to be a conserved passive additive. Thus the temperature structure function defined as

$$D_T(\mathbf{r}) = \langle |T(\boldsymbol{\rho}+\mathbf{r}) - T(\boldsymbol{\rho})|^2 \rangle, \tag{2.7}$$

can be written

$$D_T(\mathbf{r}) = C_T^2 r^{\frac{2}{3}} \tag{2.8}$$

where C_T^2 is the temperature structure constant. Many experiments (Coulman (1969), Wyngaard et al (1971), Coulman (1974), Hartley et. al. (1981), Walters and Kunkel (1981), Forbes (b) (1983), Forbes et al (1985), ten Brummelaar (1985) and Lopez (1991)) confirm this two thirds power law in the atmosphere. The temperature structure constant C_T^2 is proportional to the local vertical temperature gradient and is not related to the velocity of the flow. Hence, even if the local wind velocity is quite large C_T^2 can be small, even zero; that is, the two structure constants are not strongly coupled. As we are dealing with small perturbations in the absolute temperature, and since density and therefore refractive index are inversely proportional to temperature, we write the refractive index structure function, defined

$$D_N(\mathbf{r}) = \langle |n(\boldsymbol{\rho}+\mathbf{r}) - n(\boldsymbol{\rho})|^2 \rangle \tag{2.9}$$

as

$$D_N(\mathbf{r}) = C_N^2 r^{\frac{2}{3}}, \tag{2.10}$$

where the refractive index structure constant is C_N^2 and is a basic measure of the optical strength of atmospheric turbulence. The temperature and refractive index structure constants are related via (Coulman, 1985)

$$C_N^2 = \left[\frac{80 \times 10^{-6} P}{T^2}\right]^2 C_T^2 \tag{2.11}$$

where the air pressure P is in millibars and the temperature T is in kelvin.

2.1.3 The Kolmogorov Spectrum

It will also be necessary to find an expression for the spatial spectrum of turbulence. We require an expression for the energy $E(\kappa)d\kappa$ between spatial frequencies κ and $\kappa + d\kappa$ which can be obtained from the dimensional analysis performed earlier. This energy must be proportional to the velocity squared

and the spatial frequency is inversely proportional to r. Combining this with equation (2.5) we get, in one dimension

$$E(\kappa)d\kappa \propto \kappa^{-\frac{2}{3}} \tag{2.12}$$

or

$$E(\kappa) \propto \kappa^{-\frac{5}{3}}. \tag{2.13}$$

To convert the three dimensional spectra $E(\boldsymbol{\kappa})$ to its one dimensional equivalent $E(\kappa)$ we integrate over all directions. Since we have assumed local isotropy we find that $E(\kappa) = 4\pi\kappa^2 E(\boldsymbol{\kappa})$ and therefore

$$E(\boldsymbol{\kappa}) \propto \kappa^{-\frac{11}{3}} \tag{2.14}$$

This is known as the *Kolmogorov Spectrum* and holds for any conserved passive additive including refractive index. The three dimensional spectrum of refractive index changes $\Phi_N(\boldsymbol{\kappa})$ is then

$$\Phi_N(\boldsymbol{\kappa}) \propto \kappa^{-\frac{11}{3}} \tag{2.15}$$

The constant of proportionality can be found by relating this spectrum to the structure function defined in equation (2.10). The structure function $D_N(\mathbf{r})$ is related to the covariance function $B_N(\mathbf{r})$ via equation (2.3) and the covariance is the three dimensional Fourier transform of the spectrum $\Phi_N(\boldsymbol{\kappa})$ (Roddier, 1981). In this way Tatarski (1961) showed that

$$\Phi_N(\boldsymbol{\kappa}) = 0.033 C_N^2 \kappa^{-\frac{11}{3}} \tag{2.16}$$

This is the Kolmogorov spectrum for refractive index changes for a given structure constant C_N^2. It is only valid within the inertial subrange ($\kappa_{L_0} < \kappa < \kappa_{l_0}$) and for a 'block' of atmosphere throughout which the structure constant is indeed constant.

2.2 Application to Astronomy

Now that an expression for the spectrum of refractive index changes due to a single turbulent layer has been derived, we must consider the atmosphere as a whole. It was Tatarski (1961 and 1971) who first published a treatment of the problem from an astronomical point of view. A further set of simplifying assumptions need to be made in order to understand seeing at ground level. First of all we shall use a *phase screen* approach (Lee and Harp, 1969). Each

turbulent layer will only introduce a phase change into the propagating wavefront, or in other words, scintillation will be largely ignored. A treatment of the problems of scintillation can be found in Coulman (1985), Roddier (1981), Young (1970), Young (1969) and Young (1967). Secondly, most of the work will be done assuming vertically propagating monochromatic waves of wavelength λ, wave number $k = 2\pi/\lambda$ and polarisation will be ignored. This means the statistics of the atmosphere will depend only on the height above the ground h. Generalisation to stars away from zenith and other wavelengths will then be given. Thus at the position $(\mathbf{x}, h)$ the complex amplitude of the light field is written

$$\Psi_h(\mathbf{x}) = |\Psi_h(\mathbf{x})| \exp[i\varphi_h(\mathbf{x})] \tag{2.17}$$

where $\varphi_h(\mathbf{x})$ is the phase. Thirdly, the complex amplitude will be normalised such that it is unity outside the earth's atmosphere ($\Psi_\infty = 1$) and phase will always be measured with respect to the average value ($\langle\varphi_h(\mathbf{x})\rangle = 0$).

2.2.1 Temporal and Spatial Properties of Structure Constants

The structure 'constants' are only constant within a given layer of the atmosphere and are assumed to be a function of height above the ground z. Before moving on to the derivation of structure functions for single and multiple layers it is important to understand the behaviour of the structure constants with height and time. Techniques used for measuring the behaviour of the atmosphere at different heights include microthermal studies, radar soundings, balloon experiments, aircraft experiments and acoustic soundings (Coulman (1969) and Coulman (1974)). Both the review papers by Coulman (1985) and Roddier (1981) contain many references to these measurements, although the paper by Coulman covers the meteorology of seeing in more detail.

The behaviour of the refractive index structure constant with height, as derived experimentally, can be broken up into four zones:

1. Purely local effects. This includes the local terrain, the telescope dome (if there is one) and so on. The primary effect of local objects is to change the inertial subrange and introduce temperature differentials. The significant scale lengths in this zone depend very much on the objects nearby while the refractive index structure constant scales as $z^{-\frac{2}{3}}$.

2. The surface boundary layer or troposphere. This is the first few kilometres

of atmosphere and, along with local effects, contains three quarters of the atmosphere. The dominant source of turbulence in this zone is wind shear, the significant scale lengths are roughly constant while the refractive index structure constant scales as $z^{-\frac{4}{3}}$

3. Above the troposphere is the stratosphere. In this zone the scale lengths are height dependent. It appears, from balloon experiments, that the turbulence in this zone is concentrated into thin (100-200m) layers.

4. In the rest of the atmosphere the turbulence is due to wind shear and stable temperature gradients dominate. This zone has little effect on seeing conditions.

A plot of average refractive index structure constant values with height is given in figure (2.1). It should be remembered that this model is for nighttime conditions only since during the day the effect of the ground, having been heated by the sun, becomes very significant. As we are interested in nighttime conditions here no further discussion of daytime seeing behaviour will be undertaken.

This model, while not reliable for short term experiments, gives very good order of magnitude predictions. Thus, while the refractive index structure constant does not hold the same value through the entire atmosphere and can undergo large short term changes, experimental evidence indicates that a theory based on the summation of several thin layers is reasonable.

2.2.2 Contribution of a Thin Layer

Given the stratification and phase screen approximations, in combination with basic turbulence theory, we are now in a position to calculate the effect of the atmosphere on an initially flat wavefront. To do so, we will follow the method set out in the review by Roddier (1981) and first calculate the effect of a single turbulent layer and then move on to a summation of many such layers.

Consider a layer of turbulent air of thickness δh and height h above the ground. The thickness δh is chosen so that it is large compared to the scale of the turbulent eddies but small enough for the phase screen approximation to remain valid. We then write the phase shift introduced by this thin layer as

$$\varphi_h(\mathbf{x}) = k \int_h^{h+\delta h} dz\, n(\mathbf{x}, z). \tag{2.18}$$

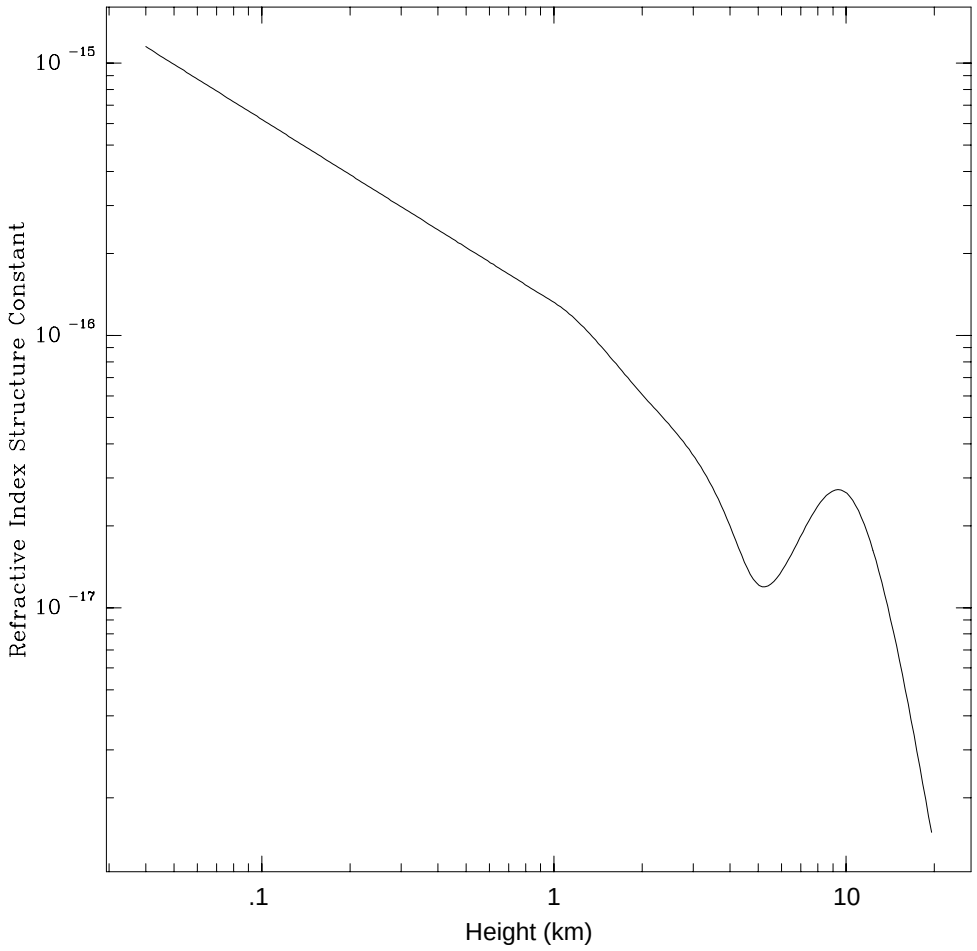

Figure 2.1: This plot (taken from Roddier (1981)) shows the long term average refractive index structure constant profile with height for night-time conditions. Note that over short time periods the real behaviour may be very different, for example, in the troposphere very large short term fluctuations have been measured.

Therefore if the complex amplitude before passing through the layer is unity, after the layer it is

$$\Psi(\mathbf{x}) = \exp[i\varphi(\mathbf{x})]. \tag{2.19}$$

The coherence function of the complex amplitude $\langle \Psi_h(\mathbf{x})\Psi_h^*(\boldsymbol{\xi}+\mathbf{x})\rangle$ is then

$$B_h(\mathbf{x}) = \langle \exp i[\varphi(\boldsymbol{\xi}) - \varphi(\boldsymbol{\xi}+\mathbf{x})]\rangle. \tag{2.20}$$

Roddier (1981) points out the similarity of this equation to the Fourier transform of the probability density function of the expression in square brackets at unit frequency. He then shows that due to equation (2.18) this quantity can be considered to be the sum of many independent variables and therefore have Gaussian statistics and uses a statistical argument to show that

$$B_h(\mathbf{x}) = \exp\left[-\frac{1}{2}D_\varphi(\mathbf{x})\right] \tag{2.21}$$

where $D_\varphi(\mathbf{x})$ is the structure function of the phase defined by

$$D_\varphi(\mathbf{x}) = \langle |\varphi(\boldsymbol{\xi}) - \varphi(\boldsymbol{\xi}+\mathbf{x})|^2\rangle. \tag{2.22}$$

The coherence function $B_h(\mathbf{x})$ is now seen to be a function of the phase structure function, which is dependent on the refractive index fluctuations. If we define the covariance of phase to be

$$B_\varphi(\mathbf{x}) = \langle \varphi(\boldsymbol{\xi})\varphi(\boldsymbol{\xi}+\mathbf{x})\rangle \tag{2.23}$$

the phase structure function can be written, using the relationship defined in equation (2.3), as

$$D_\varphi(\mathbf{x}) = 2[B_\varphi(\mathbf{0}) - B_\varphi(\mathbf{x})]. \tag{2.24}$$

Combining equations (2.23) and (2.18) we find

$$B_\varphi(\mathbf{x}) = k^2 \int_h^{h+\delta h} dz \int_{h-z}^{h+\delta h-z} d\zeta\, B_N(\mathbf{x},\zeta) \tag{2.25}$$

where $B_N(\mathbf{x},\zeta)$ is the three dimensional refractive index covariance

$$B_N(\mathbf{x},\zeta) = \langle n(\boldsymbol{\xi},z)n(\boldsymbol{\xi}+\mathbf{x},z')\rangle \tag{2.26}$$

and $\zeta = z' - z$. We take the integration over ζ to be from $-\infty$ to $+\infty$ since we have assumed that the thickness of the layer is large compared to the correlation scale of the turbulence. This yields

$$B_\varphi(\mathbf{x}) = k^2\delta h \int d\zeta\, B_N(\mathbf{x},\zeta) \tag{2.27}$$

Substituting this into equation (2.24) gives

$$D_\varphi(\mathbf{x}) = 2k^2\delta h \int d\zeta\, [B_N(\mathbf{0},\zeta) - B_N(\mathbf{x},\zeta)]. \tag{2.28}$$

Re-writing the refractive index structure function defined in equation (2.10) as

$$D_N(\mathbf{x},\zeta) = C_N^2(x^2+\zeta^2)^{\frac{1}{3}} \tag{2.29}$$

and using the relationship defined in equation (2.3) equation (2.28) can be integrated and yields

$$D_\varphi(\mathbf{x}) = 2.91k^2\, C_N^2\, \delta h\, x^{\frac{5}{3}} \tag{2.30}$$

which, using equation (2.21), means that

$$B_h(\mathbf{x}) = \exp -\frac{1}{2}(2.91k^2\, C_N^2\, \delta h\, x^{\frac{5}{3}}). \tag{2.31}$$

Finally, using the Fresnel approximation Roddier (1981) shows that $B_0(\mathbf{x}) = B_h(\mathbf{x})$ and therefore the covariance of the phase at ground level due to a thin layer of turbulence at some height off the ground is

$$B_0(\mathbf{x}) = \exp\left[-\frac{1}{2}D_\varphi(\mathbf{x})\right]. \tag{2.32}$$

It is, however, not strictly true that $D_\varphi(\mathbf{x})$ is the same at ground level. This is because for high altitude layers the complex amplitude will vary in both phase and amplitude. The turbulent layer acts like a diffracting screen and strickly we should use diffraction theory to determine the effect at ground level. These effects are small, however, so we make the phase screen approximation and take the phase structure function at ground level to be the same as that inside the thin layer.

2.2.3 Addition of Many Thin Layers

Now the contribution of a single turbulent layer has been found it remains to find the sum of many such turbulent layers which we shall number from 1 to J. Each layer is at height h_j and has a thickness of δh_j. The effect of each turbulent layer will be to introduce a phase change $\varphi_j(\mathbf{x})$ to the complex amplitude of the wavefront. Thus the complex amplitude after passing through layer j is

$$\Psi_{h_j}(\mathbf{x}) = \Psi_{h_j+\delta h_j}(\mathbf{x})\, \exp[i\varphi_j(\mathbf{x})] \tag{2.33}$$

and the coherence at the output is

$$B_{h_j}(\mathbf{x}) = \langle \Psi_{h_j+\delta h_j}(\boldsymbol{\xi})\Psi_{h_j+\delta h_j}(\boldsymbol{\xi}+\mathbf{x})\rangle \times \langle \exp i[\varphi_j(\boldsymbol{\xi}) - \varphi_j(\boldsymbol{\xi}+\mathbf{x})]\rangle. \tag{2.34}$$

The second expression inside angular brackets is the same as the coherence function defined in equation (2.20). Substituting the expression for that given in equation (2.31), and noting that for each layer the coherence function is multiplied by such an expression, we find at ground level the coherence function is given by

$$B_0(\mathbf{x}) = \prod_{j=1}^{J} \exp -\frac{1}{2}[2.91k^2\, C_N^2(h_j)\, \delta h_j\, x^{\frac{5}{3}}] \tag{2.35}$$

$$= \exp -\frac{1}{2}\left[2.91k^2 x^{\frac{5}{3}} \sum_{j=1}^{J} C_N^2(h_j)\, \delta h_j\right]. \tag{2.36}$$

$$\tag{2.37}$$

For a star at an angular distance of γ away from zenith viewed through a continuous turbulence distribution this expression can be generalised to be

$$B_0(\mathbf{x}) = \exp -\frac{1}{2}\left[2.91k^2(\cos\gamma)^{-1}x^{\frac{5}{3}} \int dz\, C_N^2(z)\right]. \tag{2.38}$$

Thus, using the relationship between the coherence function and phase structure function given in equation (2.32), the phase structure function at ground level can be written

$$D_\varphi(\mathbf{x}) = 2.91k^2(\cos\gamma)^{-1}x^{\frac{5}{3}} \int dz\, C_N^2(z)\,. \tag{2.39}$$

Equations (2.38) and (2.39) are the fundamental results of this section and will be used to represent astronomical seeing at ground level.

2.2.4 Fried's Coherence Length

The final step in the application of turbulence theory to astronomical seeing is to achieve some sort of single parameter measurement of seeing. Following the work of Fried (1965) we use the parameter r_0, known as *Fried's coherence length*, as this measure. This coherence length has many useful interpretations:

- The wavefront across an aperture of diameter r_0 has an rms phase distortion of about 1 radian (see section (2.3.3)).
- The resolution of a long exposure using a telescope affected by atmospheric turbulence can be no better than one using an aperture of r_0 (see below).
- The optimal aperture size for a short exposure image is approximately $3.8r_0$ (Fried, 1966).

Other interpretations and references are listed in Fried and Mevers (1974). In order to derive an expression for r_0 we once again follow Roddier's methodology and define the resolution of a telescope to be

$$\mathcal{R} = \int d\mathbf{f}\, B(\mathbf{f})T(\mathbf{f}) \tag{2.40}$$

where $\mathbf{f}$ is the spatial frequency vector with magnitude f, $B(\mathbf{f})$ is the second order moment of the complex amplitude at the aperture given by[2] $B_0(\lambda\mathbf{f})$ and $T(\mathbf{f})$ is the optical transfer function of the telescope. A small telescope with an unobscured circular aperture of diameter D (that is $D << r_o$) will be diffraction limited and its resolving power will only depend on the optical transfer function of the telescope:

$$\mathcal{R}_D = \int d\mathbf{f}\, T(\mathbf{f}) = \frac{1}{4}\pi(D/\lambda)^2. \tag{2.41}$$

A large telescope's resolving power will be dominated by turbulence effects so

$$\mathcal{R}_\infty = \int d\mathbf{f}\, B(\mathbf{f}) \tag{2.42}$$

where $B(\mathbf{f})$, using equation (2.38), is given by

$$B(\mathbf{f}) = B_0(\lambda\mathbf{f}) = \exp -\frac{1}{2}\left[2.91k^2\,(\cos\gamma)^{-1}\,(\lambda f)^{\frac{5}{3}}\int dz\, C_N^2(z)\right]. \tag{2.43}$$

The integration in equation (2.42) results in

$$\mathcal{R}_\infty = (6\pi/5)\left(\frac{1}{2}\left[2.91k^2\,(\cos\gamma)^{-1}\,\lambda^{\frac{5}{3}}\int dz\, C_N^2(z)\right]\right)^{-\frac{6}{5}}\Gamma(6/5). \tag{2.44}$$

We are now in a position to derive an expression for r_0 if we define it as the diameter for which $\mathcal{R}_D = \mathcal{R}_\infty$. So, placing $D = r_0$ in equation (2.41), we find equation (2.43) can be written in the form

$$B(\mathbf{f}) = \exp -3.44(\lambda f/r_0)^{-\frac{5}{3}} \tag{2.45}$$

which leads to

$$B_0(\mathbf{x}) = \exp -3.44(x/r_0)^{-\frac{5}{3}}. \tag{2.46}$$

Comparing this to equation (2.38) yields an expression for r_0 in terms of the angle away from zenith and an integral over the refractive index structure constant:

$$r_0 = \left[0.423k^2\,(\cos\gamma)^{-1}\int dz\, C_N^2(z)\right]^{-\frac{3}{5}}. \tag{2.47}$$

[2]The function $B_0(\mathbf{x})$ has the input variable $\mathbf{x}$, which is a spatial vector, while the function $B(\mathbf{f})$ has as its input variable the spatial frequency $\mathbf{f}$. One can therefore move from one function to the other using the relation $\mathbf{x} = \lambda\mathbf{f}$.

Now that we have a way of relating r_0 to the wave number k, the zenith angle γ, and the refractive index structure constant C_N^2, it is useful to express all of the important functions describing atmospheric turbulence in terms of r_0. Combining equation (2.46) with equation (2.32) gives us an expression for the phase structure function across the telescope aperture

$$D_\varphi(\mathbf{x}) = 6.88(x/r_0)^{\frac{5}{3}}. \tag{2.48}$$

This relationship has been experimentally confirmed by a number of authors including O'Byrne (1988) and Nightingale and Buscher (1991). Using the fact that the structure function is related to the power spectrum via (Noll, 1976)

$$D_\varphi(\mathbf{x}) = 2\int d\boldsymbol{\kappa}\Phi_\varphi(\boldsymbol{\kappa})[1-\cos(2\pi\boldsymbol{\kappa}\cdot\mathbf{x})] \tag{2.49}$$

the power spectrum of phase fluctuations due to Kolmogorov turbulence at the telescope aperture is

$$\Phi_\varphi(\boldsymbol{\kappa}) = \left(0.023/r_0^{\frac{5}{3}}\right)\ \kappa^{-\frac{11}{3}}. \tag{2.50}$$

Fried's coherence length, apart from giving us a useful physical measure of seeing with immediate application to optical astronomy, also yields simplified expressions for the coherence function (equation (2.46)), the phase structure function (equation (2.48)), and the phase power spectrum (equation (2.50)) at the input of an unobscured telescope with a circular aperture.

2.3 Wavefront Analysis using Zernike Polynomials

To apply turbulence theory to the performance of an optical telescope we now introduce a normalised set of orthogonal polynomials defined over a unit circle known as the *Zernike Polynomials*. The phase across the aperture can be expanded in terms of these polynomials and the temporal behaviour of the expansion coefficients can then be studied. The work in this section is largely based on the work by Noll (1976) using a modified set of Zernike polynomials while a more general description can be found in Born and Wolf (1987) section 9.2. A very good discussion of the polynomials along with some pictorial representations and numerical methods for coefficient determination can be found in Wang and Silva (1980) while methods for experimental determination can be found in Lawrence and Chow (1984).

2.3.1 Zernike Polynomial Definition and Properties

Using polar coordinates ρ and θ, normalised for an unobscured aperture of radius R, the phase of the wavefront across the aperture can be written

$$\varphi(R\rho,\theta) = \sum_j a_j Z_j(\rho,\theta) \tag{2.51}$$

where $Z_j(\rho,\theta)$ is the Zernike polynomial of order j, a_j are the expansion coefficients given by

$$a_j = \int d\boldsymbol{\rho}\, W(\rho)\, \varphi(R\rho,\theta)\, Z_j(\rho,\theta) \tag{2.52}$$

and the weighting function

$$W(\rho) = \begin{cases} 1/\pi & \rho \le 1 \\ 0 & \rho > 1 \end{cases} \tag{2.53}$$

is added so that the integral can be taken over all space. The Zernike polynomials themselves are given by

$$Z_j(\rho,\theta) = \sqrt{n+1}\, R_n^m(\rho) \times \begin{cases} \sqrt{2}\cos m\theta & m \neq 0, \quad j \text{ even} \\ \sqrt{2}\sin m\theta & m \neq 0, \quad j \text{ odd} \\ 1 & m = 0 \end{cases} \tag{2.54}$$

where

$$R_n^m(\rho) = \sum_{s=0}^{(n-m)/2} \frac{(-1)^s (n-s)!}{s!\,[(n+m)/2-s]!\,[(n-m)/2-s]!}\, \rho^{n-2s}. \tag{2.55}$$

The constants m and n are integers such that $m \le n$ and $n - |m|$ is even. The index j is used to order the modes, the first eight of which are shown in table (2.1). The low order modes have a direct correspondence to common aberration terminology and, most importantly in the context of this thesis, to that of wavefront tilt (modes 2 and 3).

Zernike polynomials follow the orthogonality relation

$$\int d\mathbf{r} W(r) Z_j(\mathbf{r}) Z_{j'}(\mathbf{r}) = \delta_{jj'}. \tag{2.56}$$

The only other property of the Zernike polynomials that will be required for an analysis of turbulence is their Fourier transform $Q_j(k,\phi)$ defined by

$$W(\rho) Z_j(\rho,\theta) = \int d\,\mathbf{k} Q_j(k,\phi) \exp(-2\pi i \mathbf{k}\cdot\boldsymbol{\rho}) \tag{2.57}$$

and written as (Born and Wolf, 1987)

$$Q_j(k,\phi) = \sqrt{n+1}\, \frac{J_{n+1}(2\pi k)}{\pi k} \times \begin{cases} (-1)^{(n-m)/2}\, i^m \sqrt{2}\cos m\phi & m \neq 0, \text{even } j \\ (-1)^{(n-m)/2}\, i^m \sqrt{2}\sin m\phi & m \neq 0, \text{odd } j \\ (-1)^{n/2} & m = 0 \end{cases} \tag{2.58}$$

mode j	Common name	n	m	Zernike Polynomial
1	Constant/Piston	0	0	$Z_1 = 1$
2	X Tilt/Lateral Position	1	1	$Z_2 = 2\rho\cos\theta$
3	Y Tilt/Lateral Position	1	1	$Z_3 = 2\rho\sin\theta$
4	Defocus/Longitudinal Position	2	0	$Z_4 = \sqrt{3}(2\rho^2 - 1)$
5	Astigmatism (3rd order)	2	2	$Z_5 = \sqrt{6}\rho^2\cos 2\theta$
6	Astigmatism (3rd order)	2	2	$Z_6 = \sqrt{6}\rho^2\sin 2\theta$
7	Coma (3rd order)	3	1	$Z_7 = \sqrt{8}(3\rho^3 - 2\rho)\sin\theta$
8	Coma (3rd order)	3	1	$Z_8 = \sqrt{8}(3\rho^3 - 2\rho)\cos\theta$

Table 2.1: The first eight Zernike polynomials. The mode numbering is such that even j values represent the symmetric (cos) modes while odd values of j represent the antisymmetric (sin) modes. There is a direct correspondence between these polynomials and the kinds of aberrations traditionally discussed in optics.

With this set of polynomials defined we will now proceed to assume that in optical telescopes of small ($R \leq r_0$), unobscured circular aperture, such as those used in SUSI, the wavefront is well approximated by the first three polynomials. This approximation will be shown to be valid for Kolmogorov turbulence in section (2.3.3). In SUSI, only the modulus of the visibility is measured; consequently measurements are insensitive to the piston mode, as long as the characteristic time for piston mode fluctuations exceeds the sample time of the fringe detecting system. It is the job of the tilt correction servo to remove the remaining tilt modes. The angle of tilt in either axis is related to the corresponding Zernike expansion coefficient via

$$\phi_{v,h} = a_{2,3}\frac{\lambda}{\pi R} \tag{2.59}$$

where $\phi_{v,h}$ are the vertical and horizontal wavefront tilt respectively.

To proceed with the design of the tilt servo, it is necessary to know the expected temporal power spectrum and variance of these coefficients. Before deriving these spectra in the next section, a brief discussion of the definition of wavefront tilt may be in order. A number of possible definitions exist. We shall use the relationship defined in equation (2.59). Another, similar, definition is the angle of a plane fitted to the phase profile of the wavefront in a 'least squares' sense. One could also define the tilt in terms of an average phase angle taken over the entire aperture (Tango and Twiss, 1980), or equivalently (Merrill, 1991), the optical analogue of the Ehrenfest theorem from quantum mechanics.

A conflicting definition is the difference in phase of one side of the aperture to the other, or, in an interferometer, of one aperture to the other divided by the aperture diameter or the interferometer baseline. While not invalid, this definition does not correspond to the sorts of measurements made by the detectors used in the SUSI wavefront tilt correction servo. Authors who have investigated the power spectra of expansion coefficients in the past (for example Clifford (1971)) using this definition do not achieve results relevant to tilt servo design. The statistics of this definition of tilt are exactly the same as for piston phase, and therefore contain no new information about the wavefront. Care should be taken to ensure that the particular definition of wavefront tilt, and its measurement, are kept in mind when reading the literature on this subject. Further discussion of tilt definition and measurement techniques can be found in sections (3.1) and (5.2).

2.3.2 Temporal Power Spectra of Wavefront Distortions

In order to derive the power spectra due to Kolmogorov turbulence of a given mode j we will use a similar method to that used by Greenwood and Fried (1976), Clifford (1971), Hogge and Butts (1976) and Tango and Twiss (1980). We first calculate the temporal autocorrelation defined

$$C_{a_j}(\tau) = \langle a_j(t) a_j(t+\tau) \rangle \tag{2.60}$$

where the angular brackets denote an ensemble average. The power spectrum is then given by the Fourier transform of the autocorrelation function via the autocorrelation theorem (Bracewell, 1986)

$$W_{a_j}(f) = \int_{-\infty}^{\infty} C_{a_j}(\tau) \exp(-2\pi i f \tau) d\tau. \tag{2.61}$$

In order to find the temporal autocorrelation function we will need to invoke the Taylor Hypothesis of frozen turbulence (Taylor, 1937). This states that, since the time scales of eddy motion are smaller than the frequencies of interest, we may move from the spatial to the temporal domain by assuming that a basically 'frozen' piece of turbulent air is being moved through the wavefront by a wind with a perpendicular velocity of $v_\perp$. Thus the knowledge of the spatial characteristics of air turbulence derived in the previous section can be used to study temporal behaviour. The component of wind velocity parallel to the direction of propagation will be assumed not to affect the temporal statistical properties of the wavefront entering the aperture. Unlike most of the previous work in this area, and following the method described by Noll (1976), most of

the calculations will be performed in Fourier space rather than in real space. This has the effect of introducing a number of delta functions, thereby making many of the integrals much easier to calculate.

Combining the definition of the expansion coefficients given in equation (2.52) and explicitly adding the time dependence of the phase across the aperture, the temporal autocorrelation in equation (2.60) can be re-written in the form

$$C_{a_j}(\tau) = \int d\boldsymbol{\rho} \int d\boldsymbol{\rho}'\, W(\rho) Z_j(\boldsymbol{\rho})\, C_\varphi(R\boldsymbol{\rho}, R\boldsymbol{\rho}', \tau)\, W(\rho') Z_j(\boldsymbol{\rho}') \tag{2.62}$$

where the integral now contains the autocorrelation function of phase

$$C_\varphi(R\boldsymbol{\rho}, R\boldsymbol{\rho}', \tau) = \langle \varphi(R\boldsymbol{\rho}, t) \varphi(R\boldsymbol{\rho}', t+\tau) \rangle. \tag{2.63}$$

Using the power law (Bracewell, 1986) on both the $\boldsymbol{\rho}$ and $\boldsymbol{\rho}'$ variables, equation (2.62) can be written in Fourier space as

$$C_{a_j}(\tau) = \int d\mathbf{k} \int d\mathbf{k}'\, Q_j^*(\mathbf{k})\, \Phi(\mathbf{k}, \mathbf{k}', \tau)\, Q_j(\mathbf{k}') \tag{2.64}$$

where $\Phi(\mathbf{k}, \mathbf{k}', \tau)$ is the spatial Fourier transform of $C_\varphi(R\boldsymbol{\rho}, R\boldsymbol{\rho}', \tau)$ with respect to both $\boldsymbol{\rho}$ and $\boldsymbol{\rho}'$. Denoting this transform by a solid line above the function and following Noll (1976) we obtain

$$\overline{C_\varphi(\boldsymbol{\rho}, \boldsymbol{\rho}', 0)} = \Phi_\varphi(\boldsymbol{\kappa}) \delta(\mathbf{k} - \mathbf{k}') = 0.023 \left(\frac{1}{r_0}\right)^{\frac{5}{3}} k^{-\frac{11}{3}} \delta(\mathbf{k} - \mathbf{k}'). \tag{2.65}$$

This is a direct consequence of equation (2.50) and the auto-correlation theorem described in equation (2.61). If the two spatial wave numbers $\mathbf{k}$ and $\mathbf{k}'$ have the same value, $C_\varphi(\boldsymbol{\rho}, \boldsymbol{\rho}', 0)$ is the spatial autocorrelation of the phase across the aperture whose Fourier transform is the spatial power spectrum given by equation (2.50). If the spatial wave numbers are not the same, turbulence theory gives us no information about $C_\varphi(\boldsymbol{\rho}, \boldsymbol{\rho}', 0)$ and we therefore introduce the delta function shown in equation (2.65). Any other model for turbulence could be used at this point as long as it supplies an expression for the spatial power spectrum for phase at ground level. More complex models for these spectra have been published (Tyson (1991), Tatarski (1961) and Tatarski (1971)) and could be substituted for the Kolmogorov spectra used here. The assumption of the inertial subrange means the Kolmogorov spectra will not produce the correct results for very high frequencies. As we are primarily interested in the low frequency behaviour, to aid in servo design, the Kolmogorov spectra will be used in this analysis.

By the similarity theorem (Bracewell, 1986) we find that

$$\overline{C_\varphi(R\boldsymbol{\rho}, R\boldsymbol{\rho}', 0)} = 0.023 \left(\frac{R}{r_0}\right)^{\frac{5}{3}} k^{-\frac{11}{3}}\, \delta(\mathbf{k} - \mathbf{k}'). \tag{2.66}$$

We now invoke the Taylor hypothesis by assuming that the temporal autocorrelation function is related directly to the spatial autocorrelation function assuming an average perpendicular wind speed $v_\perp$ via

$$\langle\varphi(R\rho,t)\varphi(R\rho',t+\tau)\rangle = \langle\varphi(R\rho,t)\varphi(R(\rho'-v_\perp\tau/R),t)\rangle. \tag{2.67}$$

Note that, as we have assumed local isotropy, we have dropped the vector notation for ρ and ρ'. By using the shift theorem of Fourier transforms (Bracewell, 1986) we can now write the required transform

$$\Phi(\mathbf{k},\mathbf{k}',\tau) = 0.023\left(\frac{R}{r_0}\right)^{\frac{5}{3}}\exp(-2\pi i v_\perp\tau k/R)\,k^{-\frac{11}{3}}\,\delta(\mathbf{k}-\mathbf{k}'). \tag{2.68}$$

Combining equations (2.58), (2.64) and (2.68) we arrive at an expression for the temporal autocorrelation function of the jth mode of the Zernike polynomial expansion of the wavefront across the aperture due to Kolmogorov turbulence. Due to the delta function in equation (2.68) the integral over $\mathbf{k}'$ becomes trivial, as is the integral over the angular part. The final expression becomes

$$C_{a_j}(\tau) = \frac{0.046}{\pi}\left(\frac{R}{r_0}\right)^{\frac{5}{3}}\int dk\,\exp(-2\pi i v_\perp\tau k/R)\,k^{-\frac{8}{3}}\,\frac{J^2_{n+1}(2\pi k)}{k^2}. \tag{2.69}$$

Note that the effect of the Taylor hypothesis is to introduce a periodic envelope function to the transform, whose frequency depends on the aperture radius R, the average wind speed $v_\perp$ and the time τ, and is given by $v_\perp\tau/R$.

It remains to perform a Fourier transform of this expression to find the power spectrum of the selected mode. As the only part of equation (2.69) containing a time dependence is the periodic exponential function, by swapping the order of integration we need only consider the transform of this part. Noting further that the power spectrum must be real and is undefined for negative frequencies, we write

$$\begin{aligned}\int df\exp(-2\pi i v_\perp\tau k/R)\exp(-2\pi i f\tau) &= \delta(f-v_\perp k/R)\\ &= R/v_\perp\delta(k-Rf/v_\perp).\end{aligned} \tag{2.70}$$

Substituting equations (2.69) and (2.70) into equation (2.61) we find that

$$W_{a_j}(f) = 0.092\,(2\pi)^{\frac{11}{3}}\left(\frac{R}{r_0}\right)^{\frac{5}{3}}\frac{R}{v_\perp}\,(n+1)\left(\frac{f}{f_0}\right)^{-\frac{8}{3}}\,\frac{J^2_{n+1}(f/f_0)}{(f/f_0)^2} \tag{2.71}$$

where $f_0 = v_\perp/(2\pi R)$. This equation is the main result of this Chapter and will be used in later sections to establish r_0 estimates by fitting this equation to experimental data. Note that no integrals remain and that C_N^2 does not appear in this expression, in contrast to similar work by Hogge and Butts (1976). The

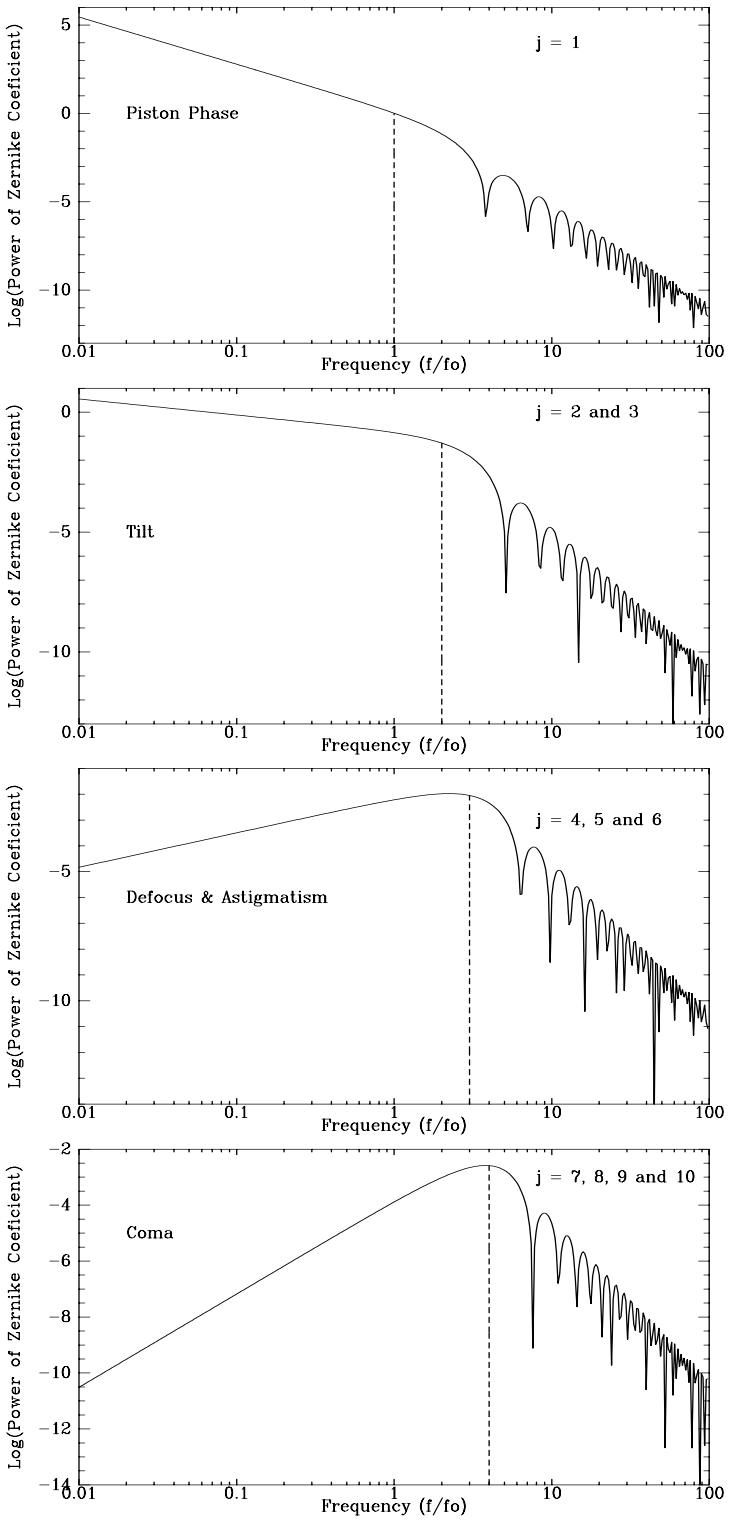

Figure 2.2: The power spectra for the first eight Zernike expansion coefficients for Kolmogorov turbulence. Note that most of the power is contained in the first three modes and that in all modes the majority of energy is contained in the low frequency range. The 'knee frequency' is marked in each plot with a dotted vertical line and increases with increasing mode number. In the high frequency end of all modes the oscillatory behaviour is not properly displayed due to the numerical nature of the calculations. Each minimum should reach zero.

first ten modes are plotted in figure (2.2). This figure demonstrates the main properties of these spectra. To begin with, the shape of the power spectrum depends only on the value of the azimuthal frequency (n value) of the given mode and not on the radial degree (m). This, though little else, is in agreement with the results derived by Hogge and Butts (1976). This paper seems to have become a starting point for many other works in this area, although the results are in conflict with the work contained in this thesis and of other workers (Tango and Twiss (1980) and Greenwood and Fried (1976)). Another discrepancy is the simple power law relationships often used to model these spectra. Given that the Bessel function in equation (2.71) can be approximated by (Palmer et al, 1990)

$$J_\nu(x) \sim \begin{cases} \frac{1}{\Gamma(\nu+1)}\left(\frac{1}{2}x\right)^\nu & \text{for} \quad 0 < x << \nu \\ \frac{2^{1/3}}{3^{2/3}\Gamma\left(\frac{2}{3}\right)}\nu^{-1/3} & \text{for} \quad x = \nu \\ \sqrt{\frac{2}{\pi x}}cos\left(x - \frac{1}{2}\nu\pi - \frac{\pi}{4}\right) & \text{for} \quad x >> \nu, \end{cases} \tag{2.72}$$

the power spectra given in equation (2.71) can be approximated by the following power laws:

$$W_{a_j}(f) \propto \begin{cases} f^{(6n-8)/3} & \text{for} \quad f << (n+1)f_0 \\ f^{-17/3} & \text{for} \quad f >> (n+1)f_0. \end{cases} \tag{2.73}$$

Thus, the 'knee' frequency, which will always be a harmonic of f_0, increases with increasing mode. For low frequencies the slope of the power spectra in the log domain will depend on the azimuthal frequency, for piston phase this will be $-\frac{8}{3}$, in agreement with Greenwood and Fried (1976), Tango and Twiss (1980), Hogge and Butts (1976), Clifford (1971) and Greenwood (1977). For tilt spectra the power law for low frequencies will be $-\frac{2}{3}$. This is the same as that predicted by Tango and Twiss (1980) and Greenwood and Fried (1976) but is in conflict with Hogge and Butts (1976) who also predict a $-\frac{8}{3}$ power law for tilt spectra. As will be shown in Chapter 5, experimental evidence indicates the $-\frac{2}{3}$ power law prediction best fits the data collected by the tilt correction servo. Hence, the formulae given by Hogge and Butts (1976) will not be used. For high frequencies the amount of power will drop very quickly with increasing frequency, that is, with a power law of $-\frac{17}{3}$. There is some argument in the literature about the correct slope for the high frequency part of the spectrum, however, as the total amount of power in this range is so small, this difference in models should have little or no effect on the data analysis to follow. A more complex turbulence model than the Kolmogorov spectra used herein would be required to model the high frequency behaviour correctly. The work by Tango and Twiss (1980) uses a different definition of tilt, an average phase gradient

across the aperture, and predicts a slope of $-\frac{11}{3}$. As will be shown in section (5.2) the $-\frac{11}{3}$ value agrees most closely with the experimental evidence.

A number of other points of interest concerning these power spectra should be mentioned. Firstly, the knee frequency depends on the perpendicular wind velocity $v_\perp$. Secondly, the total power in a spectrum (or the variance), as will be shown in the following section, depends only upon r_0. Fitting equation (2.71) to experimental data, by adjusting the values of $v_\perp$ and r_0, makes it possible to obtain an estimate for both of these parameters. The wind speed value is not generally of great interest to the astronomer except for high wind speeds which produce large bandwidths of aberration fluctuations. Generally, an estimate of r_0 is useful as a measure of seeing and, in the case of SUSI, aids in the selection of appropriate aperture sizes during an observational run. Finally, the power spectra derived show that the tilt servo need not have a bandwidth larger than a few tens of hertz. A bandwidth larger than the knee frequency defined above may prove to be disadvantageous, as such a servo bandwidth would only result in noise amplification. In the tilt servo system for SUSI the bandwidth of the feedback control system will be tuned to the knee frequency measured for a particular observation.

2.3.3 Variance of Wavefront Distortions

The variance of any Zernike coefficient is given by the total power in its spectrum, that is,

$$\sigma_{a_j}^2 = \int_0^\infty df W_{a_j}(f). \tag{2.74}$$

Substituting equation (2.71) and using the variable change $k = Rf/v_\perp$ the variance of any given Zernike coefficient will be

$$\sigma_{a_j}^2 = \frac{0.046}{\pi}\left(\frac{R}{r_0}\right)^{\frac{5}{3}}(n+1)\int_0^\infty dk\, k^{-\frac{8}{3}}\,\frac{J_{n+1}^2(2\pi k)}{k^2}. \tag{2.75}$$

This is in exact agreement with the more general expression for the covariance of the expansion coefficients derived by Noll (1976) and later corrected by Wang and Markey (1978):

$$\langle a_j a_{j'}\rangle = \begin{cases} \frac{0.046}{\pi}\left(\frac{R}{r_0}\right)^{\frac{5}{3}}\sqrt{(n+1)(n'+1)} & \\ \quad\times(-1)^{(n+n'-2m)/2}\delta_{mm'} & \\ \quad\times\int dk k^{-\frac{8}{3}}\frac{J_{n+1}^2(2\pi k)}{k^2} & \text{for } (j-j') \text{ even} \\ 0 & \text{for } (j-j') \text{ odd} \end{cases} \tag{2.76}$$

which will reduce to equation (2.75) when $j = j'$.

From inspection of equation (2.76) it is clear that the modes are not decoupled. The measurement of one coefficient may affect the measurement of another. This modal cross-coupling, however, only becomes a problem when higher order modes are being used or estimated (Herrmann, 1981). Work by Cubalchini (1979) has also shown that by minimising the number of modes estimated and only working with modes less than astigmatism ($j \leq 6$) the overall variance of the estimates will be as small as possible. As both of these criteria apply to the wavefront tilt servo of SUSI, this mode coupling will be ignored.

A final check of equation (2.75) can be performed by looking at the total power, or variance, of the wavefront tilt. By equation (2.59), angle of arrival scales as $\lambda/R\pi$. This means the power spectrum of tilt will scale as $(\lambda/R\pi)^2$ and putting $j = 2$ or 3 in equation (2.75) we can write the total power in the tilt spectrum as

$$\begin{aligned} \sigma^2_{tilt} &= \tfrac{0.092}{\pi^3} (\lambda/R)^2 (R/r_0)^{\frac{5}{3}} \int_0^\infty dk k^{-\frac{8}{3}} J^2_{n+1}(2\pi k)/k^2 \\ &= 0.183 (D/r_0)^{\frac{5}{3}} (\lambda/D)^2 \,\mathrm{rad}^2 \end{aligned} \tag{2.77}$$

where $D = 2R$. This is in excellent agreement with equation (70) in Greenwood and Fried (1976) and equation (B.13) in Tango and Twiss (1980). The variance expressed here can be related to the *seeing disc*, an expression often used by astronomers. If we define the seeing disc θ_{seeing} as the full width half maximum of a Gaussian function fitted to a histogram of image position in radians, we find that

$$r_0 = 1.009 D \left(\frac{\lambda}{\theta_{\text{seeing}} D} \right)^{\frac{6}{5}} \tag{2.78}$$

which shows that r_0 depends upon the wavelength to the power of $\frac{6}{5}$. Comparing this expression with equation (2.47), shows that the seeing disk size is independent of wavelength. This expression can also be interpreted to say that the coherence length, r_0, depends on the ratio of the Airy disc formed in the telescope to the size of the seeing disc. When these are the same the coherence length is equal to the diameter of the telescope. For larger wavelengths the size of the airy disk increases, therefore one expects seeing to be better at longer wavelenghts. The dependence of r_0 on the aperture diameter is much smaller than wavelength or Airy disc size, indeed for apertures of the order of one metre this expression can be approximated by

$$r_0 \sim \left(\frac{\lambda}{\theta_{\text{seeing}}} \right)^{\frac{6}{5}}. \tag{2.79}$$

So at a wavelength of 500nm, a seeing disc of 1" corresponds to an r_0 value of around 10cm. We will be using the wavelength of 440nm in most of the

calculations to follow as it is the reference wavelength used for all alignment of interferometer optics. At this wavelength, and for the aperture sizes used in SUSI, a 1" seeing disc corresponds to a coherence length of only 9.0cm.

With the expression for variance of a given mode, two other useful predictions can be made. Firstly, equation (2.75) will yield an alternative estimate of r_0 to that given by equation (2.71) and will serve as a test of the measurements proposed in the last section. Secondly, equation (2.75) will allow us to estimate the amount of residual wavefront distortion once the lowest order aberrations have been corrected. Once again following the work of Noll (1976), we define the correction of the first J modes of the wavefront to be

$$\varphi_C = \sum_{j=1}^{J} a_j Z_j. \tag{2.80}$$

We then define the mean square residual error to be

$$\Delta_J = \int d\rho W(\rho) \langle [\varphi(R\rho) - \varphi_C(R\rho)]^2 \rangle \tag{2.81}$$

and remembering that $\langle a_j \rangle = 0$ and substituting equation (2.80) we find that

$$\Delta_J = \langle \varphi^2 \rangle - \sum_{j=1}^{J} \langle |a_j|^2 \rangle, \tag{2.82}$$

where $\langle \varphi^2 \rangle$ is the phase variance. While this variance is infinite for Kolmogorov turbulence, due to the assumption of an inertial subrange, Noll (1976) shows that this is contained within the first, piston phase, term. All other terms are finite and easily calculated. The first ten values are given in table (2.2).

The same results were originally derived by Fried (1965) via a much more complicated technique. The implication of the residual errors given here is that if piston phase and both vertical and horizontal tilt are corrected for, only a small amount of wavefront distortion remains. We see then, that if the aperture is restricted to r_0 or less the wavefront can be considered to be well approximated by the first three Zernike coefficients: piston phase and horizontal and vertical tilt.

2.4 Implications for SUSI

The design of SUSI takes many of the problems of atmospheric turbulence into account. To begin with, the site chosen is on a plain, on which grass is encouraged to grow, thus reducing the number of nearby obstacles; the buildings

Mode	Residual error
Δ_1	$1.0299 \left(\frac{D}{r_0}\right)^{\frac{5}{3}}$
Δ_2	$0.582 \left(\frac{D}{r_0}\right)^{\frac{5}{3}}$
Δ_3	$0.134 \left(\frac{D}{r_0}\right)^{\frac{5}{3}}$
Δ_4	$0.111 \left(\frac{D}{r_0}\right)^{\frac{5}{3}}$
Δ_5	$0.0880 \left(\frac{D}{r_0}\right)^{\frac{5}{3}}$
Δ_6	$0.0648 \left(\frac{D}{r_0}\right)^{\frac{5}{3}}$
Δ_7	$0.0587 \left(\frac{D}{r_0}\right)^{\frac{5}{3}}$
Δ_8	$0.0525 \left(\frac{D}{r_0}\right)^{\frac{5}{3}}$
Δ_9	$0.0463 \left(\frac{D}{r_0}\right)^{\frac{5}{3}}$
Δ_{10}	$0.0401 \left(\frac{D}{r_0}\right)^{\frac{5}{3}}$

Table 2.2: The residual errors after correcting for the first ten modes are tabulated for Kolmogorov turbulence. D is the telescope diameter. The numbers in the table clearly show that, for a telescope of diameter r_0 or less, only the first three modes need be corrected to achieve a large improvement in optical quality. To gain much better improvement, many more modes need to be corrected for.

containing the OPLC, being of cylindrical design, contain no external sharp boundaries. Furthermore, the siderostats are positioned several metres above the ground and the beams enter a vacuum system as soon as is practicable, thereby saving them from the worst of the lower air turbulence. The prevailing winds at the site are from the east. All the buildings have therefore been placed on the western side of the baseline thereby further reducing their impact on local seeing.

As previously stated, in order to avoid many of the problems associated with seeing, the apertures in SUSI are restricted to r_0 or less and the first three Zernike modes, that is phase and both axes of tilt, are corrected. The residual wavefront phase error due to Kolmogorov turbulence during the final visibility measurements will then be of the order of 0.134 radians squared, or less. The aperture size used for visibility measurements will usually be less than r_0 implying even smaller phase errors. If larger apertures are used, higher order adaptive optics systems would be required and/or longer wavelengths would have to be used.

The temporal spectra derived above will help set limits on sampling times and bandwidths of the various devices and control systems in SUSI. The minimum sample time has therefore been set at 1ms, thereby ensuring that these devices, especially the tilt correction servo, will have the required speed.

Chapter 3

HARDWARE

The wavefront tilt correction servo is a digitally controlled negative feedback loop. A diagram of its major components can be found in figure (3.1). Each cycle the system performs the following functions:

- Measures the image position.
- Calculates a new mirror position that will centre the image.
- Places the mirror in this new position.

Systems like this are also referred to as *tip/tilt* servos, *fast tracking*, or *wobblers*. In order to meet the requirement specification set out in section (1.4) both the detectors and mirrors must have resolutions of a fraction of an arcsecond. Furthermore, to track an analogue phenomenon such as image position with a digital system the cycle time of detection, calculation and correction must be less than the time constant of the tilt fluctuations. The characteristic time of atmospheric turbulence t_0 is of order 10ms (Roddier, 1981) and has been measured to be as small as 3ms (Roddier et al, 1990). Therefore a minimum cycle time of 1 millisecond has been chosen. Sample times which are multiples of this minimum are also available.

The detectors used are called *optical pyramids* which are a type of *quadrant detector*. An optical pyramid splits the focussed image into four parts or quadrants with the light in each quadrant being separately detected. The image position is by definition centred on the detector when these four signals are equal in intensity, while an imbalance implies a centring error. The number of photon events registered in each quadrant is counted and latched by electronics and read

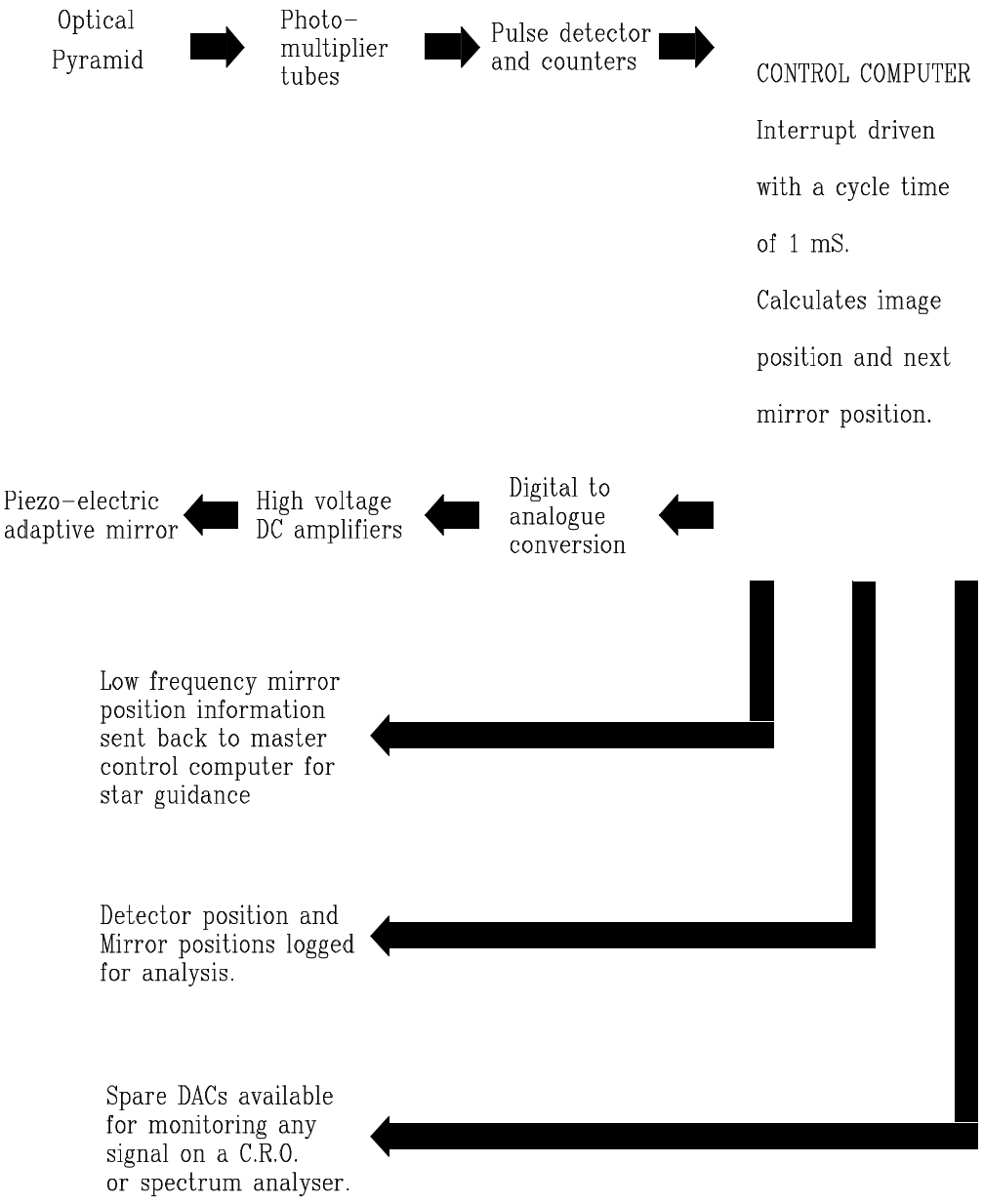

Figure 3.1: A block diagram of one tilt correction servo. The solid arrows indicate the flow of position information. Each box represents one functional part of the servo hardware.

every cycle. From these the image position is calculated and the appropriate signals are sent to the adaptive mirrors to re-centre the image.

The adaptive mirrors are normal flat mirrors mounted on three piezo-electric actuators arranged at the vertices of an equilateral triangle (see figure (3.9)). Moving the bottom two actuators in opposition tilts the mirror about a vertical axis, while moving these two actuators in parallel and in opposition to the top actuator results in a tilt about an horizontal axis. Calculations for the three piezo control voltages are performed electronically using two voltages; one representing vertical tilt and the other horizontal tilt.

3.1 The Optical Pyramids

The optical pyramids split the image of the star into four parts by focusing the stellar image onto two separate knife edges, one vertical and one horizontal. Each knife edge is created by a prism made from two optically contacted rhombs and constructed from BK-7 glass. Two lenses are also required to image the vertical edge of the detector onto the horizontal edge. The prisms, lenses and mounts were originally designed by Dr. W.J. Tango[1] and constructed for the prototype instrument (Davis and Tango (a), 1985). Refer to figure (3.2) for a drawing of the detector optics.

The entire optical pyramid is mounted on an x/y or vertical/horizontal platform which can be remotely motor driven. The motor drives have been installed on the two detectors used in the tilt servos for the north and south beams while the third 'reference' detector is in principle fixed and defines the optical axis of SUSI. An aluminium box houses the prism containing the horizontal edge and is screwed directly onto the x/y platform. This box has three small holes in the front, two for the beams issuing from the vertical edge and a central one for use during detector alignment. The back of the box has four output holes in a 70mm square. It is the light issuing from these holes that represents the four quadrants of the detector.

The prism containing the vertical edge is held in a kinematic mount which in turn sits on a block clamped to the x/y platform. In this way the vertical edge can be correctly aligned with the horizontal edge. The two small lenses that image the vertical edge onto the horizontal edge are held in bracket between the

[1]The pyramid design was based on the pyramids used in an interferometer which was originally built by R Q Twiss at the National Physics Laboratory (UK) and later rebuilt at the Italian outstation of the Royal Observatory, Edinburgh

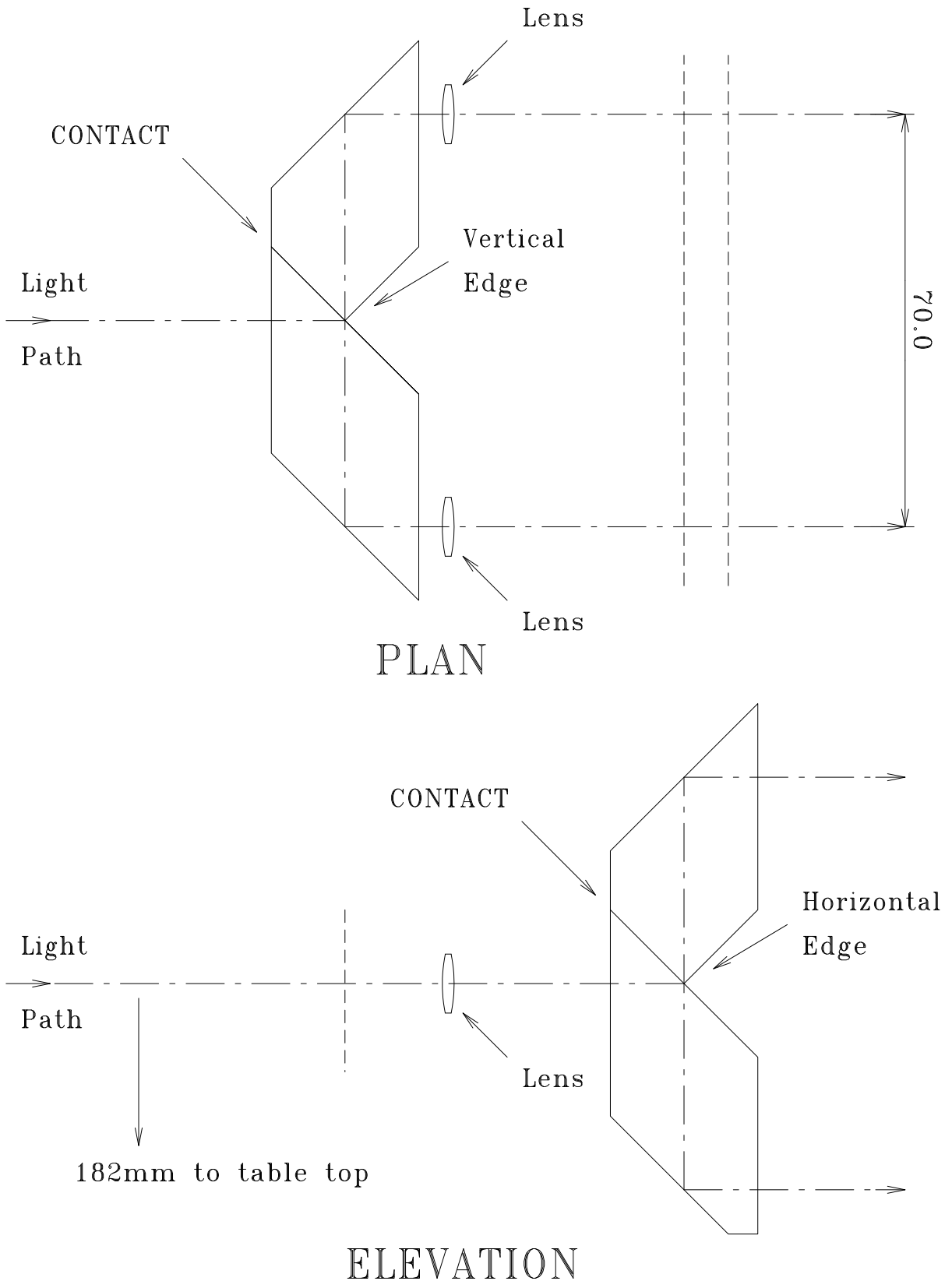

Figure 3.2: Full size plan and elevation of quadrant detector optics. The dashed line represents the light path through the optical system.

two prisms. Figure (3.3) contains some pictures of a completed optical pyramid.

There are a number of reasons for choosing a photomultiplier based quadrant detector. First of all, as little light is available, the system has to have the highest quantum efficiency possible. This means photon counting array detectors, such as the PAPA camera (Papaliolios and Mertz, 1982), would not be suitable. In a quadrant detector the light is split into only four pixels, thus ensuring the maximum illumination, and therefore signal to noise ratio, in each pixel. Secondly, systems like optical pyramids use knife edges ensuring a minimal dead zone on the detectors, which can be a severe restriction to other quadrant cell systems (Tyson, 1991). Furthermore, the system must be fast, due to the very short (1ms) cycle time. This rules out CCD based systems due to their comparatively long readout time. Silicon avalanche photodiodes can now achieve high quantum efficiency in the red (Nightingale, 1991), so they would be good candidates for use on the red light optical table.

The thesis by Buscher (1988) contains an excellent discussion of these problems. In particular he shows in Chapter 5 that a quadrant cell detector is the optimal linear estimate for image position given a noisy input signal. He goes on to show, via a number of numerical simulations, that the knife edge criterion used by the quadrant detector performs as well as the *centroid* criterion which equates the centre with the centre of gravity of the image. Atmospheric noise, that is, the remaining Zernike coefficients of the wavefront after tilt has been corrected, is also discussed and tested by numerical simulation and is shown to contribute no more than 30% to the error of beam tilt measurement. As the analysis in section (2.3.3) shows, this error is never large and we may therefore neglect this effect.

3.1.1 Initial Optical Alignment of the Quadrant Detectors

The alignment procedure of the optical pyramids must ensure:

- The image is properly focussed onto both knife edges. If the image is not correctly focussed the detector sensitivity will be reduced.
- The optical axes are normal to the prism surfaces. Since the knife edges are within glass, dispersion will result in the image being spread across the knife edge if the light is not incident normally. This will also reduce

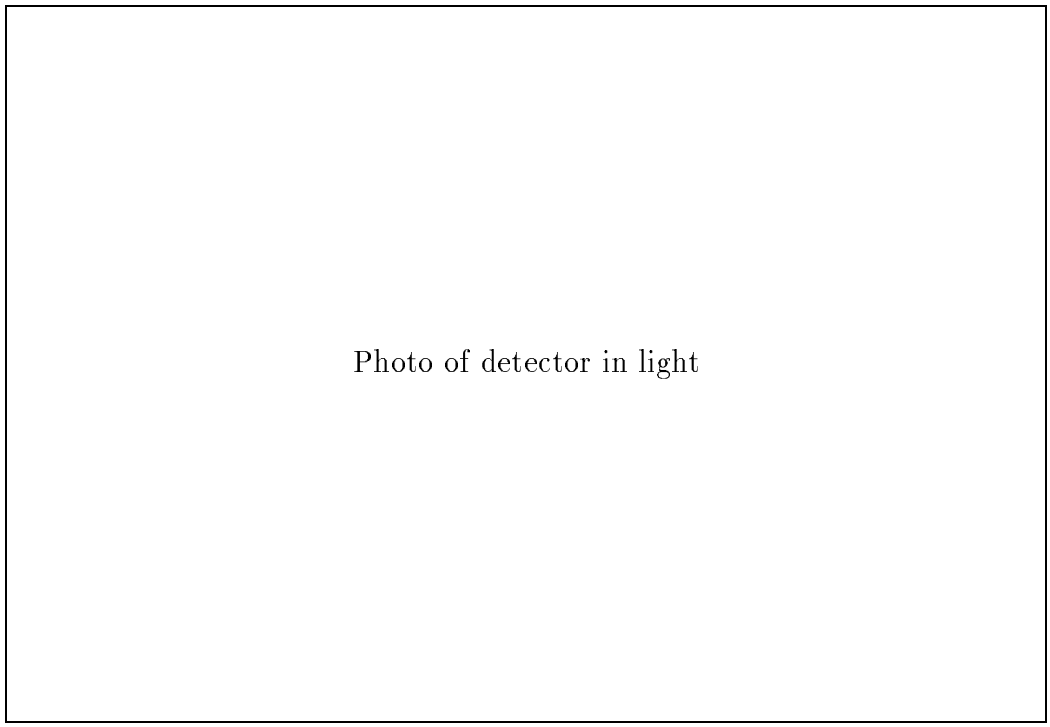

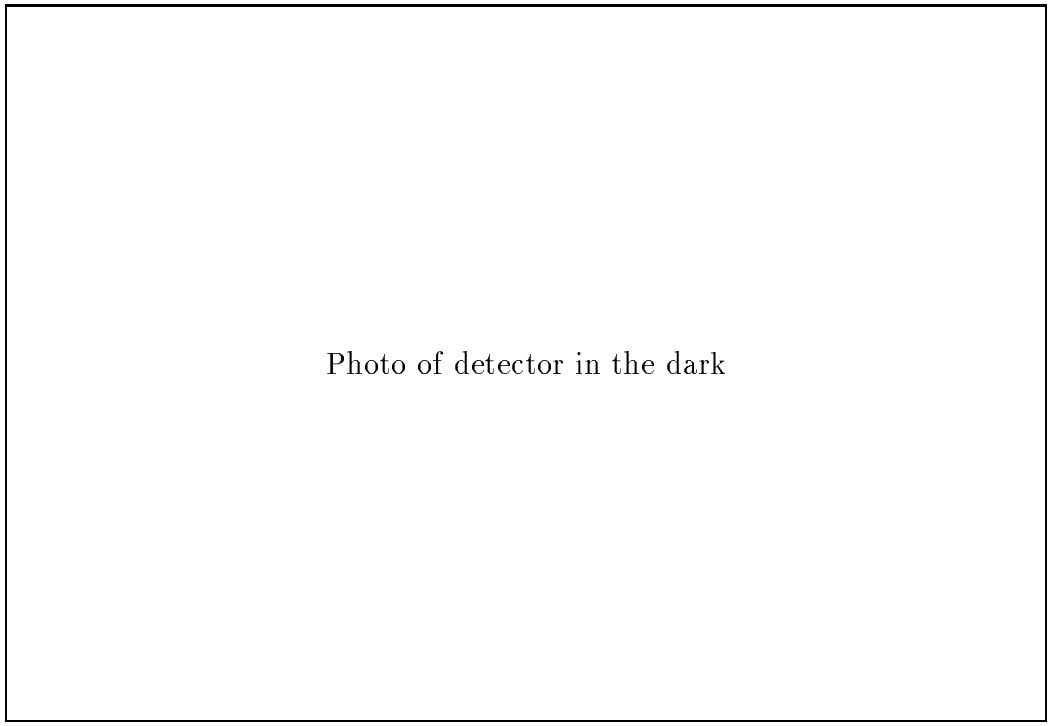

Figure 3.3: An assembled optical pyramid shown with full lighting (top) and in operation (bottom). The quadrant detectors or 'pyramid' prisms break the star image up into four sections. The image is centred when the amount of light in each quadrant is equal.

detector sensitivity.

- The horizontal edge is parallel to the optical table surface and at the correct height.
- The vertical edge is normal to the horizontal edge.

A detailed description of the alignment procedure can be found in Appendix A. The optical alignment of the detectors was performed with the detectors on the optical table in the positions in which they would eventually be clamped and used in the interferometer. As the detector response is wavelength dependent, the alignment was performed using blue light from the reference laser. Once the alignment procedure was completed with blue light the detectors were tested using a white light source. No measurable difference could be found between the two light sources.

3.1.2 Alignment of the Optical Axes

The quadrant detector alignment procedure outlined above need only be performed once, while the alignment of the optical axes of the interferometer must be checked prior to, and during, each observational run. Unless the two beams of the interferometer are correctly aligned it will not be possible to observe fringes. This procedure is not essential to the tilt servo described in this thesis but as the quadrant detectors play an important role it will be briefly described here. Refer to the optical layout of SUSI presented in figure (1.1). The blue laser is once again used as a reference light source.

The axes alignment procedure begins by ensuring that both beams are parallel to the rails of the OPLC and at the correct height to enter the OPLC fine carriage. If this is not the case the entry holes of the carriage can cause vignetting, which will vary as the carriage moves along the rails. This part of the alignment is tested by inserting a target into the beam at various locations along the OPLC track and is corrected by adjusting the mirrors on the optical table side of the OPLC.

In the second stage the alignment of the two beams with the BRT is checked. The initial adjustment of the mirrors in the vacuum system, performed when they were installed, ensures that if the beams are correctly entering the BRT they will reach all the way out to the siderostats. Once again targets are used, one at the output to the BRT and another at the beginning of the vacuum

system. The beams are adjusted by moving the mirrors on the BRT side of the OPLC until they are centred on both targets.

Once the two beams are parallel to the OPLC rails, passing through the carriage and BRT without vignetting and entering the vacuum system a large mirror is placed in front of the BRT to autocollimate both beams. The OPLC carriage is moved so that high contrast tilt fringes can be observed at the beamsplitter and the mirrors nearest the BRT adjusted to minimise these fringes. This ensures that the images formed are optically superimposed on the optical table. An iterative process is sometimes required to satisfy all alignment criteria as this adjustment can disturb the previous two stages of alignment.

These three procedures ensure that the two beams are correctly aligned with the OPLC, the BRT and each other. At this point the position of the reference quadrant detector is checked. After attenuating the laser light the quadrant detectors are switched on and the position of the two beams on the reference detector is monitored. Occasionally the reference detector needs to be moved slightly to ensure both beams are centred on the optical pyramid. The north and south detectors are also aligned with the laser light. This completes the setup alignment and, after removing the autocollimating mirror, the interferometer is ready for a night's run.

It is also necessary to check beam alignment periodically throughout the night. This is done by checking each of the two beams against the reference detector. With the tilt servo locked onto a star, the position of each beam is measured on the reference detector, one at a time. If a beam is not correctly centred the motor drives on the optical table are used to move the appropriate optical pyramid to re-centre it. Since the tilt servo locks the stellar image onto the optical pyramid, moving the detector amounts to moving the entire beam. In this way any drift in the system can be corrected.

3.1.3 Response of Detectors

When viewed from the direction of the incoming beam the quadrants are labelled as shown in figure (3.4). We therefore define the normalised image position as

$$\begin{aligned} \theta_h &= \frac{(\mathcal{N}_\mathcal{A} + \mathcal{N}_\mathcal{B}) - (\mathcal{N}_\mathcal{C} + \mathcal{N}_\mathcal{D})}{(\mathcal{N}_\mathcal{A} + \mathcal{N}_\mathcal{B} + \mathcal{N}_\mathcal{C} + \mathcal{N}_\mathcal{D})} \\ \theta_v &= \frac{(\mathcal{N}_\mathcal{A} + \mathcal{N}_\mathcal{D}) - (\mathcal{N}_\mathcal{B} + \mathcal{N}_\mathcal{C})}{(\mathcal{N}_\mathcal{A} + \mathcal{N}_\mathcal{B} + \mathcal{N}_\mathcal{C} + \mathcal{N}_\mathcal{D})} \end{aligned} \tag{3.1}$$

A	D
B	C

Figure 3.4: Definition of quadrant detector channels as viewed from the front of the quadrant detector.

where $\mathcal{N}_{\mathcal{A}...\mathcal{D}}$ are the weighted number of photon events detected in the four quadrants (refer to section 3.3.1 for an explanation of weighting factors) during the last sample period and θ_h and θ_v are the normalised horizontal and vertical image positions. If there are no photons detected the position is defined to be zero in both axes.

As this detector system has identical geometry in both the vertical and horizontal axes we shall only consider the response of the vertical axis. The results for the horizontal follow in an identical manner. After passing through a defining aperture of radius R the beam is focussed onto the optical pyramid prisms. Treating the star as a point source, so Fraunhofer diffraction conditions will apply, results in an Airy disc on the prism surface. Following Born and Wolf (1987), section 8.5.2, we write the intensity distribution of this Airy disc as

$$I(v) = I_0 \left(\frac{2J_1(v)}{v} \right)^2 \tag{3.2}$$

where

$$I_0 = \left(\frac{\pi a^2 |A|}{\lambda f^2} \right)^2 \tag{3.3}$$

and

$$v = k \frac{R}{f} r. \tag{3.4}$$

In this expression $J_1(x)$ is the first order Bessel function, k is the wavenumber $(\lambda/2\pi)$, f is the lens focal length, r is the distance from the optical axis and A is the light amplitude in the lens plane. If there is no tilt in the beam this pattern should be centred on the quadrant detector resulting in an output of zero. If the beam is tilted at an angle θ the centre of the Airy disc will be displaced by an amount $f\theta$ which, after substituting for r in equation (3.4), results in

$$v = kR\theta. \tag{3.5}$$

Note that the position of the Airy disc is independent of the focal length of the lens. A long focal length was therefore used to minimise aberrations due

to refractive surfaces of high curvature. These lenses were optimised for use at approximately 440nm[2]. Taking the Airy disc centre as (x_0, y_0) in the plane of the detector, in which the origin $(0,0)$ is the detector centre (ie, $v = y_0$), the total intensity above the x-axis for a given value of y_0 will be

$$I_{\text{total}}(y_0) = \int_{-\infty}^{\infty} dx \int_{0}^{\infty} dy I_0 \frac{4J_1^2\left(\sqrt{x^2 + (y-y_0)^2}\right)}{x^2 + (y-y_0)^2}. \tag{3.6}$$

We now re-write the detector output θ_v defined in equation (3.1) as

$$\theta_v(\theta) = \frac{I_{\text{total}}(ka\theta) - I_{\text{total}}(0)}{I_{\text{total}}(0)}, \tag{3.7}$$

which is the theoretical detector response θ_v for a given wavefront tilt θ. Note that the intensity of light in the beam cancels and the result depends only on the wavelength of the light, the aperture radius and wavefront tilt. Unfortunately the integral defined in equation (3.6) cannot be easily performed analytically; however, for specific cases of aperture size, wavelength and beam tilt, a numerical calculation can produce the desired result. Such a numerical calculation, based on the Romberg Integration method (Palmer et al, 1990)[3], was performed for the reference laser wavelength of 442nm and for a range of aperture sizes available on SUSI. These calculations are displayed in figure (3.5).

Figure (3.5) clearly demonstrates that when the position of the star image is close to the origin the response of the detector is very linear. The linearity of the function decreases as the image moves further away from the origin. When the servo is working one can assume the image must remain close to the origin, thus all calculations involving detected positions will be of the form

$$\phi_v = K_d \theta_v \tag{3.8}$$

where ϕ_v is the beam tilt in arcseconds and K_d is a calibration constant. Under these conditions, the integrand in equation (3.6) can be expanded and solved to give (Tyler and Fried, 1982)

$$K_d = \frac{3\pi}{32}\frac{\lambda}{R}. \tag{3.9}$$

For example, with an aperture radius of 17.5mm on the optical table and a wavelength of 442nm the resulting calibration factor is $K_d = 1.53$ arcsec. This equation yields the slope of the functions plotted in figure (3.5) near the origin. Due to photon noise and inevitable servo errors, the detectors will not always be

[2]R.J. Thompson and W.J. Tango, unpublished internal report.

[3]Since this integral is two dimensional, these calculations took very long times to complete. Several months of computer time was used in producing these results.

Aperture Radius	Cutoff Point	K_d
10.0 mm	1.85 arcsec	2.90 ± 0.02 arcsec
12.5 mm	1.60 arcsec	2.37 ± 0.02 arcsec
15.0 mm	1.40 arcsec	2.00 ± 0.02 arcsec
17.5 mm	1.20 arcsec	1.71 ± 0.02 arcsec
20.0 mm	1.00 arcsec	1.48 ± 0.02 arcsec
Average		2.1 ± 0.4 arcsec

Table 3.1: Using the detector response curves in figure (3.5) calibration constants are tabulated above for a range of aperture sizes at a wavelength of 442nm. These numbers are the result of a linear regression on the central, linear, part of the detector response curves. The average value shows that the calibration constant K_d should be of order 2. Note that these values apply to the detectors on the optical table. Due to the BRT, to get an equivalent value for measurements on the sky one must divide these numbers by three.

operating very close to the origin at all times. An estimate more appropriate for experimental situations can be found by performing a regression on the 'linear' part of the detector response curves. The results of such fits are shown in table (3.1). The servo analysis presented in Chapter (4) will show that the final fitted value for K_d is very close to this predicted value.

In order to test the detector response, the same optical configuration as that used to align the detectors (see Appendix A) was used. With neutral density filters in place to reduce the light intensity so that the photomultipliers could be switched on, the image position as defined in equation (3.1) was monitored while a low level sine wave was sent to the tilt mirrors. The frequency of the sine wave was 1 Hz and the amplitude was set so the signal stayed well within the range of the detectors. A sample of the results is shown in figure (3.6) along with a least squares fit of the data. The RMS residual after fitting was 0.05 which corresponds to 0.1". This same experiment was performed on all detectors and axes with similar results. These fitted sine waves allow the estimation of the calibration constants if the mirrors have been calibrated (see section 3.2.2). The results are shown in table (3.2) and display an average detector calibration constant of 2.5 ± 0.2 in good agreement with the theoretical prediction of equation (3.9). While a precise calibration of the detectors is not required for the tilt servo to work or for meaningful results to be obtained, this rough calibration will be of benefit for the noise analysis to follow and for the servo analysis in Chapter 4.

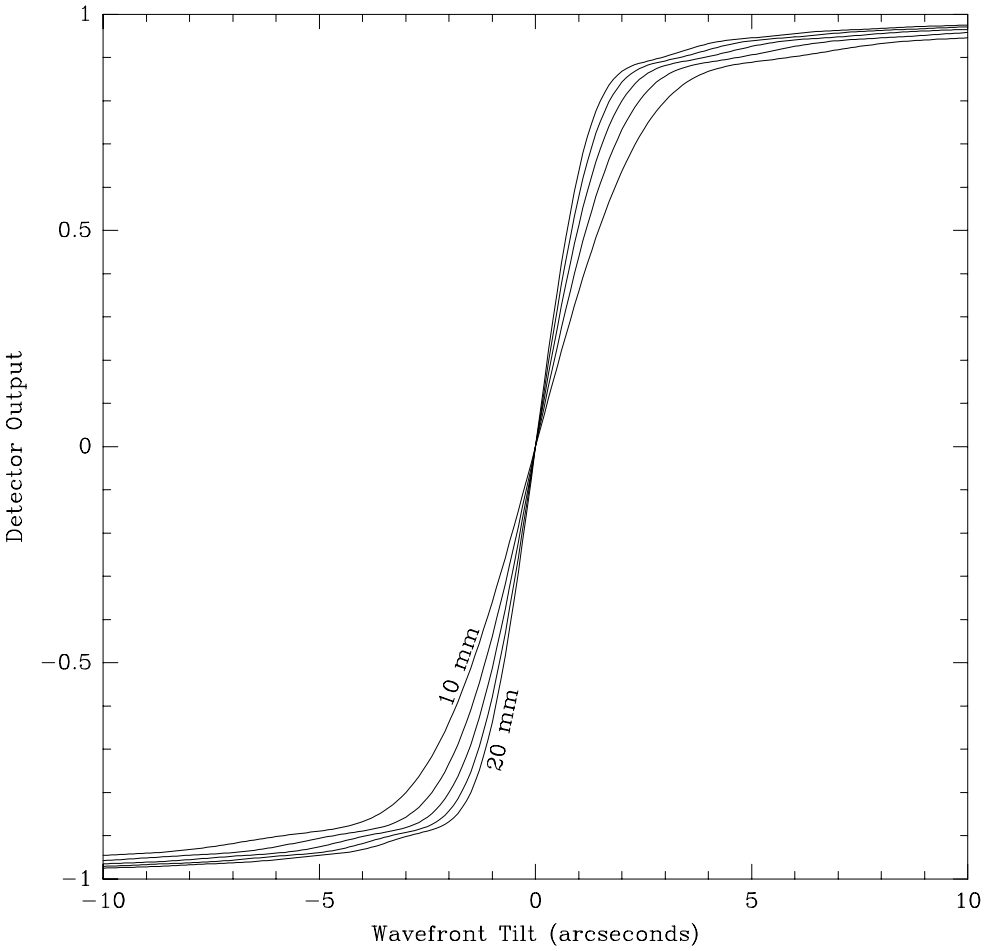

Figure 3.5: The theoretical response of one axis of a 'perfect' quadrant detector for aperture radii 10, 12.5 15, 17.5 and 20mm, all available sizes on SUSI. Inside the centre of the range the response is very close to linear. It is this linear range near the origin that is used for the image position servo. It is also possible to see the effects of the inner rings of the Airy disc, as they cross the defining edge. The data were calculated using equation (3.7) by numerical methods.

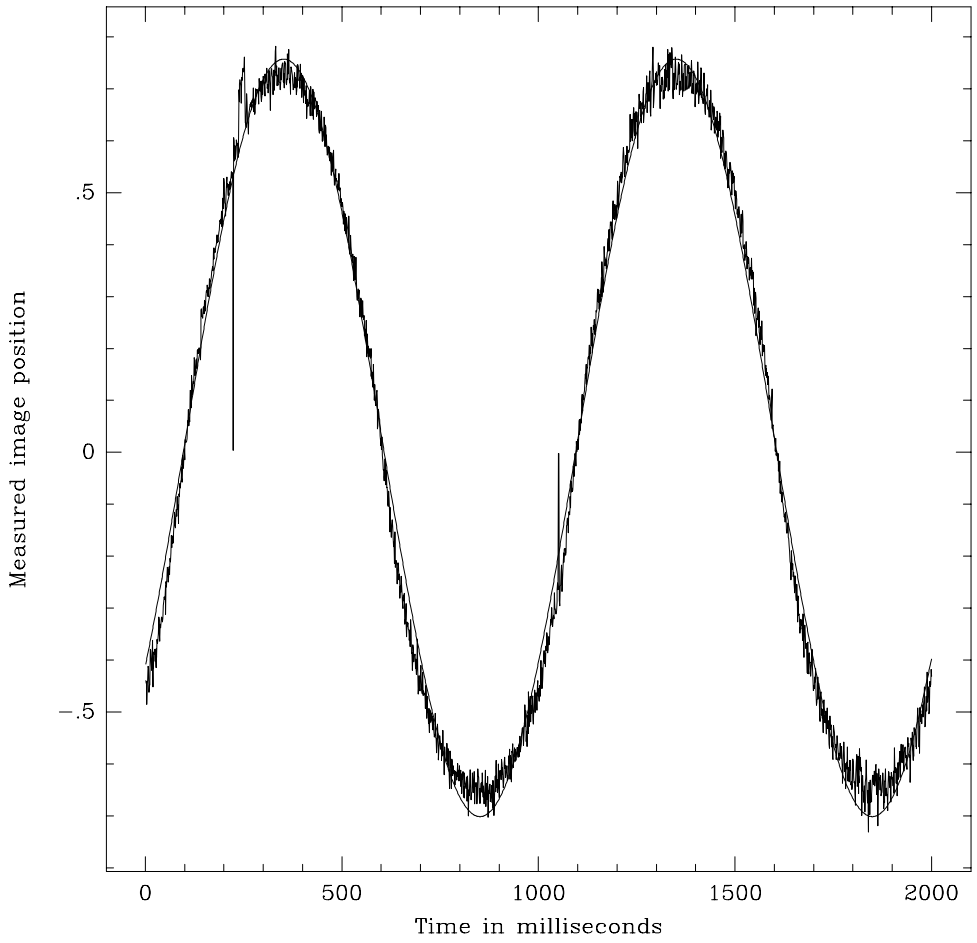

Figure 3.6: Measured response of one axis of a quadrant detector given a 1Hz sine wave input. The smooth line is a least squares fit of a sine wave to the data. It is clear the response of the detector is very close to linear, as predicted. The noise represents an angular variation of less than 0.1". The large spikes in the plot above were due to software timing errors which have since been corrected.

This rough calibration also confirms that the optical alignment of the detectors is satisfactory since any alignment error would show up as a reduction in detector sensitivity.

3.1.4 Detector Signal to Noise

The error associated with angular position measurements using quadrant detectors, as well as for other optical detectors used for adaptive optics, has been well studied (Tyler and Fried (1982), Dyson (1975) and Walkup and Goodman (1973)). The expression for the error term associated with the quadrant

Detector Axis	K_d
North Vertical	2.30 ± 0.02 arcsec
North Horizontal	2.25 ± 0.02 arcsec
South Vertical	2.56 ± 0.02 arcsec
South Horizontal	2.68 ± 0.02 arcsec
Average	2.5 ± 0.2

Table 3.2: After sending a sine wave of known amplitude to the mirrors the resulting detector output using a 35mm diameter aperture was fitted with a sine wave in the least squares sense. The amplitude of the fitted sine wave could then be compared to the mirror movement amplitude to produce the detector calibration constants listed above. Comparison with equation (3.9) indicates that these results are in good agreement with the theoretical predictions.

detector, as derived by Tyler and Fried (1982), is

$$\sigma_\phi = \pi \left[\left(\frac{3}{16} \right)^2 + \left(\frac{n}{8} \right)^2 \right]^{\frac{1}{2}} \frac{\left(\frac{\lambda}{D} \right)}{\text{SNR}} \tag{3.10}$$

where n is the angular subtense of the object divided by the diffraction angle (λ/D) of the optical system, D is the aperture diameter and SNR is the signal to noise ratio of the four detectors summed to act as a single detector. In the system under discussion here the star is unresolved and we therefore say $n \ll 1$. The signal to noise ratio of the four detectors summed is primarily dependent upon the Poisson statistics of the photon events so we can write the error in angular position measurement of the quadrant detectors as

$$\sigma_\phi = \frac{\pi \frac{3}{32} \left(\frac{\lambda}{R} \right)}{\sqrt{N}} \tag{3.11}$$

where N is the total number of counts received in all four quadrants. Using highly attenuated laser light this expression was tested with the same system used to align the detectors (see Appendix A). By varying the aperture size, neutral density filters and sampling rates, several two second samples were taken of detector response for a range of light intensities. The resulting data were Fourier transformed, the low spatial frequencies attenuated, and inverse transformed back to the spatial domain. These operations were performed in order to filter out any underlying motion of the beam due to internal thermal and turbulent effects. Once filtered, the variance of each sample was calculated and compared to a prediction using equation (3.11) (See figure (3.7)). This plot

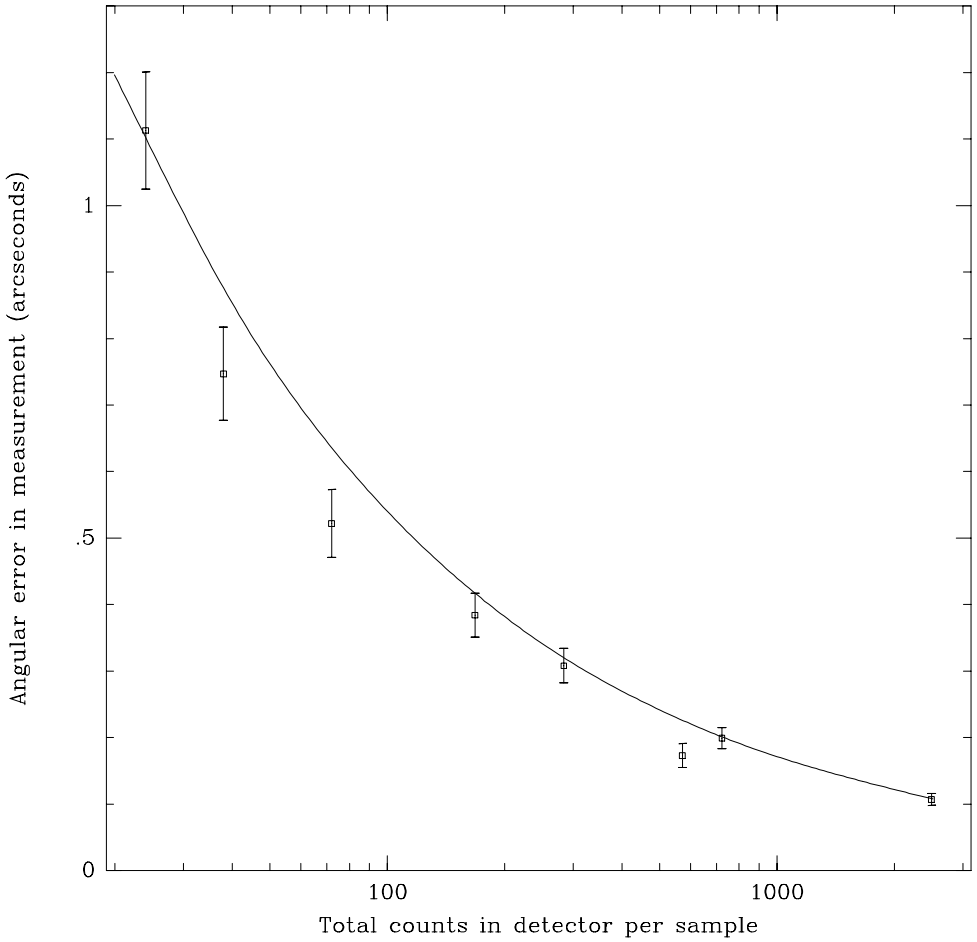

Figure 3.7: The solid line in the plot above represents the theoretical variance of detected position in a quadrant detector as stated in equation (3.11). The points plotted are measured values with the error bars representing the uncertainty in detector calibration. Correspondence is good, giving us confidence in the analytical expression.

demonstrates that equation (3.11) can be used to estimate the error in angular position detection of the quadrant detectors.

3.2 The Adaptive Mirrors

To correct wavefront tilt in an incoming collimated beam adaptive mirrors are required which can be set to any angular position under computer control. As with the pyramids, the mirrors were originally made for the prototype stellar interferometer. The adaptive mirror system consists of a normal flat mirror mounted on three piezo-electric actuators arranged at the vertices of an equilateral triangle. By sending the correct signals to these piezo-electric actuators the mirror can be tilted in any direction desired. A plate with three vertical adjustable screws holds the entire mirror assembly so the central mirror position can be correctly aligned with the rest of the optical system. Small ball bearings are glued to the end of the actuators which in turn are glued to the back of the mirror. A photograph of a completed adaptive mirror is given in figure (3.8).

The relationship between mirror position and the position of the star in the sky is given by

$$\theta_{\text{sky}} - \theta_{\text{average}} = \frac{2}{3} \times \theta_{\text{mirror}} \tag{3.12}$$

where θ_{sky} is the position of the star in one axis on the sky, θ_{average} is the average position of the star in that axis (including sidereal rate tracking) and θ_{mirror} is the position of the mirror. The factor of 2 arises because the reflected beam will be shifted by twice the angle of the mirror movement, while the factor of $\frac{1}{3}$ is due to the BRT. The vertical and horizontal axes of the mirrors will correspond with the altitude and azimuth axes of the siderostats only during transit. At other times they will rotate slowly with respect to these coordinates as the star moves across the sky. Since the tilt servo is used to supply star guidance information for the siderostats (refer to section 4.3) rotation matrices will be calculated by a separate programme to map the tilt servo axes to those of the siderostats.

If we assume that under bad seeing conditions the seeing disc of a star is 2", then by equation (3.12) these mirrors must have a range of at least 3". Since a seeing disc is a statistical measure of image motion, a larger range is really required. Furthermore, the tilt servo needs to cope with small guiding errors due to the siderostats. The mirrors used in this system use piezo-electric actuators to move mirrors with a range of approximately $\pm$10". This range has been found to be sufficient for use in SUSI. The frequency response bandwidth of the mirror movement is largely determined by the high-voltage amplifiers required to drive

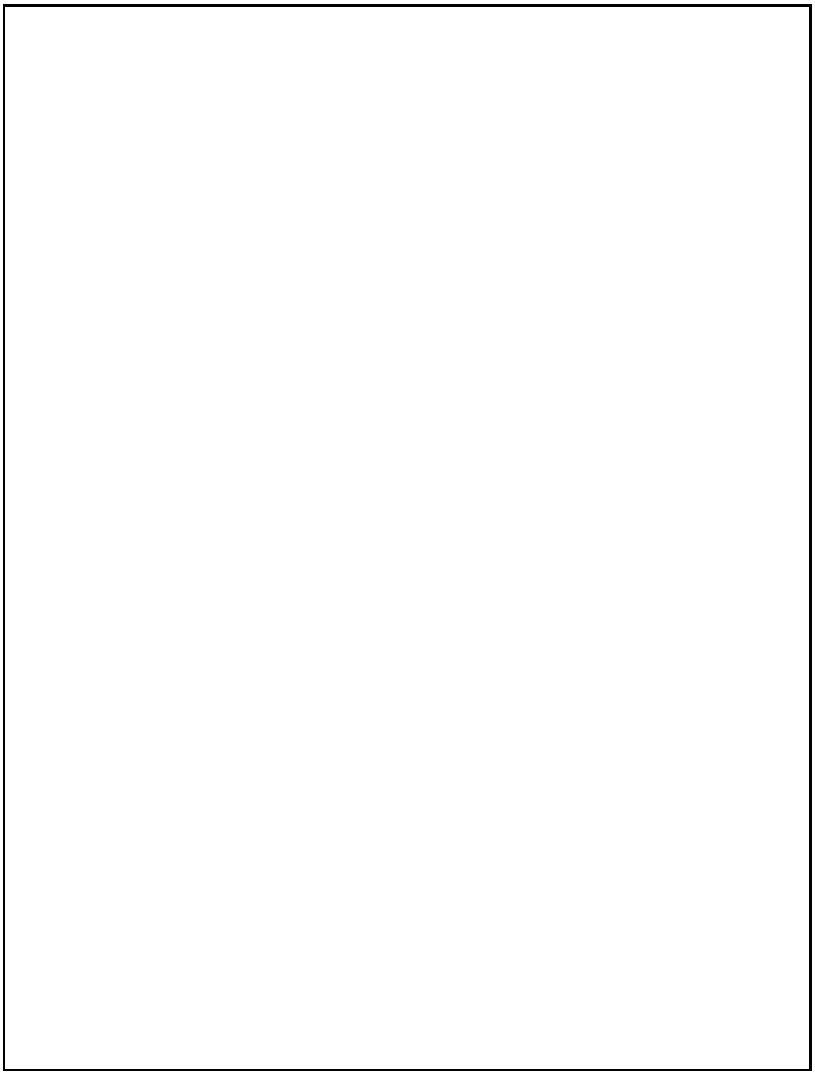

Figure 3.8: One of the adaptive mirrors with a protective cover removed. The three piezo-electric actuators can be seen behind the mirror flat. The whole assembly is mounted on three vertical adjustment screws.

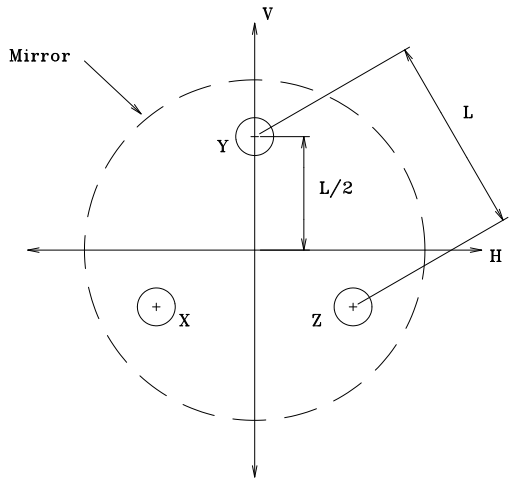

Figure 3.9: The axes used to define mirror response are defined in the diagram above. The position of the mirror can be represented as a vertical and horizontal tilt (V and H) or as the positions of the three actuators (X, Y and Z).

the piezo-electrics.

3.2.1 Response of Mirrors

Figure (3.9) contains a diagram of a tilt mirror and the three actuators whose change in length with respect to their average size are written X, Y and Z. The vertical and horizontal tilt axes are labelled V and H respectively. The actuators are laid out in an equilateral triangle with side length L such that all three points X, Y and Z are equidistant from the origin. In the current system $L \approx 40$mm. The equations relating the vertical and horizontal tilt with the positions of the three actuators are

$$\begin{aligned} V &= Y - \frac{X+Z}{2} \\ H &= \frac{Z-X}{\sqrt{3}} \\ 0 &= X+Y+Z \end{aligned} \tag{3.13}$$

which, solving for X, Y and Z gives

$$\begin{aligned} X &= -\frac{1}{3}V - \frac{\sqrt{3}}{2}H \\ Y &= \frac{2}{3}V \end{aligned}$$

$$Z = -\frac{1}{3}V + \frac{\sqrt{3}}{2}H. \tag{3.14}$$

These calculations, except for the multiplication by $\sqrt{3}$, are performed by the electronics using a simple operational amplifier circuit (see Appendix B), thus the response of the horizontal axis should be $\sqrt{3}$ different to that of the vertical axis, given the same input voltage. This difference in response is accounted for in the servo software. All that the servo electronics needs to supply is two voltages, one representing vertical tilt and one horizontal tilt.

3.2.2 Mirror Calibration

This adaptive optics system is a zero seeking servo and therefore the absolute calibration factors for the detectors and the mirrors need not accurately be known. However, to use mirror positions to study atmospheric turbulence the mirrors need to be calibrated. Using the mirrors to calibrate the detectors will also help in selecting appropriate servo parameters.

Since the angles involved are so small it was decided to use the interferometer itself for these measurements by sampling tilt fringes. Not only is this method very precise but it also means the mirrors are calibrated *in situ* using exactly the same electronics and optics as will be used during an astronomical observation.

Refer to figure (3.10) for a diagram of the optical layout of the calibration system for the tilt mirrors. The blue reference laser beam is passed through a spatial filter to the main beamsplitter on the optical table of the interferometer and subsequently the two output beams are autocollimated using a mirror placed in front of the BRT. Since the HeCd reference laser has a coherence length of only a fraction of a metre, the OPLC carriage was moved until high visibility tilt fringes could be seen on the CCD monitor which imaged the aperture plane. This optical layout is the equivalent of a standard Twyman-Green interferometer (Born and Wolf (1987) section 7.5.5). Tilt fringe images could then be sampled using the CCD and a frame grabber attached to a computer and stored for later processing. Although the video CCD used is not the perfect instrument for this kind of data collection it was found that it was very linear when used within its rather small dynamic range (Hrynevych (1992) Chapter 4). Furthermore, as the only part of the fringe pattern of interest here is fringe spatial frequency, any non-linear effects introduced by the camera should not be important.

The relationship between the spatial frequency of the tilt fringes ω_0 and

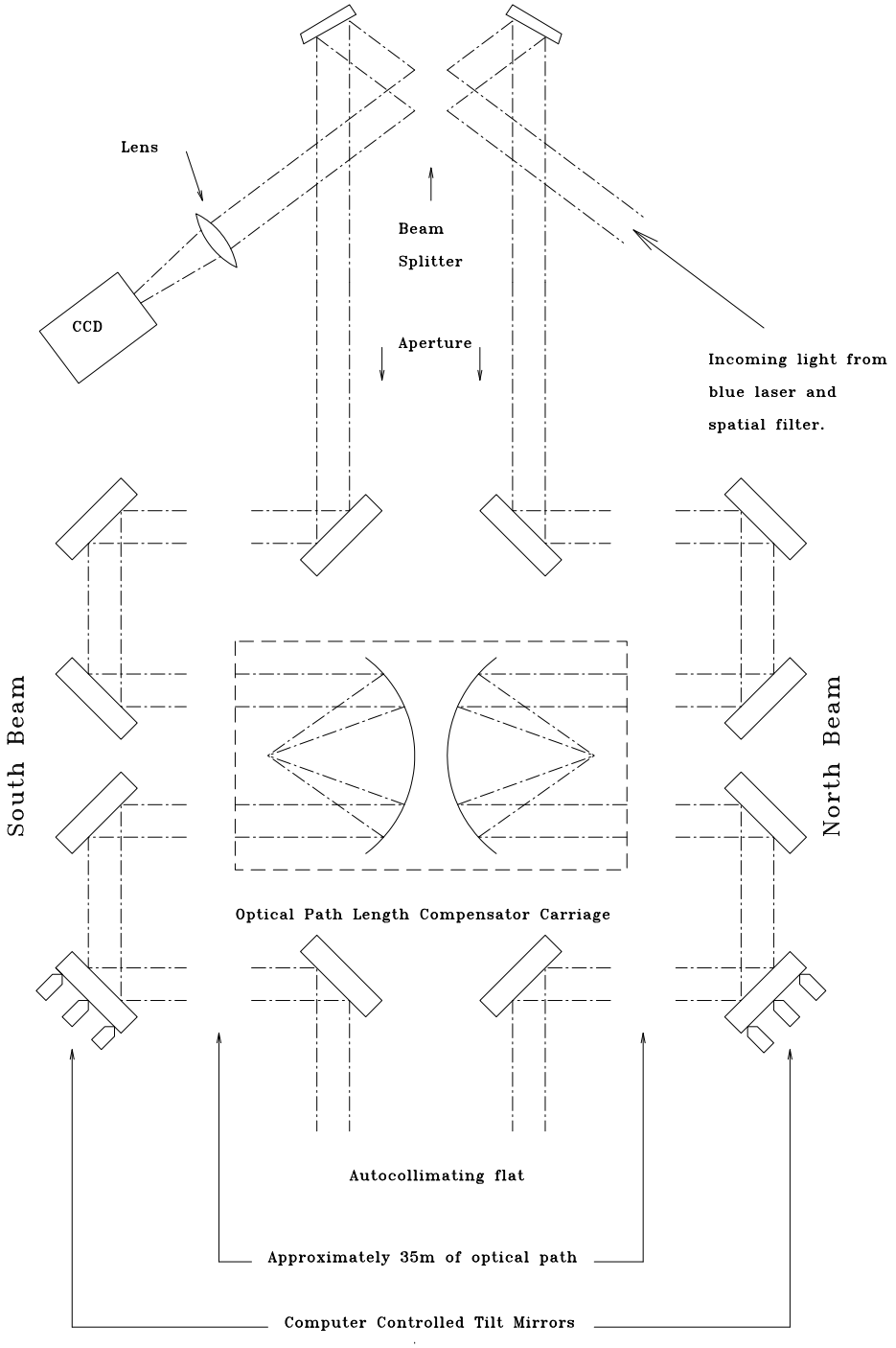

Figure 3.10: The optical layout used to calibrate the adaptive mirrors. The laser light, after passing through an optical spatial filter, enters the beamsplitter and then is sent down each arm of the interferometer. The autocollimating flat then reflects both beams back through the entire optical system to the beamsplitter where they are recombined and imaged onto the CCD array. The optical path length difference in the two arms was cancelled out by adjusting the optical path length compensator. In this way the system operates as a standard Twyman-Green interferometer and tilt fringes were observed.

the mirror position θ_{mirror} is

$$\theta_{\text{mirror}} = \frac{\lambda\omega_0}{4} \tag{3.15}$$

where λ is the laser wavelength (442nm). The resulting fringe pattern sampled by the CCD and frame grabber was modelled using the equation (Born and Wolf (1987) section 7.1)

$$I = I_1 + I_2 \cos^2(\pi\omega_0(x\cos\phi + y\sin\phi) + \delta). \tag{3.16}$$

The angle ϕ represents the rotation of the fringes, the intensities I_1 and I_2 are for the background light and fringe amplitude respectively and the δ term incorporates any fringe phase offset. Sampled data was fitted to equation (3.16) in the least squares sense. An example of sampled tilt fringes and the resulting fit can be found in figure (3.11).

To calibrate the CCD, a series of flat fields were sampled with the same optical setup for each beam. The resulting images were diffraction patterns caused by the aperture. The number of CCD pixels per millimetre in the aperture plane and the location of the centre of the aperture were found using the fact that the intensity of light is at one quarter of the average intensity across the aperture at the diffracting edge (Born and Wolf (1987) section 8.7.3). These data, combined with the known aperture size of 35mm, were sufficient to calibrate the CCD images.

The measurements of mirror position were also affected by the air mass inside the interferometer enclosure. This was minimised by allowing the enclosure to settle for a number of hours before any measurements were made and averaging over a number of readings. As would be expected, this internal 'seeing' affected the measurements of the smallest angles most severely. For this reason each run on a mirror axis was set up so that the mirror range had zero tilt at one end of the run rather than in the centre, halving the number of small angles in the measurements.

Two separate experiments were performed for each axis of each of the two mirrors. Both covered the entire range of the digital to analogue converters in the electronics which supplied the control voltages for the piezo drives. Results of both experiments are shown for one mirror axis in figure (3.12). In one run, referred to as the static run, the mirrors were set to a given voltage, allowed to settle and a measurement was taken with the mirror at rest. This experiment confirmed that the positioning of the mirrors was linear. The second experiment tested the dynamic response of the mirrors. Each axis in turn was driven by a 1Hz sine wave with samples being taken at various phase positions. The results

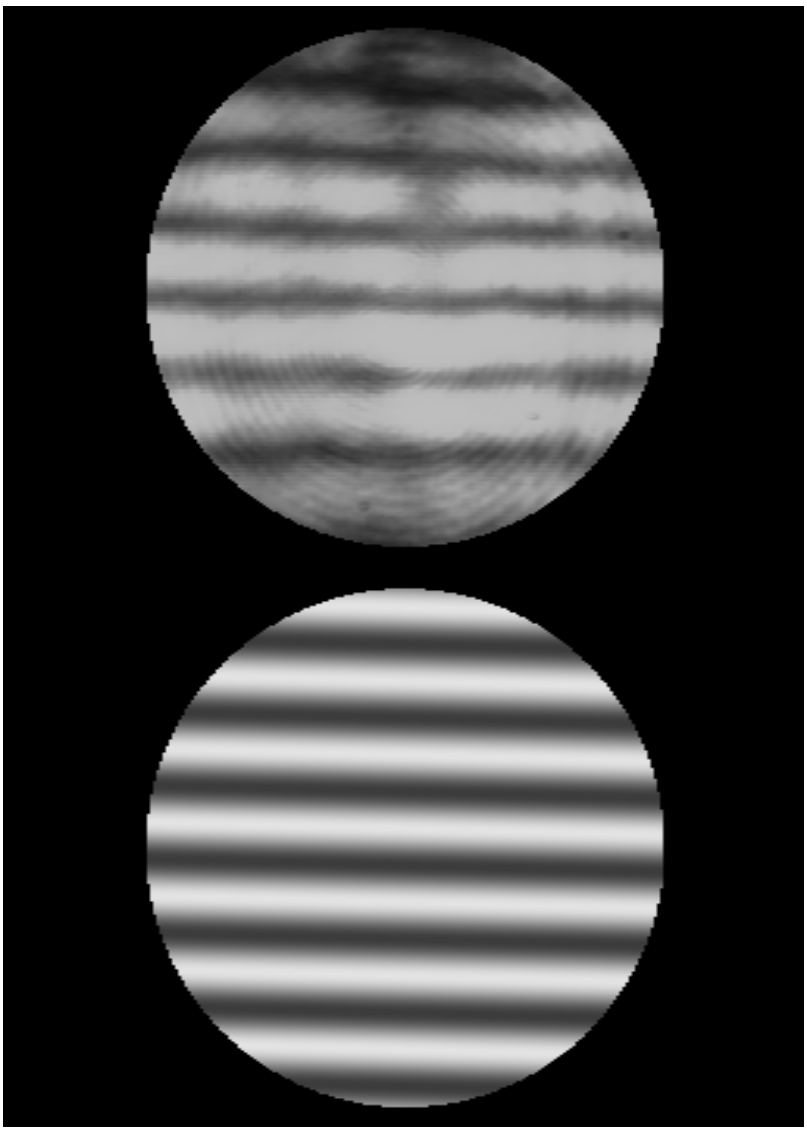

Figure 3.11: An example set of sampled tilt fringes (top) and the resulting fit (bottom). The circular ring pattern in the sampled data is the result of diffraction and is not modelled. The spatial frequency of these fringes is a measure of mirror tilt and can be read straight out of the fitted data.

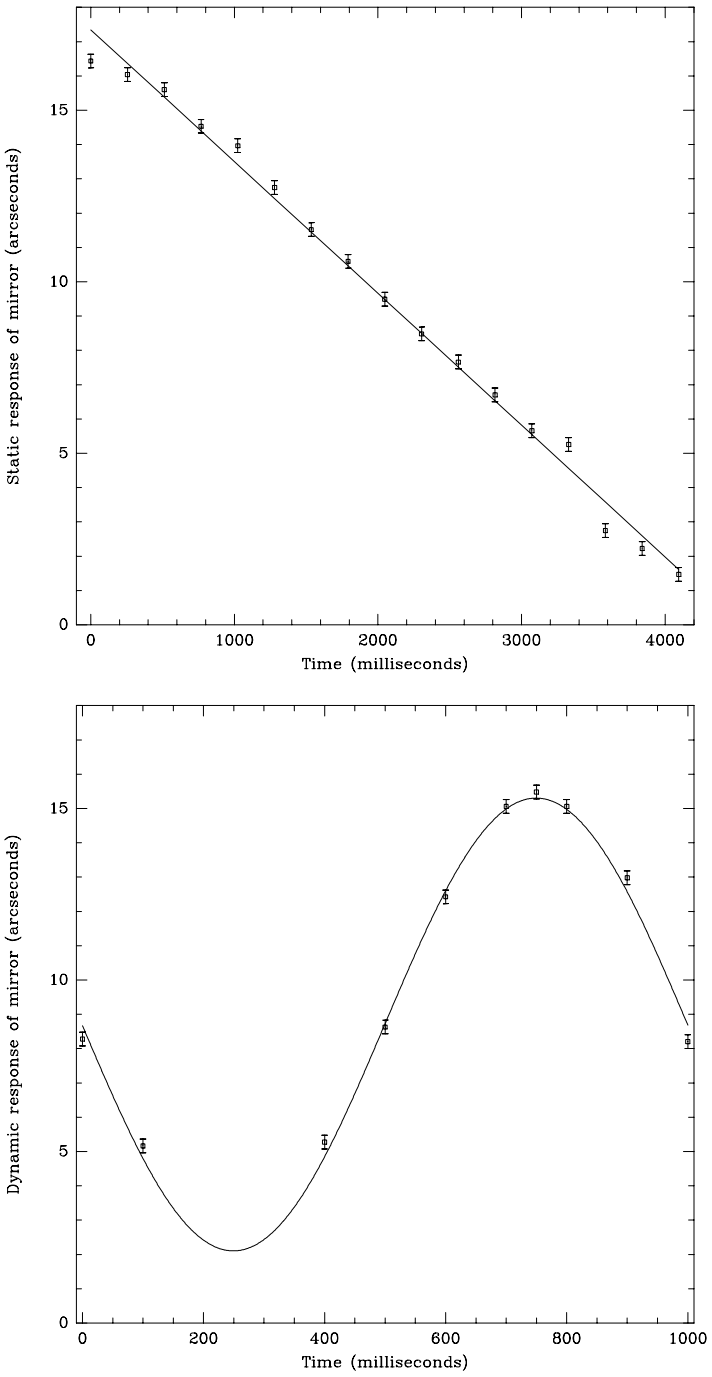

Figure 3.12: The response of one axis of one of the tilt mirrors for the static case (top) and the dynamic case (bottom). Both plots cover the entire range of movement of the mirror. The solid line in the lower graph represents the 1Hz signal used to drive the mirror. Some small angle positions are missing from this plot as the results of these measurements were badly affected by turbulence inside the instrument enclosure. A fit to these two plots results in a calibration constant of -3.84 ± 0.08 milliarcseconds per DAC unit for the static case and -3.2 ± 0.1 milliarcseconds per DAC unit for the dynamic case. The dynamic result has been used throughout the rest of the calculations.

Axis	K_m
North Vertical	9.06 ± 0.27
North Horizontal	9.39 ± 0.27
South Vertical	9.66 ± 0.30
South Horizontal	9.33 ± 0.33
Average	9.36 ± 0.30

Table 3.3: The final calibration constants used for the adaptive mirrors are tabulated above. Given the 'normalised' mirror position, that is $+1$ represents maximum and -1 the minimum, the angular position of the beam can be found by multiplying by the appropriate calibration constant. To obtain the equivalent angular position on the sky these constants need to be divided by 3 to account for the effect of the BRT.

showed that the dynamic response of the mirrors was slightly smaller than the static response. This is to be expected given the mass of the mirror being moved and the imperfections in the response of the high voltage amplifiers driving the piezos. The amplifiers were being driven at close to maximum output and thus with a sine wave input the $\frac{dV}{dt}$ at the output could be expected to be very large (Refer to section (3.3.2) for a discussion of the performance of these amplifiers). It was decided to use the dynamic calibration for all further work as it most closely simulates mirror operation when tracking seeing. The final calibration constants for the mirrors are given in table (3.3). Based on this set of calibration data it is possible to measure image position on the sky to within ± 0.1".

3.3 Electronics

While a great deal of electronics are required for the adaptive optics system to function, most of the circuitry uses standard techniques and will not be discussed in detail here. A block diagram showing the major parts of the servo electronics is given in figure (3.13) and the corresponding circuit diagrams can be found in Appendix B. The two areas that will be discussed below are the photon counting circuitry and the high voltage amplifiers used for the piezo-electrics, as both have a significant effect on the performance of the tilt servo.

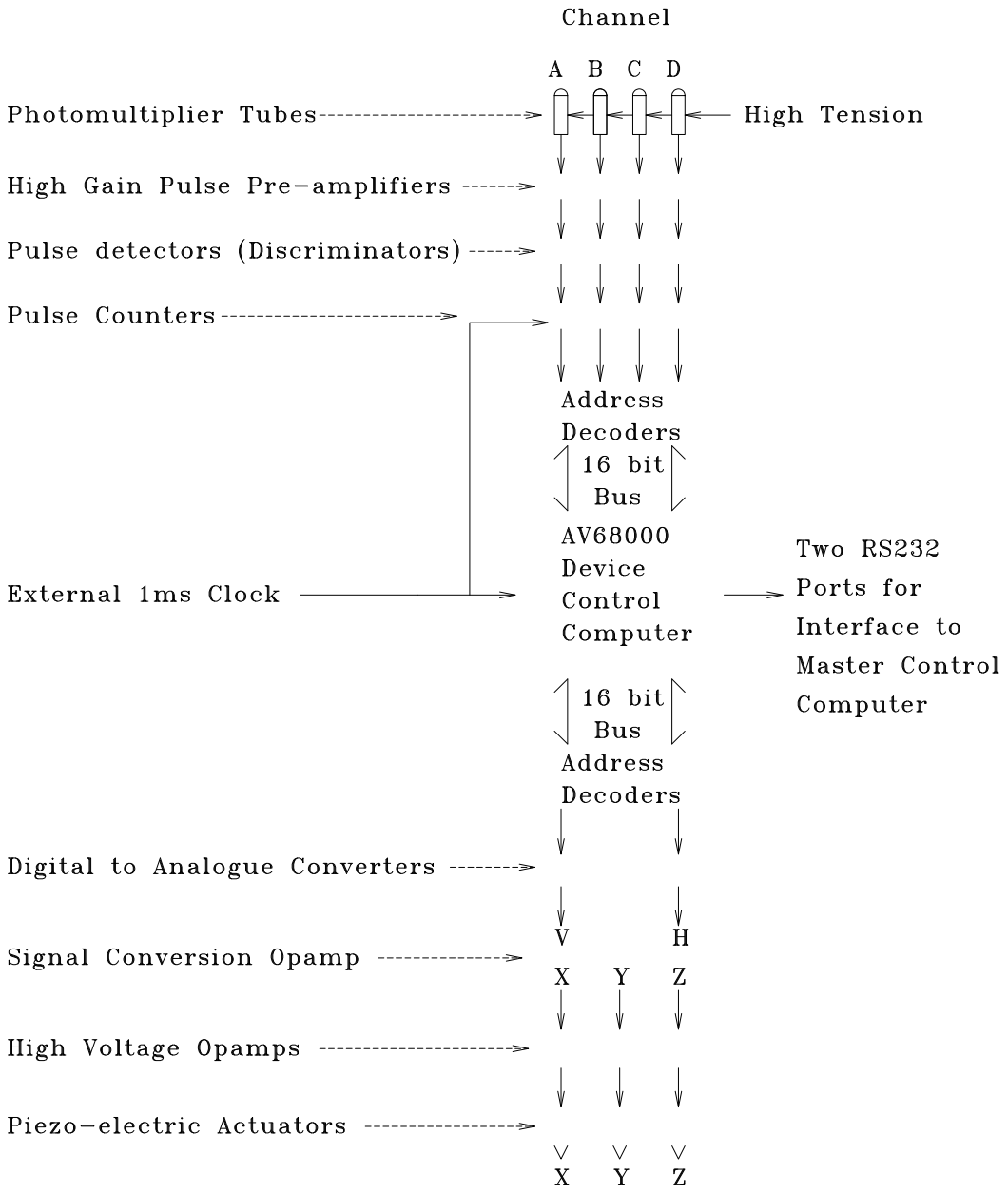

Figure 3.13: A block diagram of the electronics for the tilt servo system. Note that only one set of detector and mirror electronics are shown. The actual system contains three detector sets (north, south and reference) and two mirror sets (north and south). Some units are discussed in more detail in the text. The circuit diagrams can be found in Appendix B.

3.3.1 Photon Counting Circuitry

The servo contains three separate quadrant detectors, each using four photon detection systems. These systems have three main parts; a pre-amplifier, a pulse detection circuit and a counting circuit. The counting circuitry is standard TTL logic design and will not be discussed here.

Behind each quadrant detector there is a single water cooled unit containing four matched photomultipliers, four pre-amps and four pulse detection circuits with external power supply connections. The photomultipliers used were E.M.I. 51mm diameter bialkali tubes type 9789A with maximum sensitivity in the blue ($\sim$ 440 nm). These tubes were matched for gain by the manufacturer. Resistor divider chains were used in the high tension supply and the resistor values chosen so each tube operates nominally at the same gain. Each photomultiplier was then placed in the container behind a glass window which faces the output of an optical pyramid. The pre-amplifier and pulse detectors were then mounted inside the box immediately behind the photomultipliers, thereby keeping to a minimum the length of cables used to transmit the low level, high frequency signals. Water cooling was also used to reduce any problems with extra turbulence caused by heat generated by the detectors.

Many commercial pre-amplifier/pulse detection systems exist, however, due to the size and high cost of these systems, it was decided to develop circuitry to perform this task within the department. The pulse detection circuit used is a simple discriminator based upon the LM360 chip. While this is a simple circuit, it was found the orientation and separation of the components affected the performance of the device. A printed circuit board was designed to fit all four circuits into the container and maximise performance by placing all components as close together as possible while keeping to a minimum those that are adjacent and parallel. Any unused part of the board is used as an earth plane. Building a pre-amplifier that performed suitably proved to be more difficult. A number of designs were tested, some based upon discrete transistor circuits (Taylor, 1980) and others on specialised chips (Palmer (1988) and DuPuy (1981)), few of which performed well at all. A circuit based upon a high speed operational amplifier (Radio Shack, 1988) was eventually chosen as the components were commonly available, as well as an 'off the shelf' printed circuit board. This pre-amplifier also had the best performance of all those tested. The pre-amplifiers were built, tested and grouped in sets of four so that their characteristics were roughly matched. Figure (3.14) shows a circuit diagram of one such pre-amplifier/discriminator circuit.

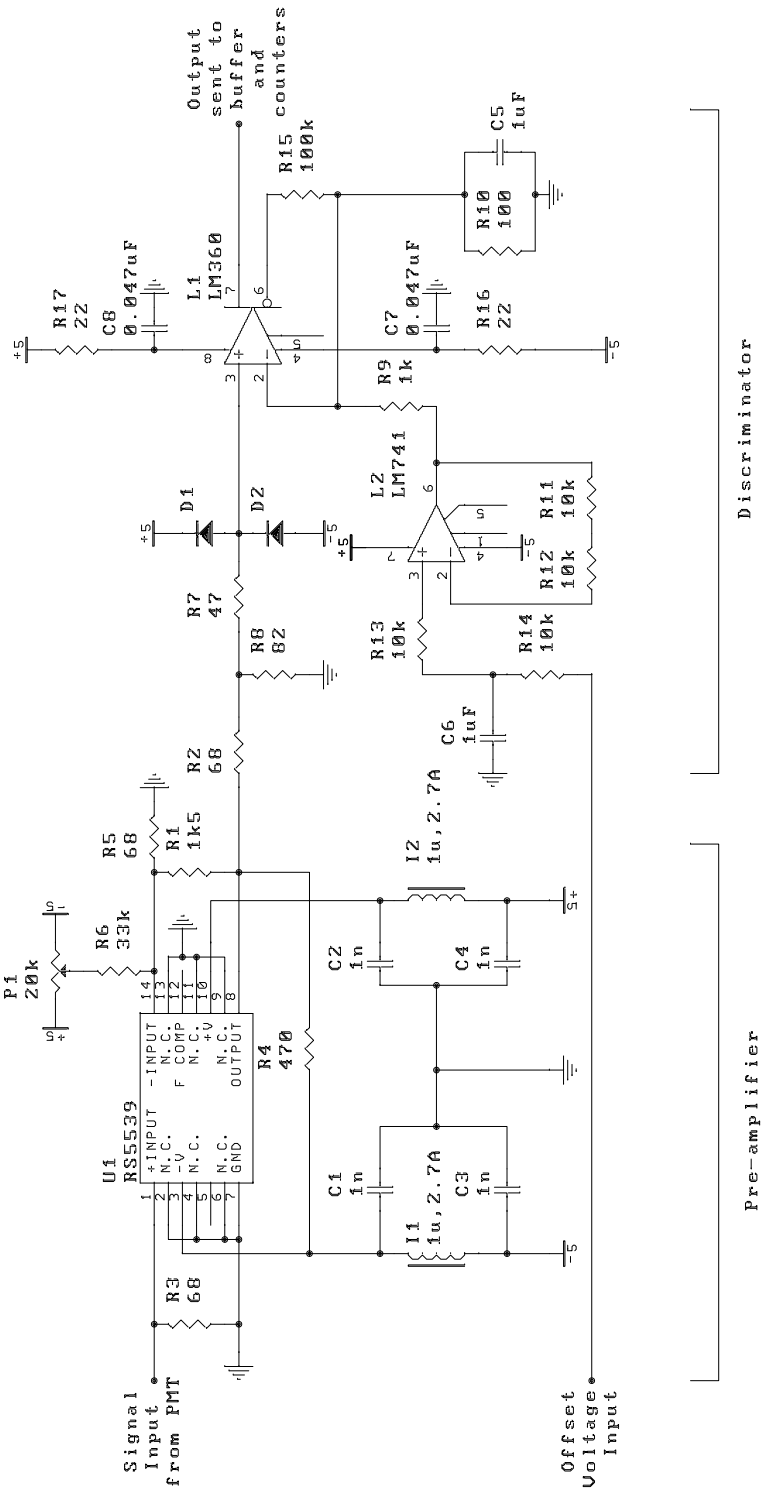

Figure 3.14: Circuit diagram for one preamplifier/discriminator circuit. The preamplifier circuit was based on a commercially available device (Radio Shack, 1988), while the discriminator was a modification of a circuit by Palmer (1988).

Once these photomultiplier/pulse detection boxes were completed an experiment was performed to check the system's linearity and that the number of counts received was correct. A small light emitting diode (LED) was used as a light source with an adjustable supply current. This current was set so that the photomultiplier under test was producing the recommended maximum current of 10μA. Neutral density filters were then inserted between the LED and the photomultiplier so the anode current and number of pulses per millisecond could be measured at different light levels. The number of pulses expected for a given anode current is given by

$$N_{\text{pulses}} \approx \frac{I_a \times T}{q_e \times G} \tag{3.17}$$

where I_a is the anode current, T is the sample time (in this case 1ms), q_e is the charge of an electron and G is the gain of the photomultiplier (in this case, 10^7). Figure (3.15) shows the results of these tests for one of the photomultipliers and clearly demonstrates that the expected number of counts was achieved and that the system is linear. Other calculations performed by Dr. W. Tango[4] when the photomultipliers were originally used in the prototype interferometer give the expected quantum efficiency of the optical system. The results are plotted in figure (3.16). From this graph it is clear that the median and weighted mean wavelength is approximately 440nm. This wavelength will be used in all further calculations as a representative wavelength of the system.

After these tests it was noticed that the response of the four quadrants was not the same for all of the photon counting systems. If these differences in response are constant with changing input intensity, they can be corrected by using simple weighting factors in the servo software. To see if this effect was consistent one of the servos was turned on and locked onto the laser beam using the same optical set up as described in Appendix A. The amount of light reaching the detectors was varied by introducing different amounts of neutral density to the incoming beam. The number of counts reaching channels B, C, and D compared with those reaching channel A were recorded and are shown in table (3.4). The ratios of counts received remained essentially constant over the range of light intensities tested indicating that this effect can easily be corrected. In future, this should be fixed in the electronics, however, as the effect is constant, suitable weighting factors have been added in the software such that

$$\mathcal{N}_{A,\ldots,D} = W_{A,\ldots,D} \times N_{A,\ldots,D}, \tag{3.18}$$

where $N_{A,\ldots,D}$ are the raw counts, $W_{A,\ldots,D}$ are the weighting factors and $\mathcal{N}_{A,\ldots,D}$ are the resulting weighted values used by the rest of the servo software. Refer to

[4]Unpublished internal report.

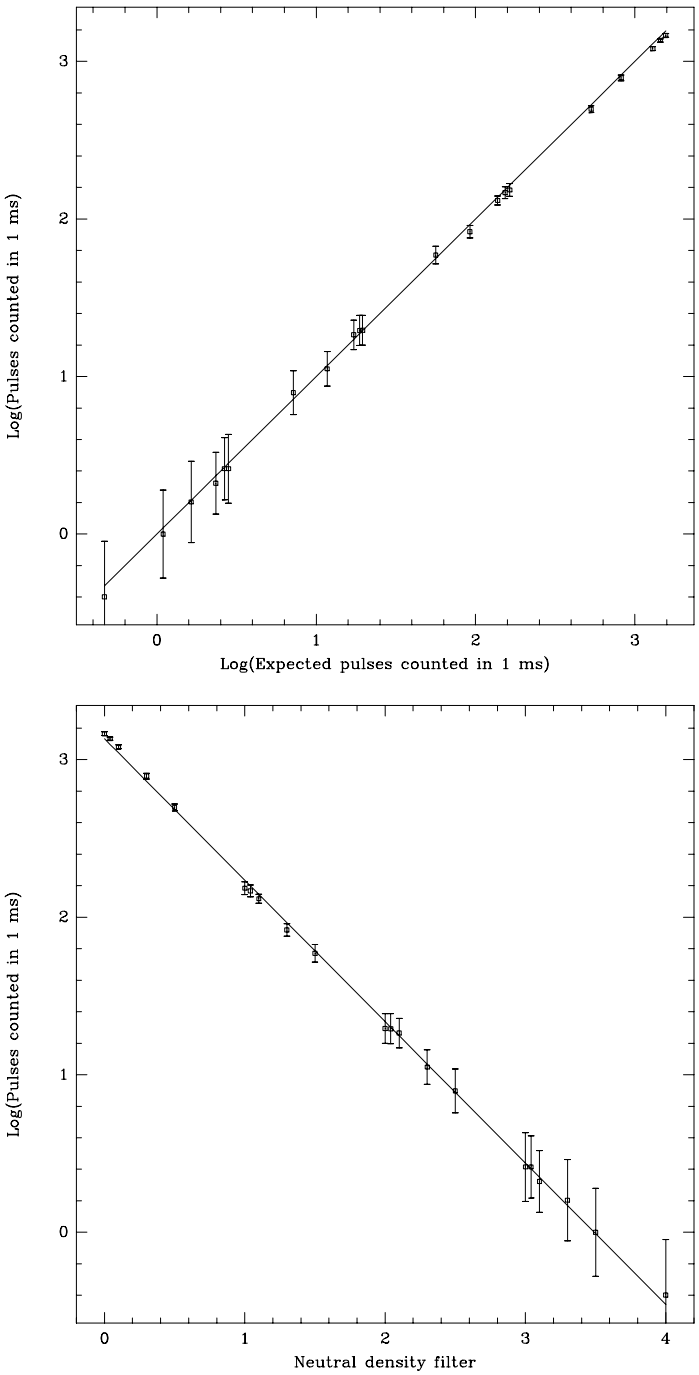

Figure 3.15: These two plots show the results of a test run on one of the photomultiplier/pulse detection circuits used in the servo system. The test consisted of using a faint light source and measuring anode current and pulse rates with a number of different neutral density filters in between the light source and the photomultiplier. The plot at the top shows measured pulse rates against pulse rates predicted using equation (3.17) and clearly demonstrates that the electronics achieve the desired sensitivity. Due to dead time in the counter circuits (1μs) the measured rate drops below the predicted value at high count rates. The lower plot shows measured pulse rates against the neutral density filter used, showing the system is linear.

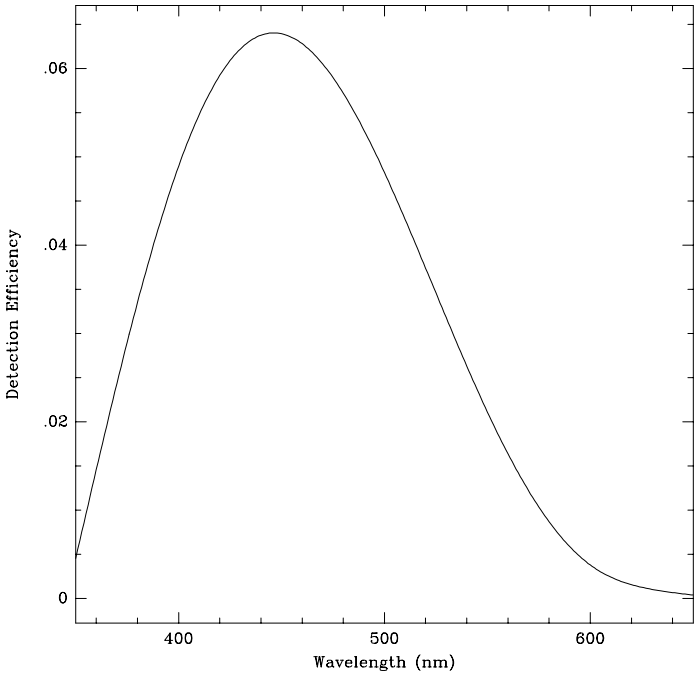

Figure 3.16: The data displayed above shows the expected quantum efficiency of the optics and photomultiplier tube combination. Note that the maximum sensitivity is near 440 nm and is of the order of 0.06.

ND	N_A	$\frac{N_A}{N_B}$	$\frac{N_A}{N_C}$	$\frac{N_A}{N_D}$
4.3	2877	0.629	1.01	0.630
4.4	2889	0.664	1.00	0.670
5.0	1485	0.637	1.04	0.632
5.1	1026	0.589	0.98	0.595
5.3	450	0.649	1.02	0.669
5.4	378	0.602	1.00	0.619
6.0	155	0.651	0.98	0.638
6.1	94	0.644	1.03	0.618
6.3	66	0.647	1.03	0.673
6.4	16	0.615	1.00	0.615
Mean	N.A.	0.63±0.02	1.01±0.02	0.64±0.03

Table 3.4: Count rates of the four channels of one of the photon counting sets for varying light intensity. The column at the left shows the neutral density filter used for each run. It is clear that the ratio of counts received remains constant with changing intensity.

Appendix (C) for a description of the procedure used to measure and set these weighting factors.

A final test of the photon counting system was performed after the system had been installed in the interferometer to check count rates received from a number of stars of known magnitude. The amount of energy radiated from a star reaching the outside of earth's atmosphere in the blue is given by (Allen (1973) section 94)

$$m_B = -2.5 \log \left(\int B_\lambda f_\lambda d\lambda \right) - 12.97 \tag{3.19}$$

where m_B is the blue magnitude and $\int B_\lambda f_\lambda d\lambda$ is in erg cm^{-2} s^{-1}. As a rough approximation, we assume we can model the blue light as a number of photons of average wavelength 440nm, that is, if $N_{\rm ph}$ is the number of photons arriving, A is the aperture area in cm^2 and T is the sample period and $\lambda_{\rm av}$ is the average wavelength then

$$\int B_\lambda f_\lambda d\lambda \approx N_{\rm ph} \frac{1}{AT} \frac{hc}{\lambda_{\rm av}}. \tag{3.20}$$

By combining equation (3.19) and equation (3.20) we obtain

$$N_{\rm ph} = \frac{\eta_T}{2} \frac{\lambda_{\rm av}}{hc} AT \times 10^{(\frac{m_B + 12.97}{-2.5} - 7)} \tag{3.21}$$

where η_T is the quantum efficiency of the total system incorporating losses due to the atmosphere η_A, interferometer and quadrant detector losses η_I and the quantum efficiency of the photon counting system itself η_P such that

$$\eta_T = \eta_A \eta_I \eta_P. \tag{3.22}$$

The factor of two in equation (3.21) is present because only half the light reaching the optical table is directed towards the detector system. A number of stars of varying magnitudes were observed and tracked with the tilt correction servo and the count rates logged. A sample of the data collected is given in table (3.5). The results showed the total quantum efficiency of the northern system to be 0.0051 ± 0.0007 and that of the southern to be 0.0067 ± 0.0007. These results are an order of magnitude below the quantum efficiencies predicted and displayed in figure (3.16). Count rates in the visibility measurement system have also been found to be much less than predicted, indicating that the problem probably lies in some part of the optics other than the optical table. One of the factors contributing to this low efficiency is the rather poor surface quality of the adaptive mirrors. These mirrors were originally constructed for the prototype interferometer and the coatings have degraded visibly. Another factor would be the atmosphere, which can cause losses of up to the equivalent of a magnitude

Star	m_B	η_T	Spectral Type
α Eri	0.30	0.005	Bs Vp
α Pav	1.24	0.005	B2.5 V
α Psa	1.25	0.008	A3 V
α Dor	3.17	0.004	A0 IIIp Si
θ Eri	3.54	0.005	A5 III
δ Cap	4.00	0.008	Am
π Phe	6.26	0.019	K0 III
ι Tuc	6.25	0.019	G5 III

Table 3.5: A sample of the data used to estimate the total quantum efficiency of the south arm of the tilt correction servo photon counting system. The seeing during the observational run did not allow fainter objects. The magnitudes are taken from the Bright Star Catalogue (Horrit and Jaschek, 1982) and the quantum efficiencies were calculated using equation (3.21). The two largest values of 0.019 in the table apply to stars of spectral types K and G while the rest of the stars in the table are class A or B. Using m_B to calculate the efficiency does not take into account the different spectral shapes of these stars. The photomultiplier sensitivity is centred at 450nm with a bandwidth of 200nm. It is to be expected that the count rates are higher for G and K class stars, as their spectra contain more energy in this waveband than the A or B class stars.

of intensity. The coating stability of the siderostat mirrors and other internal optical surfaces may also contribute to this low figure.

We are now in a position to estimate the limiting magnitude of the system. A night with very good seeing allows the use of the largest aperture size of 12cm and a sample time of 50ms. In order to track the star and meet the specifications set out in section (1.4) the detector error must be less than 0.1". By equation (3.11) we therefore require at least 40 counts per sample. It has also been found experimentally that counts below this figure result in unstable servo behaviour. By equation (3.21) the system could in theory go to a magnitude of 7.0 before failing. This is in agreement with earlier estimates (Davis and Tango (b) (1985) and Tango (1979)). If the reason for the low light levels measured could be found and quantum efficiencies closer to those predicted achieved, the limiting magnitude would become 8.5.

3.3.2 High Voltage Amplifiers for Piezos

The maximum frequency response of the tilt servo as a whole can be no greater than that of the tilt mirrors themselves. Large voltages are required to drive the piezo-actuators and the piezos can be considered as a capacitive load of approximately 20nF. This means the amplifiers will start to fail at high frequencies when the high amplitude voltage shifts over small time periods imply large currents. Furthermore, several strong resonances occurred in the piezos and the physical system which needed to be repressed in the high voltage amplifiers. In order to test the amplifier performance a sine-wave generator was connected to the input of one of the high voltage amplifiers and the output voltage measured with the piezo connected to and loading the amplifier. Measurements were taken at a number of frequencies and amplitudes in order to determine the frequency response of the amplifier/piezo combination. The results are shown in figure (3.17), which shows a -3dB frequency of 160 ± 10 Hz. This frequency response is sufficient to cover the power spectrum of any Zernike coefficient as defined in equation (2.71) and, as will be shown in section (4.2.4), largely determines the maximum bandwidth of the tilt servo as a whole. These measurements also showed the amplifier/mirror combination to suffer from hysteresis. Modern piezo control electronics now available are capable of reducing the effects of hysteresis and should in future be incorporated into the system. The effects of hysteresis are further discussed in section (4.2.3).

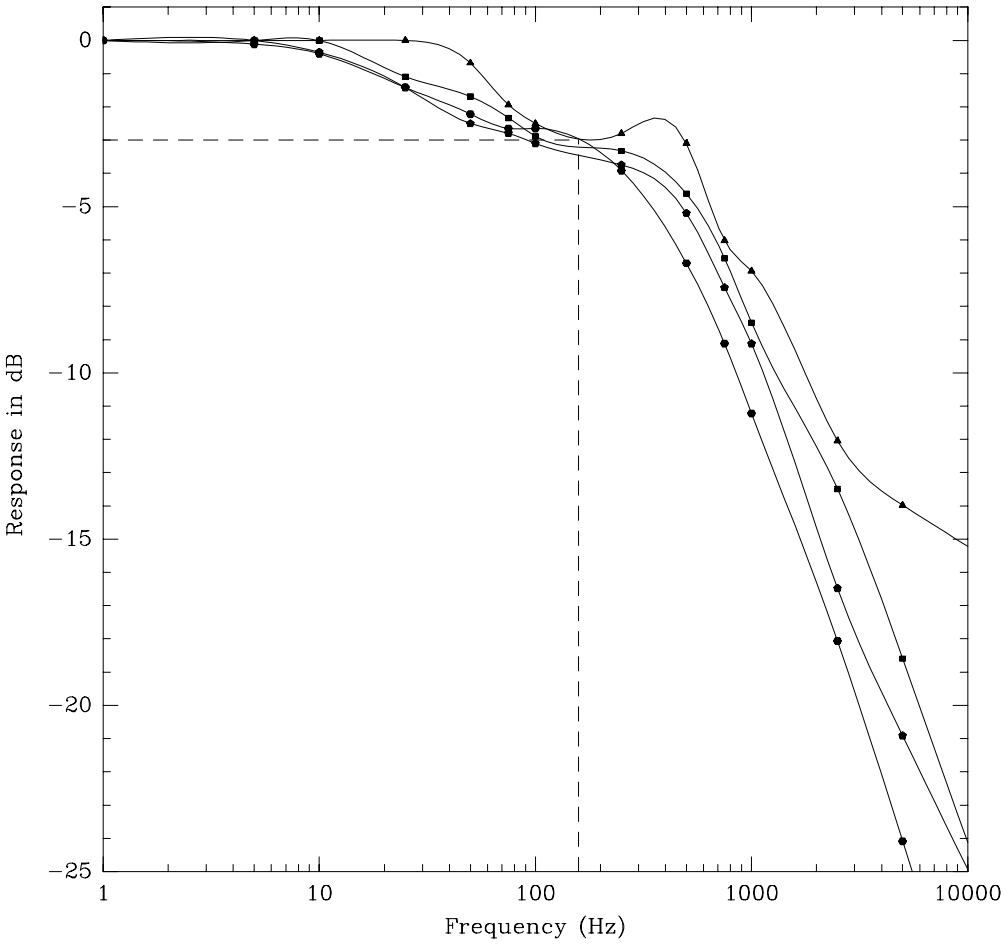

Figure 3.17: Frequency response of the high voltage amplifiers used to drive the piezo-electric actuators on the tilt mirrors. Each set of points represents different output voltage amplitudes: triangles 20 volts, squares 40 volts, pentagons 200 volts and hexagons 400 volts. The solid lines are spline fits to each data set while the dashed line shows the position of the -3dB position of 160 ± 10 Hz.

Chapter 4

SERVO AND PERFORMANCE ANALYSIS

Since the tilt correction system can be described as a zero seeking servo, its behaviour is subject to linear control theory. Before the data gathered by the system can be used, the reliability and the functional properties of the system need to be known and understood. Furthermore, in order to adjust the feedback parameters of the digital servo, a mathematical model of the system's performance must be developed. Such a linear model is described in this Chapter.

Before developing this model basic linear control theory will be outlined in the first section, covering *Laplace transforms*, *Transfer functions*, *Z transforms* and *Negative feedback*. The reader is assumed to be familiar with Fourier transform analysis techniques, which will be used as a reference point for the discussion of Laplace transforms.

In the second section this theory will be used to generate a linear model for the tilt correction servo. Each component will be discussed separately and then these individual models will be put together to form a model of the entire system. This model will be used to find optimal feedback parameters for the operation of the tilt correction servos.

Apart from beam stabilisation the tilt correction servo is also responsible for providing a star guidance error signal for the siderostats in the form of an average tilt mirror position. The tilt corrector/siderostat servo will be briefly discussed in the third section.

With the optimised parameters in place the final section contains a performance analysis of the system while tracking a star.

4.1 Linear Control Theory

If the behaviour of a system can be described by a linear differential equation it can be analysed using linear control theory. This technique involves constructing the transfer function of the system which allows its analysis in much the same way as an optical transfer function aids in the analysis of an optical system. These techniques are described in numerous texts, for example, those used by the author: Barbe (1963) and Dorf (1974). The book by Tyson (1991) also contains a summary of linear control theory as applied to adaptive optics. Most of these books concentrate on analogue models using a method related to Fourier transform theory called Laplace transform theory. Laplace transforms map a linear differential equation to a linear algebraic expression thereby greatly simplifying systems analysis. To analyse a digital system the equivalent sampled transform, known as the $\mathcal{Z}$ transform, is required. More recent texts such as Franklin and Powell (1980) cover the theory and uses of these methods. Laplace transform methods and the $\mathcal{Z}$ transform are also included in the book by Bracewell (1986).

The frequency-domain techniques to be outlined below are limited in their usefulness to linear, time-invariant systems. The advantage of this approach is its direct link to Fourier analysis and the ease of interpretation of the results. For nonlinear, time-varying or multivariable systems a time-domain formulation is more appropriate. This method is known as *state variable analysis* and is described in the references cited above. The tilt correction servo is linear and so state variable analysis has not been used. Furthermore, a treatment in the frequency domain better compliments the power spectrum analysis of Chapter 2 and the frequency response measurements presented in section (4.2.4).

4.1.1 Laplace Transforms

The Laplace transform maps a function in the time domain $f(t)$ to a complex function $F(s) = \mathcal{L}(f(t))$ where s is a complex variable. The *one sided* Laplace transform of $f(t)$ is defined

$$F(s) = \mathcal{L}(f(t)) = \int_0^\infty f(t)e^{-st}\,dt. \tag{4.1}$$

A transform of a function exists if the integral

$$\int_0^\infty |f(t)|e^{-\sigma_1 t}\,dt \tag{4.2}$$

Description	$f(t)$	$F(s) = \mathcal{L}(f(t))$
Constant	1	$\frac{1}{s}$
Heavyside's unit function	$v(t)$	$\frac{1}{s}$
Proportional	t	$\frac{1}{s^2}$
Delta function	$\delta(t)$	1
Exponential	e^{at}	$\frac{1}{s-z}$
Trigonometric functions	$\frac{\sin(at)}{a}$	$\frac{1}{s^2+a^2}$
	$cos(at)$	$\frac{s}{s^2+a^2}$

Table 4.1: A sample of function/Laplace transform pairs. Standard tables of such functional pairs can be found in many mathematical handbooks such as Beyer et al. (1979) and linear control theory texts such as Dorf (1974).

converges for some real, positive value of σ_1. In almost all cases of physical systems this integral will converge. The inverse Laplace transform is

$$f(t) = \frac{1}{2\pi i} \int_{\sigma - i\infty}^{\sigma + i\infty} F(s) e^{st}\, ds \tag{4.3}$$

where σ is a suitable real constant chosen such that $\sigma < \sigma_1$. An important property of these transforms is their relationship to the Fourier transform. If the variable s is replaced with $i\omega$ where $\omega = 2\pi f$, the Laplace transform defined in equation (4.1) becomes

$$F(i\omega) = \int_0^\infty f(t) e^{-i\omega ft}\, dt = \int_0^\infty f(t) e^{-2\pi it}\, dt \tag{4.4}$$

which, by comparison to equation (2.61), is the same as the Fourier transform of $f(t)$ provided $f(t) = 0$ for $t < 0$. Hence, once we have the Laplace transform of a function the Fourier transform can be found by simply replacing the variable s with $i\omega$. This allows us to use theorems from Fourier transform theory. A few examples of function and Laplace transform pairs are given in table (4.1). More complete tables of this kind can be found in the references listed above or in almost any mathematical handbook, such as Spiegel (1968) or Beyer et al. (1979).

A number of general properties exist for Laplace transforms that make the solution and analysis of linear differential equations quite simple. For example, consider the transform of the first derivative of the function $f(t)$:

$$\mathcal{L}(f'(t)) \;=\; \int \frac{df(t)}{dt} e^{-st}\, dt$$

Description	$f(t)$	$F(s)$
Similarity	$f(at)$	$\frac{1}{\|a\|}F(\frac{s}{a})$
Addition	$f_1(t) + f_2(t)$	$F_1(s) + F_2(s)$
Shift	$f(t-a)$	$e^{-sa}F(s)$
Differentiation	$f'(t)$	$sF(s)$
Integration	$\int_0^t f(t)dt$	$\frac{1}{s}F(s)$
Reversal	$f(-t)$	$F(-s)$

Table 4.2: Some general properties of Laplace transforms. Many other properties exist and are listed in the references cited in the text.

$$\begin{aligned} &= \int e^{-st}\, d(f(t)) \\ &= \int f(t)\, d(e^{-st}) - f(0) \\ &= s\int f(t)e^{-st}\, dt - f(0) \\ &= s\,\mathcal{L}(f(t)) \end{aligned} \tag{4.5}$$

provided that $f(0) = 0$. The differential operator $\frac{d}{dt}$, then, maps to a multiplication by s, so that linear differential equations are mapped to linear algebraic expressions. Many other useful properties of the Laplace transform exist, some of which are listed in table (4.2). More complete lists of general properties can be found in the texts cited above. Using a combination of these properties and the function/Laplace transform pairs the analysis of linear differential equations and the physical systems they represent reduce to the solution of a set of linear algebraic equations.

4.1.2 Transfer Functions

If the input to a linear system is $i(t)$, whose Laplace transform is $I(s)$, and the output of the system is $o(t)$, with the transform $O(s)$, the transfer function of the system is defined as

$$T(s) = \frac{O(s)}{I(s)} \tag{4.6}$$

with all initial conditions set to zero. The transfer function of the system describes its dynamics but contains no information concerning its internal function. In order for a transfer function to exist the system must be *stationary*, that is,

all parameters describing the system must be constant since, if the system parameters vary with time, the Laplace transform cannot be used. The transfer function of a system allows us to find the output of a system for any given input by finding the Laplace transform of the input, multiplying by the transfer function and performing an inverse transform on the result. For example, consider a low pass filter described by the differential equation

$$o(t) = i(t) - \tau \frac{do(t)}{dt} \tag{4.7}$$

where τ is the time constant of the filter. These systems are also known as damped or simple lag systems. Applying the Laplace transform to this equation gives us

$$O(s) = I(s) - \tau s O(s). \tag{4.8}$$

The transfer function of the filter is then

$$T_{\text{lp}}(s) \equiv \frac{O(s)}{I(s)} = \frac{1}{1 + \tau s}. \tag{4.9}$$

Once the transfer function of the system has been found it is relatively easy to calculate its complex gain by means of impulse response analysis. If the input to a system is an impulse, that is $i(t) = \delta(t)$, whose Laplace transform is $I(s) = 1$, the Laplace transform of the output $O(s)$ will be identical to the transfer function $T(s)$. Fourier transform theory tells us that the complex gain of a linear system is given by the Fourier transform of the output when the input is a delta function (Bracewell, 1986). By equation (4.4) this can be obtained by substituting $i\omega$ for s in the transfer function. If we know the transfer function of a system we then know that the gain of the system in decibels is

$$\text{Gain}(\omega) = 20 \times \log |T(i\omega)| \text{dB} \tag{4.10}$$

and the phase shift imposed by the system will be

$$\text{Phase}(\omega) = \tan^{-1} \frac{\text{Im}(T(i\omega))}{\text{Re}(T(i\omega))} \tag{4.11}$$

where $\omega = 2\pi f$. For example, in the case of the low pass filter, the gain in decibels will be

$$\text{Gain}_{\text{lp}}(\omega) = -10 \times \log(1 + \tau^2 \omega^2) \tag{4.12}$$

and the phase will be

$$\text{Phase}_{\text{lp}}(\omega) = -\tan^{-1}(\tau\omega). \tag{4.13}$$

The cutoff frequency of the filter, defined as the frequency at which the gain is -3dB, can be found using equation (4.12) and is

$$f_{-3\text{dB}} = \frac{1}{2\pi\tau}. \tag{4.14}$$

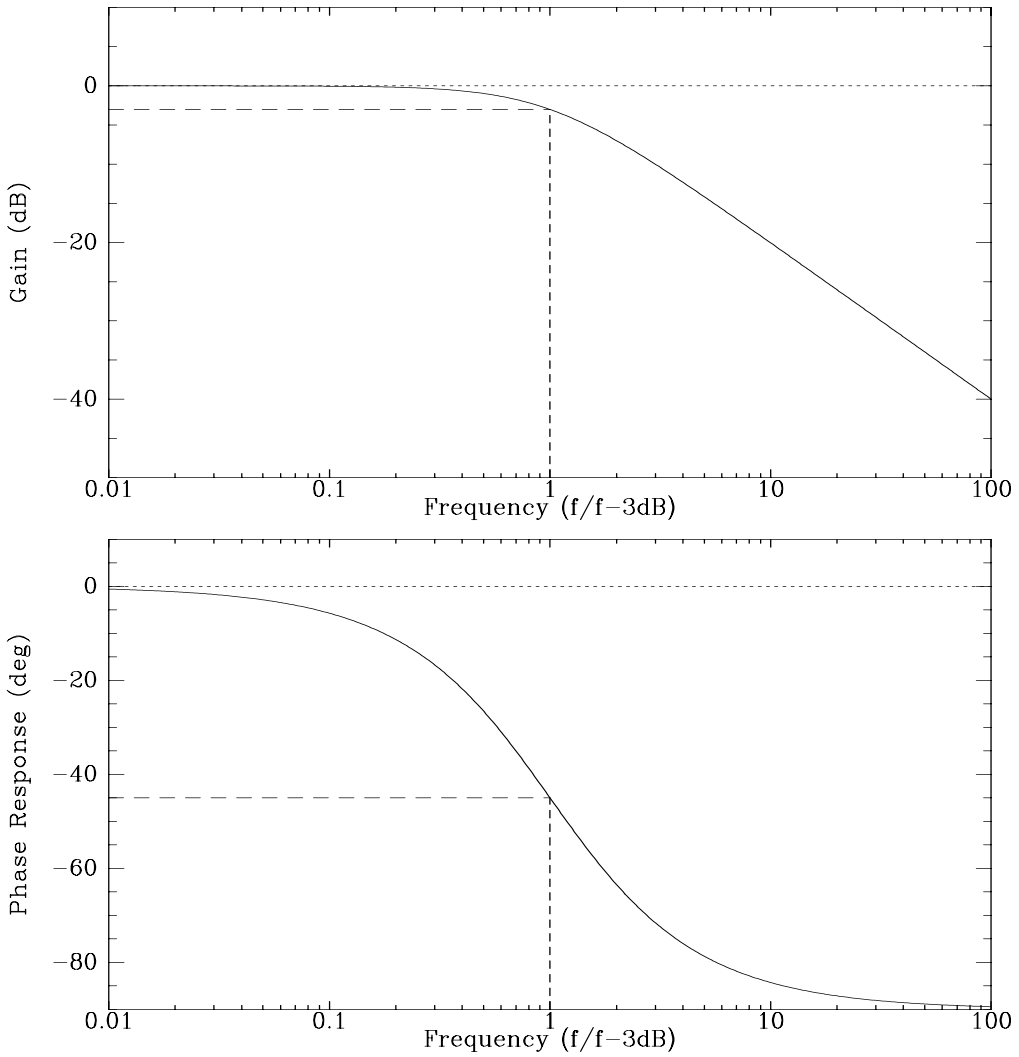

Figure 4.1: These plots show the results of the model of a low pass or simple lag filter expressed in equations (4.12) and (4.13). At the 'cutoff' frequency of $f_{-3\mathrm{dB}}$ the phase reaches a 45^o lag while the gain is at -3 dB.

Figure (4.1) shows plots of these functions. Plots of this kind are generally referred to as *Bode* plots. Note that at the -3 dB point the phase is lagging by 45^o, which will be used as a criterion for finding the cutoff frequency of other, more complex, systems.

To study the dynamics of a linear physical system, one need only find its transfer function. Using equations (4.10) and (4.11) the behaviour of the system, in terms of its effect on the amplitude and phase of any input signal, is easily calculated.

4.1.3 $\mathcal{Z}$ Transforms

While the Laplace transform and transfer function are very useful in the analysis of analogue devices, in order to study the behaviour of digital apparatus we need to use a $\mathcal{Z}$ transform defined for digital data. Before we can use this transform it is necessary to employ a *modulation model* of the analogue function $i(t)$ using a delta function as a *sampler* to produce the equivalent digital series $i^*(t) = i_0, i_1, i_2, \cdots$ given by

$$i^*(t) = \sum_{k=0}^{\infty} i(t)\,\delta(t - kT) \tag{4.15}$$

where T is the sampling time of the digital system and $k = 0, 1, 2, \cdots$.

Given the digital signal is $i^*(t)$ we then define its one-sided $\mathcal{Z}$ transform to be

$$I(z) \equiv \mathcal{Z}[i^*(t)](z) \equiv \sum_{k=0}^{\infty} i_k z^{-k} \tag{4.16}$$

where z is a complex variable and $r_0 < |z| < R_0$ with r_0 and R_0 chosen such that the series converges. This is the digital equivalent of the Laplace transform as it maps real data to a complex function of a complex variable.

The $\mathcal{Z}$ transform has properties very similar to those of the Laplace transform. The major conceptual differences lie in the fact that the $\mathcal{Z}$ transform forces one to think in terms of time while Laplace transforms are easier to deal with in terms of frequency. For example, instead of considering the differentiation with respect to time of a signal we should deal with a time shift:

$$\begin{aligned}
\mathcal{Z}[i^*(t - nT)](z) &= \sum_{k=0}^{\infty} i_{k-n} z^{-k} \\
&= \sum_{k=0}^{\infty} i_k z^{-(k+n)} \\
&= z^{-n} \sum_{k=0}^{\infty} i_k z^{-k} \\
&= z^{-n}\,\mathcal{Z}[i^*(t)](z).
\end{aligned} \tag{4.17}$$

Note the similarity of this relationship to that set out in equation (4.5). Some other general properties of the $\mathcal{Z}$ transform are listed in table (4.3).

Transfer functions are also defined as the ratio of the $\mathcal{Z}$ transform of the output to that of the input. We shall use as an example the digital equivalent of the low pass filter discussed in section (4.1.2),

$$o_n = i_n - \frac{\tau}{T}(o_{n-1} - o_{n-2}) \tag{4.18}$$

Description	$i^*(t)$	$I(z)$
Similarity	$i^*(at)$	$aI(z)$
Addition	$i_1^*(t) + i_2^*(t)$	$I_1(z) + I_2(z)$
Shift	$i^*(t - kT)$	$z^{-k}I(z)$
Geometric Progression	$\alpha^{-k}i^*(t)$	$I(\alpha z)$

Table 4.3: Some general properties of the $\mathcal{Z}$ transform.

where once again τ is the lag time and T is the sample time. If $I(z)$ is the $\mathcal{Z}$ transform of the input $i^*(t)$ and $O(z)$ is the $\mathcal{Z}$ transform of the output $o^*(t)$ the equivalent expression in the complex plane is

$$O(z) = I(z) - \frac{\tau}{T}\left(z^{-1}O(z) - z^{-2}O(z)\right). \tag{4.19}$$

The transfer function is then

$$T_{\text{lp}^*}(z) \equiv \frac{O(z)}{I(z)} = \frac{1}{1 + \frac{\tau}{T}\left(z^{-1} - z^{-2}\right)}. \tag{4.20}$$

To make use of the $\mathcal{Z}$ transform transfer function and construct models of hybrid systems, such as the tilt correction servo, we need to map it to its equivalent Laplace transform. This can be achieved by using the modulation model. Combining equations (4.15) and (4.1) it is easy to show that

$$\mathcal{L}(i(t)) = \mathcal{Z}[i^*(t)]\left(e^{-st}\right). \tag{4.21}$$

So, in the case of the low pass filter, the equivalent Laplace transfer function is

$$\begin{aligned} T_{\text{lp}}(s) &= T_{\text{lp}^*}\left(e^{st}\right) \\ &= \frac{1}{1 + \frac{\tau}{T}\left(e^{-sT} - e^{-2sT}\right)}. \\ &\simeq \frac{1}{1 + \tau s} \text{ when } |s| << \frac{1}{T} \end{aligned} \tag{4.22}$$

which is identical to the analogue expression in equation (4.9). With these tools we can analyse the digital and analogue components of a system separately and then combine them into one single linear model of the entire device.

4.1.4 Negative Feedback Models

For systems such as the tilt correction servo, it is normal to perform the analysis using a *negative feedback model*. Negative feedback means that the output of a

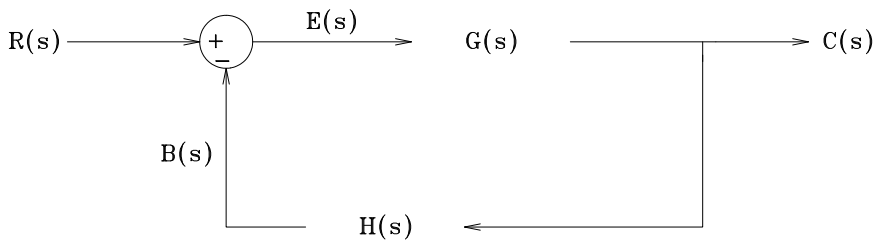

Figure 4.2: The standard negative feedback loop. Note that all signals are written as the Laplace transform of the signal and all devices are written as the transfer function of the device. In this case $R(s)$ is the input signal, $C(s)$ is the output signal, $G(s)$ is the gain transfer function and $H(s)$ is the feedback transfer function. Almost all linear control systems that involve feedback can be analysed using a diagram similar to this one.

system is subtracted from the input to create an error signal. Positive feedback systems, where the output is looped back around and added to the input, also exist but are, on the whole, not stable. Negative feedback systems are normally drawn as shown in figure (4.2) and the analysis is performed in the complex Laplace transform plane.

If the transfer functions of the gain, $G(s)$, and feedback, H(s), are known, the performance of the entire system can be found. If $B(s)$ is the transform of the feedback signal

$$B(s) = H(s)C(s) \tag{4.23}$$

and $E(s)$ is the transform of the error signal

$$E(s) = R(s) - B(s) \tag{4.24}$$

the output of the system can be written

$$\begin{aligned} C(s) &= G(s)E(s) \\ &= G(s)(R(s) - B(s)) \\ &= G(s)(R(s) - H(s)C(s)). \end{aligned} \tag{4.25}$$

The transfer function of the system is then

$$T_{\text{sys}} = \frac{C(s)}{R(s)} = \frac{G(s)}{1 + G(s)H(s)}. \tag{4.26}$$

Once the transfer function for the entire system is known, the complex gain can be found and analysis can continue using equations (4.10) and (4.11). The transfer function can also be used to investigate servo stability by looking for its poles. If a pole lies on the left hand half of the s plane[1] the system is stable, if it lies on the right hand side the system is either neutral or unstable. More analysis tools using transfer functions are described in Dorf (1974) and other linear control texts.

To illustrate negative feedback we once again turn to the low pass filter. This filter can be modelled several ways, the most obvious being

$$\begin{aligned} G(s) &= 1 \\ H(s) &= \tau s \end{aligned} \tag{4.27}$$

where the feedback device performs a differentiation and the gain part of the circuit does nothing. Substituting these functions into equation (4.26) yields an expression identical to equation (4.9). Another way of expressing the low pass filter in terms of a negative feedback loop is setting

$$\begin{aligned} G(s) &= \frac{1}{\tau s} \\ H(s) &= 1. \end{aligned} \tag{4.28}$$

In this case the feedback system does nothing, while the gain part performs an integration. This illustrates a general property of negative feedback systems, that is, differentiation in the feedback loop is equivalent to an integration in the gain part of the circuit. In Laplace transform space this translates to multiplication in the feedback loop being the same as a division in the gain and *vice versa*.

4.2 Model of the Control System

With the mathematical tools of Laplace transforms, $\mathcal{Z}$ transform and negative feedback, we are now in a position to construct a linear model of the tilt correction servo. In order to build this model we first draw a diagram, similar to figure (4.2), that represents the adaptive optics system. Given this diagrammatic representation we can then proceed to build linear models of each of the

[1] That is, the imaginary coefficient is negative.

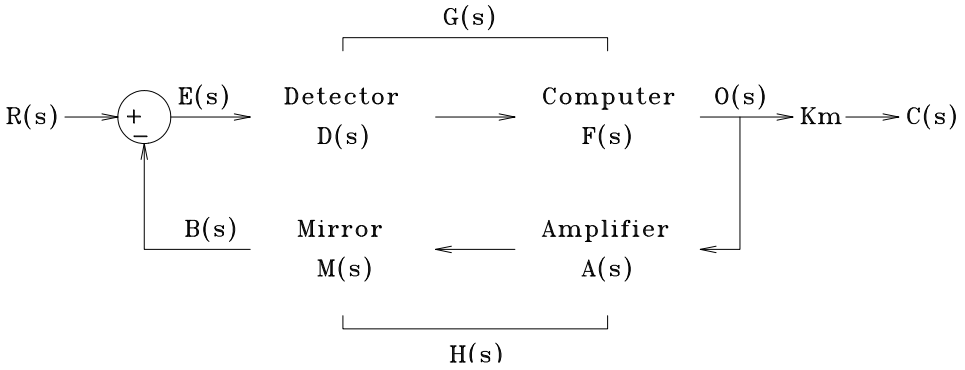

Figure 4.3: The tilt correction servo analysed as a negative feedback loop. The tilt of the incoming beam is $R(s)$, the corrected output beam going on to the rest of the optical table is $E(s)$ while the output of the computer system, which represents a measurement of wavefront tilt, is $C(s)$. The 'subtraction' is performed by the tilt mirror itself. The final multiplication of the computer output by the calibration constant K_m, ensures that the output of the system is in the same units as the input.

components of the system by constructing the various transfer functions of the individual components. Combining these transfer functions we then obtain the transfer function of the entire system, from which useful predictions can be made.

A diagram of the tilt correction servo viewed as a negative feedback system is given in figure (4.3). The error signal $E(s)$ represents the resulting angle between the beam and the optical axis of the interferometer. This is measured by the quadrant detectors, whose transfer function is $D(s)$, and processed by the control computer with the transfer function $F(s)$. The gain component of the feedback loop is therefore

$$G(s) = D(s)F(s). \tag{4.29}$$

The output of the control computer, $o^*(t)$ is a number between -1 and $+1$ and represents a normalised measurement of the tilt of the incoming beam. If this number is multiplied by the mirror calibration constant K_m discussed in section (3.2.2) the results can be recorded in the correct units and stored for later processing and analysis.

This normalised beam tilt measurement is processed by the high voltage amplifier $A(s)$ and subtracted from the optical beam by the tilt mirror $M(s)$.

The feedback component of the system is therefore

$$H(s) = A(s)M(s). \tag{4.30}$$

There are two transfer functions of primary interest. The first transfer function describes the ability of the mirror $C(s)$ to track the real tilt of the beam R(s) defined

$$T_{\text{track}}(s) \equiv \frac{B(s)}{R(S)}. \tag{4.31}$$

We shall use this transfer function to study how well the system actually removes tilt. The second transfer function of interest is

$$T_{\text{measure}}(s) \equiv \frac{C(s)}{R(S)} \tag{4.32}$$

which describes the ability of the system to measure the incoming beam tilt. Using an analysis similar to that used to produce equation (4.26) it can be shown that these transfer functions are

$$T_{\text{track}}(s) = \frac{-G(s)H(S)}{1 + G(S)H(s)} \tag{4.33}$$

and

$$T_{\text{measure}}(s) = \frac{K_m\, G(s)}{1 + G(s)H(s)}. \tag{4.34}$$

Equations (4.33) and (4.34) will enable the determination of the usable servo bandwidth for tracking and measurement of beam tilt.

The transfer function of the control computer can be directly calculated, while those of the high voltage amplifier, detectors and mirrors need to be modelled and fitted to experimental data. Once these empirical parameters and transfer functions are known the complex gain of the adaptive optics system can be found and its performance analysed.

4.2.1 Detector Model

The quadrant detectors measure the beam tilt $\theta_{v,h}(t)$ and produce a normalised output variable $\phi_{v,h}(t)$ which can be read by the control computer. Once again, as the vertical and horizontal systems are identical, we will drop the v and h subscripts. The equation representing the response of the detectors was derived in section (3.1.3) as $\phi(t) = K_d\theta(t)$, so the transfer function of the detector system can be written as

$$D(s) \equiv \frac{\Theta(s)}{\Phi(s)} = \frac{1}{K_d}. \tag{4.35}$$

This expression is correct only if the angular error of the beam is small. If this is not the case the detectors become extremely non-linear and will no longer be stationary, making linear analysis impossible. During operation servo errors of this kind should only result from large amplitude high frequency changes in beam tilt. As the theoretical analysis performed in section (2.3.2) demonstrates, the high frequency component of the tilt power spectrum is small, so these errors should not be significant. It is reasonable to suppose, however, that the high frequency behaviour predicted by this linear model will not exactly match that produced by the real system.

4.2.2 Computer System Model

The sole component of the system that can easily be adjusted is the software running in the control computer. The programme receives a modulated and sampled signal $\phi^*(t)$ as input representing the normalised beam tilt $\phi(t)$ which can be written, using equation (4.15), as

$$\phi^*(t) = \sum_{k=0}^{\infty} \phi(t)\delta(t - kT) \tag{4.36}$$

where T is the sample time of 1 ms. This series of samples, which we assume to have the $\mathcal{Z}$ transform $\Phi(z)$, must be processed in some manner by the computer and sent out as the output signal $o^*(t)$ with the $\mathcal{Z}$ transform $O(z)$. The most common, and general, choice for a first order processing algorithm is what is known as a proportional, integrating and differentiating controller (PID), that is, one whose output depends on the input signal, its integral over time and its rate of change. The proportional term is the gain of the system, the integral term is responsible for correction of long term drift and the differential term represents damping. Since the star guidance servo to be discussed in section (4.3) corrects for drift a controller algorithm was chosen that only contains the proportional and damping components. Furthermore, as shown in section (3.3.1), larger sample times than 1ms will be required for the fainter objects so a running mean over a variable number of samples was added to the control equation. The algorithm used in the control computer, using C_1 as the constant of proportionality, C_2 as the damping constant and T_d as the time over which the running mean is calculated is

$$\underbrace{o_k - o_{k-1}}_{Change\,in\,output} = \underbrace{\frac{C_1 T}{T_d} \sum_{j=1}^{T_d/T} \phi_{k-j}}_{Proportional\,term} - \underbrace{C_2(o_{k-1} - o_{k-2})}_{Damping\,term}. \tag{4.37}$$

This equation was implemented on the control computer in the C programming language purely using integer arithmetic. Even without floating point arithmetic and a relatively fast processor, many problems were encountered in achieving the necessary speed for a 1ms minimum sample time. This was overcome by a combination of assembly code[2] and the distribution of less time critical calculations over several sample cycles. For example, since the total light intensity will only change slowly, the division by the total counts in equation (3.1) need not be performed every cycle.

The $\mathcal{Z}$ transform of equation (4.37) is

$$O(z) - z^{-1}O(z) = \frac{C_1 T}{T_d} \sum_{j=1}^{T_d/T} z^{-j} E(z) - C_2(z^{-1}O(z) - z^{-2}O(z)) \tag{4.38}$$

which means the transfer function must be

$$F^*(z) \equiv \frac{O(z)}{E(z)} = \frac{\frac{C_1 T}{T_d} \sum_{j=1}^{T_d/T} z^{-j}}{1 - (C_2 - 1)z^{-1} - C_2 z^{-2}}. \tag{4.39}$$

The equivalent analogue form for this expression is found by invoking the modulation model and replacing z by e^{-sT} resulting in

$$F(s) = F^*(e^{-sT}) = \frac{\frac{C_1 T}{T_d} \sum_{j=1}^{T_d/T} e^{-jsT}}{1 - (C_2 - 1)e^{-sT} - C_2 e^{-2sT}}. \tag{4.40}$$

As this part of the servo is completely implemented in software, the ability of this transfer function to predict the behaviour of the control system could be checked. A test programme was written including the same code used by the control computer, to generate sampled sine waves of varying amplitudes and frequencies, feed them through the control algorithm and record the results. The gain and phase shift of the control computer could then be measured. The results of a number of these tests are shown in figure (4.4) and show that equation (4.40) correctly predicts the response of the algorithm expressed in equation (4.37). Once again the predicted behaviour is significantly different to the measured behaviour at high frequencies only, mostly due to the Nyquist limit of the system being approached. As this transfer function only starts to fail at frequencies much larger than those for which the servo is expected to operate, it can be included in our system model without change.

[2]Assembly code modifications included re-writing the multiplication, division and input/output routines of the C complier used which, while very general, were not optimised for speed.

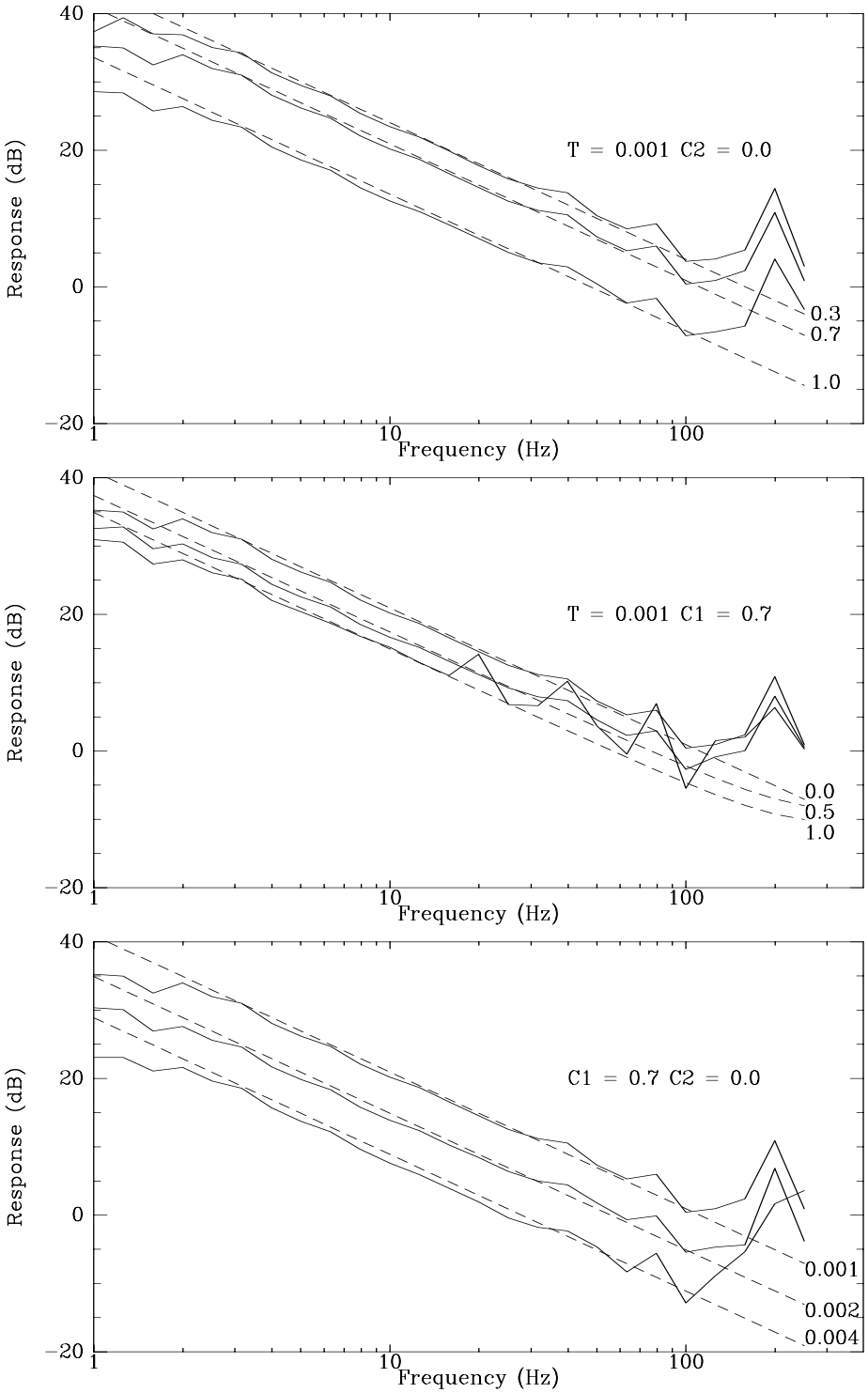

Figure 4.4: The theoretical (dotted lines) and the measured (solid lines) response of the control computer algorithm. These plots were generated by substituting equation (4.40) into equations (4.10) and (4.11). The ability of the transfer function to predict the response of the control system is clear, except at high frequencies, where the sample time of the system starts to play a large role in determining its behaviour, and at very low frequencies, where the theoretical gain implies outputs larger than can be accommodated by an integer variable in the computer.

4.2.3 High Voltage Amplifier and Tilt Mirror Model

The behaviour of the combination of the high voltage amplifier and the tilt mirrors is complex and difficult to measure. The measurements performed on the amplifiers in section (3.3.2) suggest the simple low pass filter of the form

$$H(s) = \frac{K_m}{1 + \tau_A s} \tag{4.41}$$

as a good starting point for a model of this part of the system. The mirror calibration constant K_m is added so the normalised output of the control computer is correctly shifted to arcseconds and the lag time τ_A will need to be found by fitting the response of the system to measurements.

Attempts were made to measure the response of the amplifier/mirror combination by sending sine waves of various frequencies to the amplifier input and monitoring the response with a quadrant detector. Unfortunately, as the linear range of the detectors is much smaller than that of the mirrors, and largely within the range of the random angular errors generated by the internal thermal noise of the enclosure, these measurements only represent the low amplitude mirror response and are very noisy. An example of the results is shown in figure (4.5) along with the 'best fit' low pass filter model[3]. While the shape of this curve shows that a low pass filter is indeed a good starting point for a model, it is also clear that the mirror's behaviour is more complex.

Texts that describe the modelling of piezo controllers, such as Tyson (1991), state that a damped harmonic oscillator is the most appropriate model, but this resulted in fits no better than the low pass filter. Many other forms of transfer function were tried, including quadratic lag and complex polynomials up to order five, with no better results. As the piezos used in the tilt mirrors were purchased for the prototype instrument some years ago, before the appearance of specialised control electronics for driving them, they suffer from hysteresis. Furthermore, as figure (4.5) demonstrates, the high frequency response is greater than is predicted by a simple lag system. In an attempt to model this, a second differential term was added to the equation describing a low pass filter. The resulting form of the differential equation representing the combination of the

[3]The device used to make these, and all other similar measurements throughout this thesis, was a Hewlett Packard 3562A Dynamic Signal Analyser which could directly measure histograms, frequency responses, power spectra and so on. The data were then transferred to a computer using the GPIB data bus.

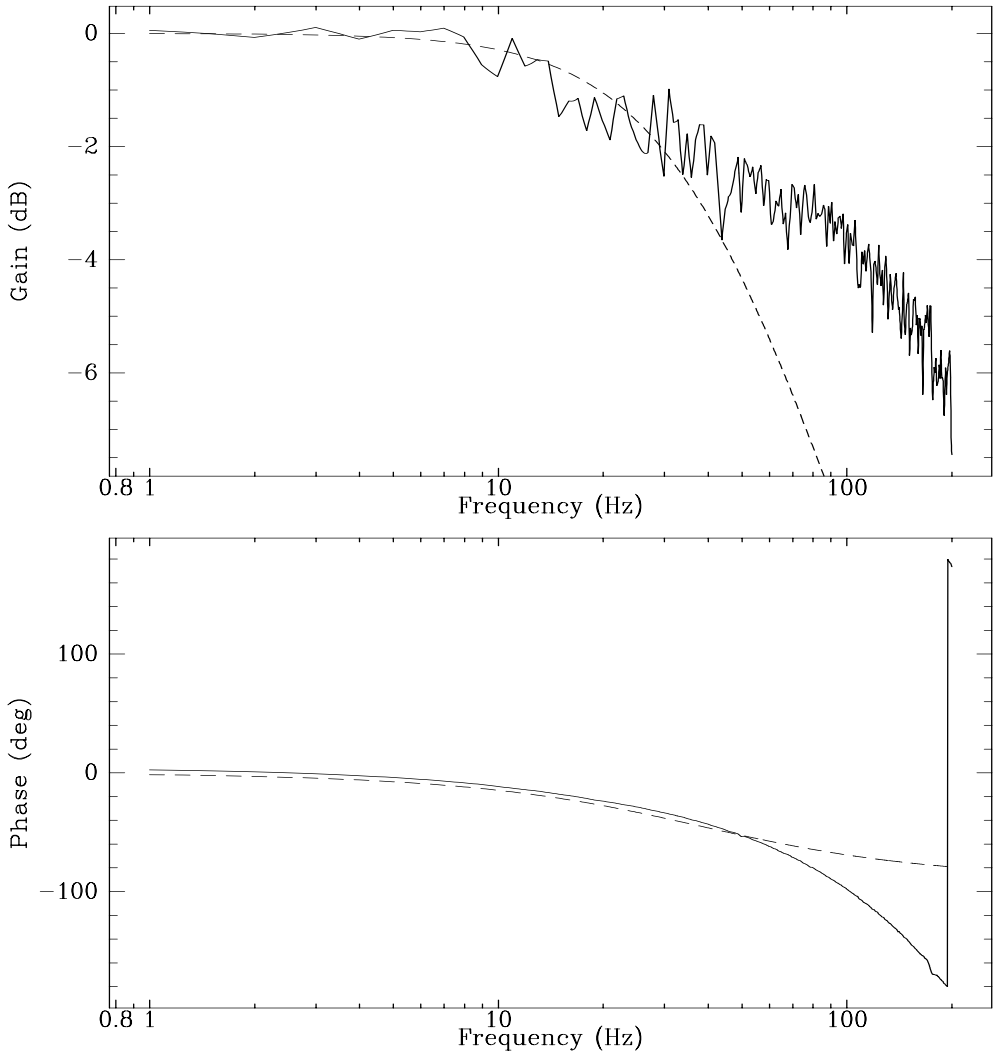

Figure 4.5: The measured response of the tilt mirror/high voltage amplifier combination. The best fit of the low pass filter response is also shown as a dashed line. Phase (the bottom plot) fits well, but the gain predicted by a low pass filter drops below that measured at high frequencies. Clearly, while a low pass filter model is a good first approximation to the data, it does not successfully describe the performance of the system.

amplifier and mirror is

$$b(t) = \underbrace{\underbrace{\underbrace{K_m o(t)}_{Proportional} - \underbrace{\tau_A \frac{db(t)}{dt}}_{Damping}}_{LowPassFilter} + \underbrace{K_m \tau_M \frac{do(t)}{dt}}_{Correction}} \tag{4.42}$$

with the transfer function

$$H(s) = \frac{K_m(1 + \tau_M s)}{1 + \tau_A s}. \tag{4.43}$$

This transfer function with its extra time constant τ_M may seem rather *ad hoc*, but it does produce better fits to the experimental data set than any of the other functions tried, some of which have many more free parameters than the two contained in this expression. One way of interpreting this correction factor is to assume there is a resonance in the mirror system with a frequency greater than a few hundred hertz. As the system contains three piezo electric actuators it is very stiff so a high frequency resonance is to be expected. The effect of such a resonant peak at low frequencies would be an increase in gain as the frequency increases towards this resonance. The simple linear correction term can be seen as a model of the tail end of this resonant peak. As no data is available for very high frequencies a more detailed resonant model is inappropriate.

4.2.4 Frequency Response Measurements

By combining equations (4.35), (4.40), (4.29) and (4.43) with either (4.33) or (4.34) we can derive the theoretical servo response for tracking or measuring beam tilt. However, there are still three parameters not known to great precision. Two of these are the time constants in the feedback circuit, τ_A and τ_M and the third is the detector calibration constant K_d which, while estimated at $1Hz$ in section (3.1.3), is not accurately known. A number of adjustments have been made to the optics, including the quadrant detectors, since the first estimate was obtained, so it may only be considered a good first approximation to the required value.

These free parameters can be found by measuring the complex gain of the entire tilt correction servo for a range of values of the servo parameters C_1, C_2 and T and performing a least squares fit of the linear model. To be able to measure the frequency and phase response of the servo it is necessary to be able to introduce tilt of known amplitude and phase into the beam and compare this with the output signal $c(t)$ of the system. The initial approach used one mirror to introduce tilt and a second mirror to servo it out as shown diagrammatically

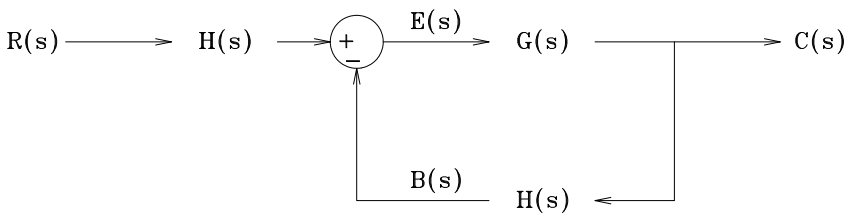

Figure 4.6: Linear feedback model of first calibration system. The first amplifier/mirror system $H(s)$ is used to introduce known amounts of tilt into the beam, while a second mirror system is used to correct it. This results in the response of the mirror system being included twice in the measurement.

in figure (4.6). Using the methods outlined above it can be shown that the transfer function of this calibration setup is

$$T_{\mathrm{cal}_1}(s) = \frac{G(s)H(s)}{1 + G(s)H(s)} \tag{4.44}$$

where, as would be expected, the transfer function of the mirror/amplifier system is included twice. Note that, apart from a phase change of 180 degrees, this expression is identical to equation (4.33), the transfer function for the tracking ability of the servo. In this way we can measure the real performance of the tilt servo. While this configuration worked well on the test bench in the laboratory, it was not suitable for use in the instrument itself where the two mirrors are placed 70m apart at either end of the OPLC. In this case, instead of using a second mirror to introduce the test signals, a flat was used to autocollimate the beam and the signals were injected directly into the feedback path as shown in figure (4.7). The transfer function of this calibration setup is

$$T_{\mathrm{cal}_2}(s) = \frac{-G(s)H(s)}{1 + G(s)H(s)} \tag{4.45}$$

which is identical to equation (4.33). Other advantages of performing the experiments in this manner are the ease in which these signals can be introduced electronically into any of the four independent servos and the fact that no extra optics or electronics are required. Probably the most important advantage of this measurement technique is that it can be used while tracking a star.

Using the laser and spatial filter once again as an artificial star many frequency response measurements were carried out on the tilt servo for a wide range

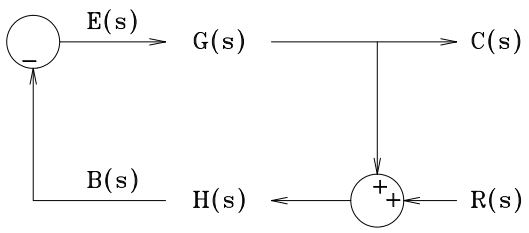

Figure 4.7: Linear feedback model of final calibration system. While this system has almost identical dynamics of the system shown in figure (4.6) it requires no extra optics and can be used *in situ* in the interferometer itself.

of servo parameters. The lowest value of C_1 was the smallest possible while still allowing the servo to function and the highest C_1 value used was the largest value possible without allowing the system to oscillate. These experiments resulted in more than 60 000 data points. Although the air inside the optical enclosure was allowed to settle for a number of hours before the experiment commenced, residual air turbulence remained, causing bad signal to noise ratios in the low frequency parts of the measurements. For this reason non-repeatable peaks in these data were smoothed out.

The final step in producing the servo model is to perform a least squares fit of the unknown parameters K_d, τ_A and τ_M. Many alternatives for performing this fit are available, each giving a different weighting on the data. For example, one may perform the fit in the complex plane, fit magnitude or phase only, or fit magnitude in decibels. The nature of the equipment used in data collection was such that frequency was scanned linearly, which means that if the data is shown on a log plot the higher frequencies are over sampled. Fitting magnitude in decibels thus gives too high a weight to the high frequency data so it can not be used. Two fits were performed on a sample of the data, one in the complex plane and one to magnitude alone, the results of which are shown in figure (4.8).

It was found that the fit in the complex plane produced an excellent fit to the phase response and not such a good fit to the gain, while the fit to magnitude only had the reverse behaviour. In choosing between these methods we must first decide which features of the complex gain we are most interested in predicting. There are two applications of this model to consider. One is choosing optimal

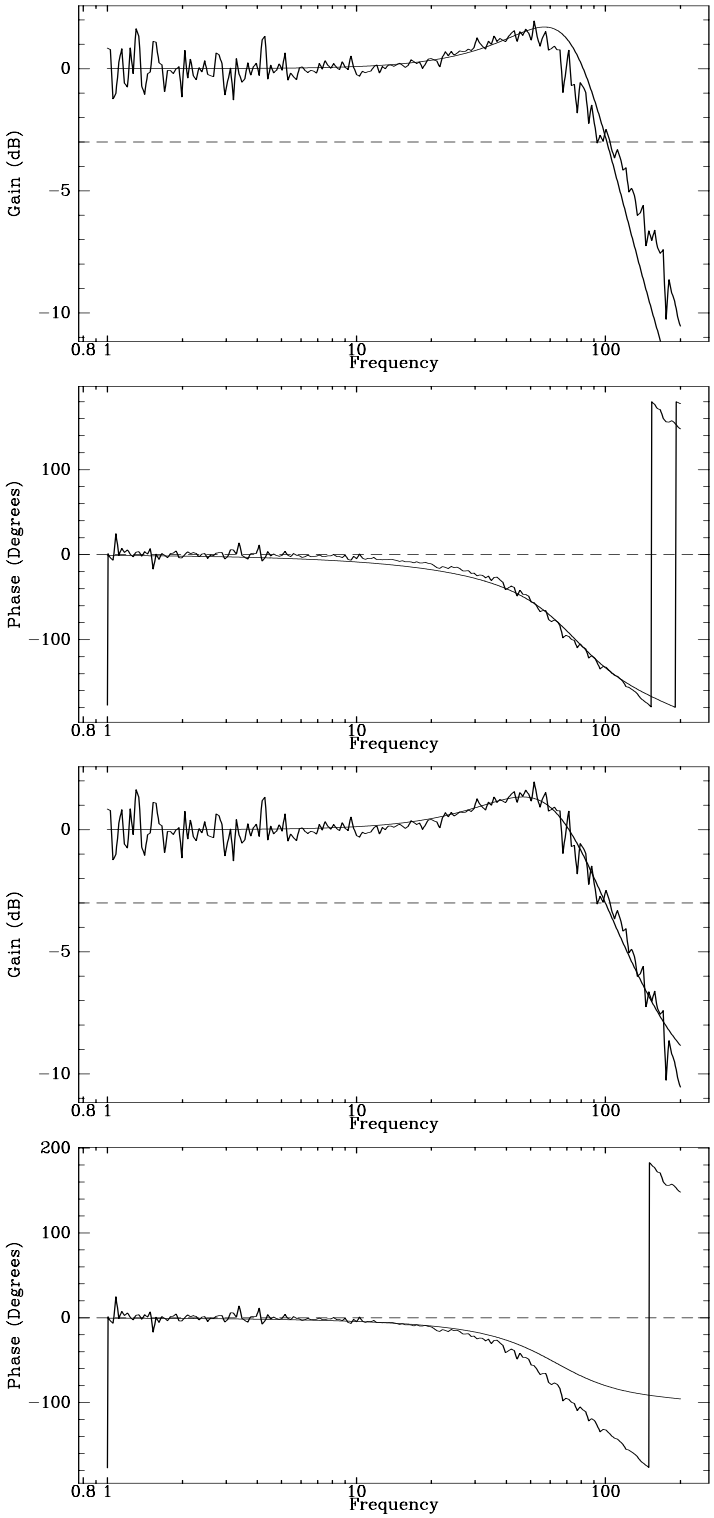

Figure 4.8: Two fits, one in the complex plane (top two plots) and one performed on magnitude alone (bottom two plots). The fit in the complex plane fits phase well while the fit to magnitude only fits magnitude well. Refer to text for more discussion of these plots.

servo parameters for a given sample time and required bandwidth (or -3dB frequency), in which case we are most interested in the size of the resonant peak, the cutoff frequency and, to a lesser extent, the phase response. The second application will arise in the following Chapter when we wish to fit the theoretical power spectrum of tilt derived in section (2.3.2) to the data collected by the tilt correction system. In this case we are primarily concerned with the frequency range in which the gain response is flat. Furthermore, the values found for the unknown parameters using either fit differed only by small amounts. The fit to magnitude alone was therefore selected and used to fit all data, as it predicts the size of the resonant peak and the cutoff frequency well. The fit to phase is acceptable in the low frequency range. The resulting values for the free parameters are

$$\begin{aligned} K_d &= 1.7 \pm 0.3 \text{ arcsec} \\ \tau_A &= 2.2 \pm 0.2 \times 10^{-3} \text{ s} \\ \tau_M &= 2.2 \pm 0.2 \times 10^{-4} \text{ s} \\ \text{RMS residue} &= 0.08 \text{ dB} \end{aligned}$$

where the errors quoted are the changes required to double the RMS residue of the fit. Note that the value found for K_d matches the value of 1.71 ± 0.02 predicted in section (3.1.3). This gives us confidence in using the values predicted for other aperture sizes. A sample of the raw and fitted data is given in figure (4.9). It is interesting to note that the largest bandwidth found possible was approximately 160 Hz, which coincides with the cutoff frequency found for the high voltage amplifiers in section (3.3.2). Assuming there is plenty of light available, the response of the system is restricted by the performance of the tilt mirrors themselves. If the current mirrors were replaced with one of the newer piezo systems available today, superior system performance could be achieved.

4.2.5 Optimisation of Control Parameters

Now that a model for the servo system is available we can proceed to find optimal values for the two servo parameters. Given a particular sample time, based on the amount of light reaching the detectors, and bandwidth, based upon the measured behaviour of the atmosphere, the optimal values for the constants C_1 and C_2 must be found, such that the resonant peak is as small as possible in both height and width. We are interested in both the tracking and measurement performance of the system. Parameters will be chosen primarily

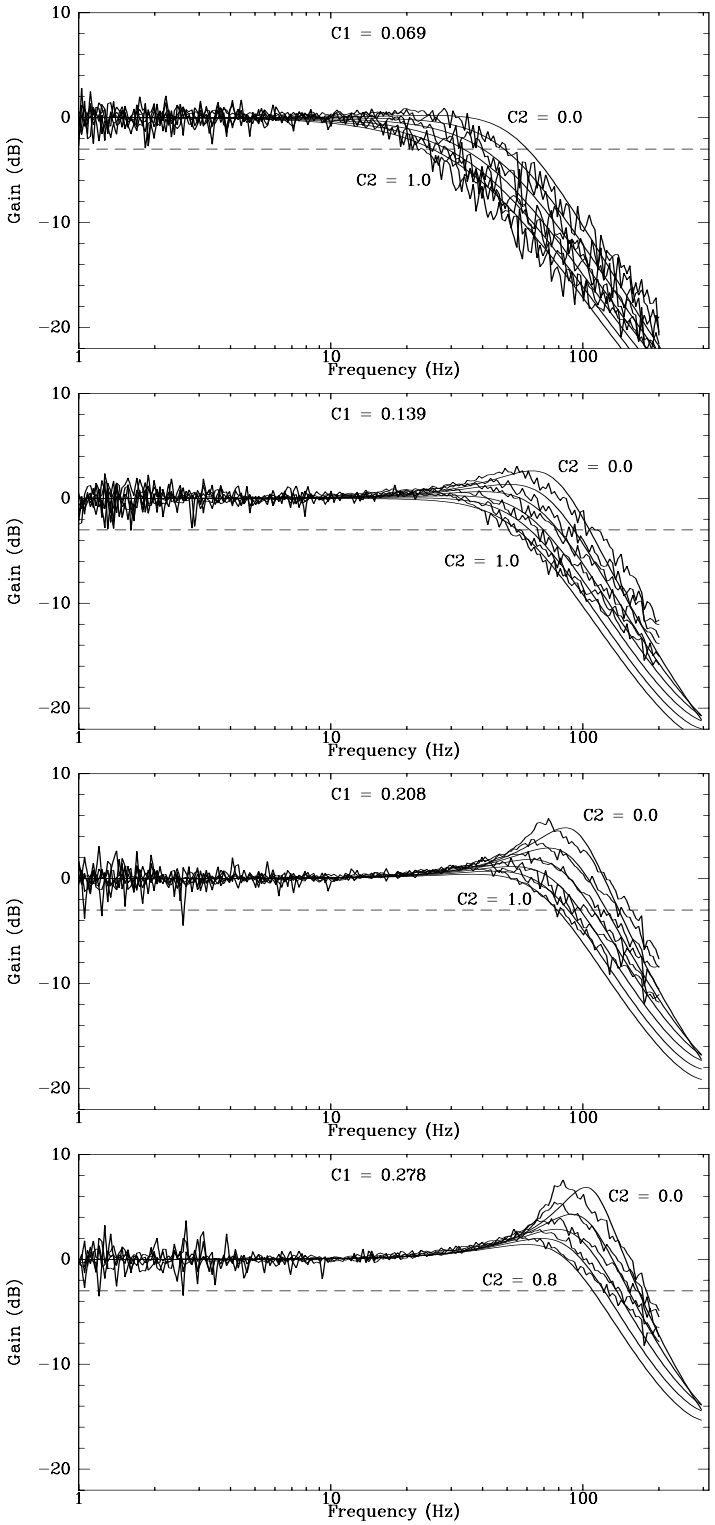

Figure 4.9: A sample of the raw and fitted data for the complex gain of the tilt servo for a range of values of C_1 and C_2. Note that the size of the resonant peak and the position of the -3dB point match well.

from the tracking bandwidth they imply, however, if the measurement response contains a peak of more than 3dB they will not be accepted.

As shown in section (3.3.1) at least 40 photon events per sample time is required to keep the detector error to less than 0.1". This is the minimum count allowable before the servo becomes unstable. It is recommended the smallest sample time possible is chosen so at least 100 counts are received in each detector per sample. Of course, larger count rates will improve signal to noise and should be used if possible.

The bandwidth required of the servo should match the current cutoff frequency of the tilt spectrum described in section (2.3.2). If the bandwidth of the servo is smaller than this cutoff frequency a significant fraction of the tilt will not be removed. Alternatively, if the bandwidth of the servo is much greater than that of the tilt spectra the servo will only amplify the photon noise present in the detector, with little or even detrimental effect on the stability of the image. This cutoff frequency, derived earlier as $v_\perp/\pi R$, lies in the range of zero to less than 50Hz. If the cutoff frequency is much larger than this it implies a very large average perpendicular wind speed, under which conditions observations are unlikely to take place. The procedure used to find this cutoff frequency is as follows. After having chosen the sample time the servo is set to the maximum possible bandwidth. This is likely to be undesirable for image stabilisation, but is useful for the measurement of the tilt spectra (to be discussed in section (5.2)). The cutoff frequency of the tilt spectra can then be used as an estimate of the optimal bandwidth of the servo. As seeing can vary considerably with time, this optimal bandwidth measurement should be repeated periodically throughout an observational run.

Unfortunately, as figure (4.8) shows, it is not obvious how one should define the bandwidth of the tilt servo. Once again using a low pass filter as an example, the -3 dB frequency of the amplitude response is usually used to define the bandwidth. At this frequency the power of the output response is half that of the input and the phase of the output lags the input by 45^o. The -3dB frequency of the tilt servo does not coincide with this 45^o phase lag frequency, in fact it is always somewhat larger. Even if the amplitude response is perfect at a given frequency, if the phase lag is too large the servo will produce little or no improvement in image stability. The -45^o frequency predicted by the model was found to lie always slightly above the measured 45^o frequency and below the -3dB amplitude response frequency. Thus, the bandwidth of the servo will be defined as the frequency at which the model predicts the 45^o phase lag, written as f_{-45^o}.

Bandwidth f_{-45^o} Hz	C_1	C_2	Track Gain$_{\text{res}}$ dB	Track f_{res} Hz	Track f_{-3dB} Hz	Measure Gain$_{\text{res}}$ dB	Measure f_{-3dB} Hz
5.0	0.007	0.08	-0.13	< 1.0	5.9	-0.13	5.9
10.0	0.014	0.01	-0.02	< 1.0	13.9	-0.02	14.4
15.0	0.027	0.28	-0.01	< 1.0	23.5	-0.01	25.8
20.0	0.034	0.12	0.00	< 1.0	37.1	0.00	44.2
25.0	0.074	0.93	0.00	< 1.0	45.0	0.00	56.9
30.0	0.095	0.96	0.00	8.1	56.6	0.37	75.5
35.0	0.115	0.95	0.15	26.3	68.2	1.04	95.4
40.0	0.135	0.92	0.44	37.3	79.6	1.83	117.4
45.0	0.155	0.88	0.78	46.4	91.0	2.66	142.5
47.6	0.175	0.97	0.90	49.8	95.9	2.97	161.8

Table 4.4: The optimal servo parameters for a range of bandwidths are shown here for a sample time of 1ms and an aperture diameter of 35mm on the optical table.

The final criterion in choosing the servo parameters is the size of the resonant peaks in the tracking and measurement responses. If either peak is too large the servo will be adding tilt to the beam at this frequency instead of removing it. Usually a peak of no more than 3dB is considered to be acceptable as this is the frequency where the servo output contains twice the energy of the input. The output of the system is then at least no worse than without the servo. Of course, if a set of servo parameters can be found that produce a smaller resonant peak, they should be used.

The linear model of the tilt servo was used to find values of C_1 and C_2 fitting these criteria for a range of sample times and bandwidths. The resulting values for the fastest sample time of 1ms are listed in table (4.4). A complete set of optimal servo parameters can be found in Appendix D. Once again the maximum $f_{-3\text{dB}}$ bandwidth for the servo was found to be of the order of 160 Hz. This is very close to the $f_{-3\text{dB}}$ frequency measured for the high voltage amplifiers in section (3.3.2). Ultimately the response of the tilt servo can be no better than the response of the tilt mirrors themselves.

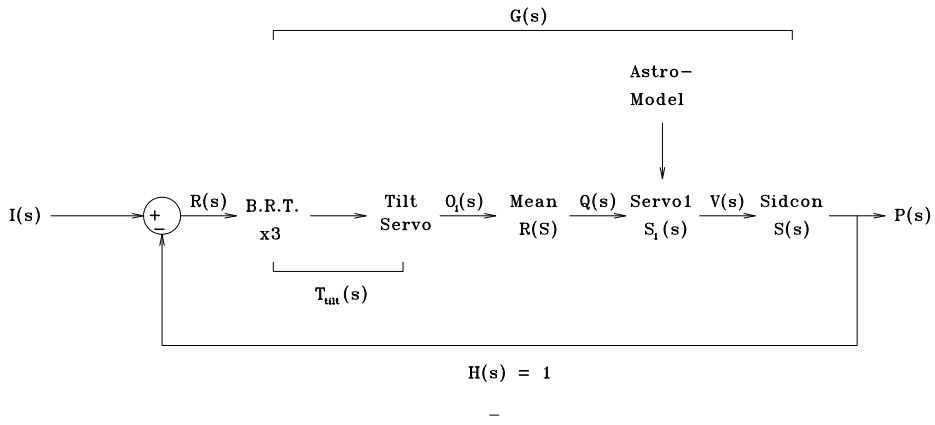

Figure 4.10: The star guidance servo drawn as a negative feedback loop. The average position of the tilt correction mirrors is used as an error signal. This is then combined with the positions and velocities generated by the astrometric model and sent to the siderostat control computer *sidcon*. The response of this system must be restricted to less than a few hertz to ensure that it does not conflict with the tilt correction servo.

4.3 Star Guidance Servo

There would be little point using the tilt correction system to correct for small angular errors in the optical axis of the interferometer if the siderostats were not correctly tracking the star being observed. To track the star the siderostat must be positioned so the unit vector normal to the mirror surface is the average of two other vectors: the unit vector pointing at the star and the unit vector pointing in the direction of autocollimation. The autocollimation direction is measured before each observational run, while the position of the star is calculated using standard techniques. A mathematical model of the siderostat pointing, including several correction factors, has been developed (Thorvaldson, 1991) as a further aid in star guidance. This astrometric model is used to provide an estimate of the siderostat position as well as the velocity required to track the star every ten seconds. The tilt correction servo is used to generate an error signal for star guidance by passing the output of the tilt control computer through a low pass filter. A velocity servo was then implemented as shown diagrammatically in figure (4.10).

The frequency response of this star guidance servo should be large enough to keep the star image near the centre of the range of the tilt correction mirrors while being small enough not to interfere with the operation of the tilt correction servo. The siderostats are quite massive, so high frequency response, i.e. greater than a few hertz, is not possible. We therefore require the star guidance

servo to restrict its response to this range of frequencies. Using the techniques just developed and used on the tilt correction servo, we will now proceed to construct a linear model of the star guidance servo in order to choose suitable servo parameters.

4.3.1 Linear Model of Star Guidance System

Comparing figure (4.10) with figure (4.2) and using equation (4.26), the transfer function of the star guidance system can be written

$$T_{\text{servo1}}(s) = \frac{3T_{\text{tilt}}(s)R(s)S_1(s)S(s)}{1 + 3T_{\text{tilt}}(s)R(s)S_1(s)S(s)} \tag{4.46}$$

where $T_{\text{tilt}}(s)$ is the transfer function of the tilt correction servo, $R(s)$ is a transfer function representing a running mean, $S_1(s)$ is the transfer function of the software controlling the star guidance system, $S(s)$ is the transfer function of the siderostats themselves and the factor of three is due to the BRT. The astrometric model produces the star position used as an origin for the system and will also be responsible for generating the rotation matrices that map the tilt correction mirror axes to the axes of the siderostats. At the present, as these rotation matrices change very slowly, they are loaded manually.

Tilt Servo

The frequency response of the tilt servo is much larger than the bandwidth of the star guidance system and we therefore model it using simple gain; that is, the gain of the tilt system is assumed not to be frequency dependent at low frequencies. The stream of output numbers from the tilt control computer are normalised measurements of the angular beam position. We must therefore include the mirror calibration constant K_m in the transfer function. They are also multiplied by 2096 as this is the internal format used in the control computer. The transfer function of the tilt servo will therefore be simplified to

$$T_{\text{tilt}}(s) \simeq \frac{2096}{K_m}. \tag{4.47}$$

Running Mean

As we are interested only in the low frequency part of mirror movement, we need to pass the output of the tilt control computer through some kind of low pass

filter. This filter is implemented as a running mean of the mirror position and is performed digitally by software. However, since the sample time is much less than the time period of the running mean an analogue model may be used. The equation representing a running mean is

$$q(t) = \frac{1}{T_m} \int_{t-T_m}^{t} o_1(t)dt \tag{4.48}$$

where $q(t)$ is the output, T_m is the time period for the running mean and $o_1(t)$ is the input. This can be written as

$$q(t) = \frac{1}{T_m} \left[\int_0^t o_1(t)dt - \int_0^{t-T_m} o_1(t)dt \right] \tag{4.49}$$

which has the transfer function

$$R(s) = \frac{Q(s)}{O(s)} = \frac{1}{sT_m} \left[1 - e^{-sT_m} \right] \tag{4.50}$$

The time period was chosen to be 64 milliseconds since it is a power of two[4] multiplied by the sample time of the tilt correction system and still small enough to track the star position.

'Servo One': the Star Guidance Programme

The computer that actually performs the link between the tilt correction system and the siderostats and closes the star guidance feedback loop is called, for historic reasons, *servo one*. As in the case of the tilt servo a proportional/differential controller was chosen.

If the input stream of numbers is q_k, the output stream is v_k and the velocity produced by the astrometric model is v_{mod_k}, the equation representing 'servo one' is

$$v_k = v_{\mathrm{mod}_k} + K_1 q_{k-1} - K_2 v_{k-1}. \tag{4.51}$$

No integral term is explicitly included here as it is included in the running mean calculation. The model velocity can be considered to define the origin of the system and so we put $v_{\mathrm{mod}_k} = 0$. The $\mathcal{Z}$ transform transfer function of the system is therefore

$$S_1(z) = \frac{V(z)}{Q(z)} = \frac{K_1}{z + K_2} \tag{4.52}$$

which, by the modulation model, has the analogue equivalent

$$S_1(s) = \frac{K_1}{e^{sT_{s_1}} + K_2} \tag{4.53}$$

[4]Using a power of two means the division required for the mean calculation can be replaced by a bit shifting operation, thereby saving valuable CPU time.

where T_{s_1} is the sample time of the 'servo one' software set to be 80ms. This speed was chosen as this servo must also work with the widw field video acquisition system (Seneta, 1991) which has a set frame rate of 80ms.

Siderostat

The number resulting from the calculations described above is a velocity which, after calibration, is sent to the siderostats. The motors moving the siderostat mirrors have high torque and the movement is geared down by very large factors, so we assume a 'perfect' response from these motors. Thus if the position of the siderostat for sample k is p_k, the sample time of the siderostat is T_s and the demand velocity is v_k, the siderostat equation can be written

$$\frac{p_k - p_{k-1}}{T_s} = 2K_s v_{k-1} \tag{4.54}$$

where K_s is the calibration constant of the siderostats and the factor of two is included because a movement of the mirror results in double the movement of the star image. The $\mathcal{Z}$ transform transfer function is then

$$S(z) = \frac{P(z)}{V(z)} = \frac{2T_s K_s}{z-1} \tag{4.55}$$

with the analogue equivalent

$$S(s) = \frac{2T_s K_s}{e^{sT_s} - 1}. \tag{4.56}$$

The constant K_s is set by the siderostat electronics and is $5.3644 \times 10^{-2}\text{rads}^{-1}$ and the sample time of the system, as for 'servo one' , is $T_s = 80\text{ms}$.

4.3.2 Optimisation of Star Guidance Parameters

By combining equations (4.47), (4.50), (4.53), (4.56) and (4.46) and using equations (4.10) and (4.11) we can proceed to investigate the behaviour of the star guidance system and choose appropriate values for the servo parameters K_1 and K_2. Figure (4.11) shows examples of this calculated response for a number of values of the servo parameters and demonstrates the effect of varying each parameter. The response is required to be as flat as possible up to about 1Hz, then drop off quickly, have as small a resonant peak as possible and display a good phase response.

Based on gain response only two sets of servo parameters, $K_1 = 0.1$, $K_2 = 1.0$ and $K_1 = 1.0$, $K_2 = 0.0$, were found to be suitable, the phase responses

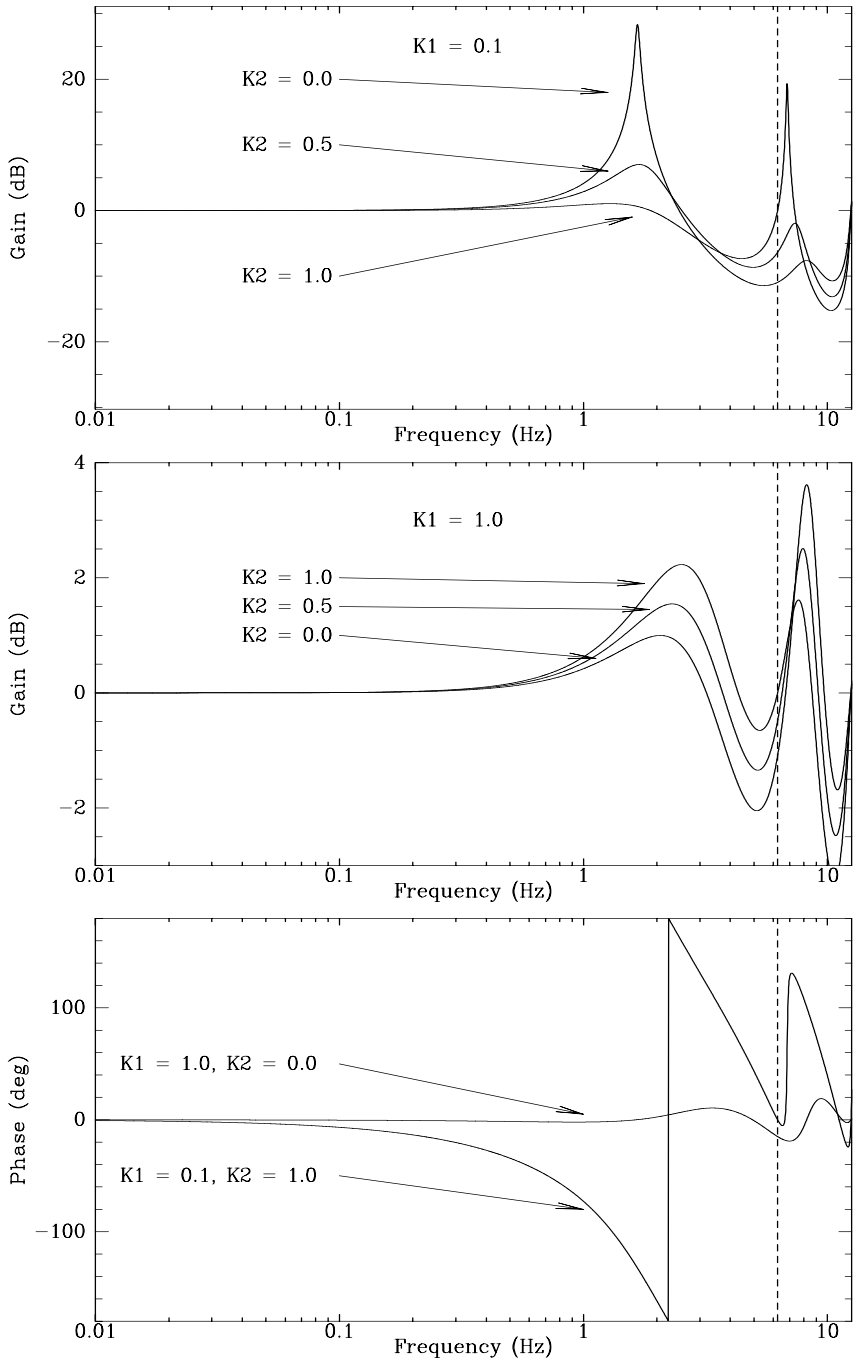

Figure 4.11: Some examples of calculated star guidance servo response. Note that as the frequency approaches the Nyquist limit of the system (Shown as dotted line) both the gain and phase behaviour are bad. As the tilt correction system is responsible for this frequency range this should present no real problem. It is also interesting to note that the effect of the damping constant K_2 reverses with increasing K_1. The plot at the bottom shows the phase responses of the system with the two 'best' sets of servo parameters. Clearly the parameters $K_1 = 1.0$ and $K_2 = 0.0$ display the best gain and phase response.

of which are also shown in figure (4.11). For the set where $K_1 = 0.1$, the phase is lagging by 45 degrees by the time the frequency reaches approximately 0.7Hz, at which point the gain is also reducing. This we define as the cutoff frequency of the star guidance servo for this set of parameters. The second set of parameters displays a much better phase response and a similar gain response. The final parameters chosen then were

$$\begin{aligned} K_1 &= 1.0 \\ K_2 &= 0.0. \end{aligned} \tag{4.57}$$

The gain of the tilt correction/siderostat servo is flat up to about 1 Hz. Any data coming out of the tilt correction servo below this frequency will not reflect the true behaviour of the wavefront tilt, because the two servos are coupled.

While tracking a star it was found that the system would 'hunt', that is oscillate around the desired position. This oscillation was found to occur whether the servo was operating in closed or open loop and is therefore probably a mechanical problem not due to the star guidance system. While this oscillation is corrected by the tilt servo and does not affect visibility measurements, it can affect data collected by the tilt servo itself (see section (5.1.2)).

4.4 Measured Performance

It remains to measure the real performance of the tilt servo to ensure it meets the original specification put forward in section (1.4). Due to time constraints on access to the interferometer the results of the analysis in the preceding sections were not available at the time when most of the measurements of servo performance had to be made. Thus the servo parameters used were not necessarily optimal. For this reason many measurements were made using a range of servo parameters, stars, sample times and aperture sizes. Stellar magnitudes ranged to magnitude 6 while sample times ranged from 1 to 30 ms. Once the linear servo model was available the servo parameters were checked against it and any measurement for which these parameters implied a resonant peak of greater than 3dB was removed from the data sample. The residual image sizes on the north and south detectors were summed and are displayed in figure (4.12). A Gaussian curve was then fitted to these data resulting in a standard deviation of 0.098 ± 0.013 arcseconds for the southern system and 0.132 ± 0.010 arcseconds for the northern system. This means that the standard deviation of the difference

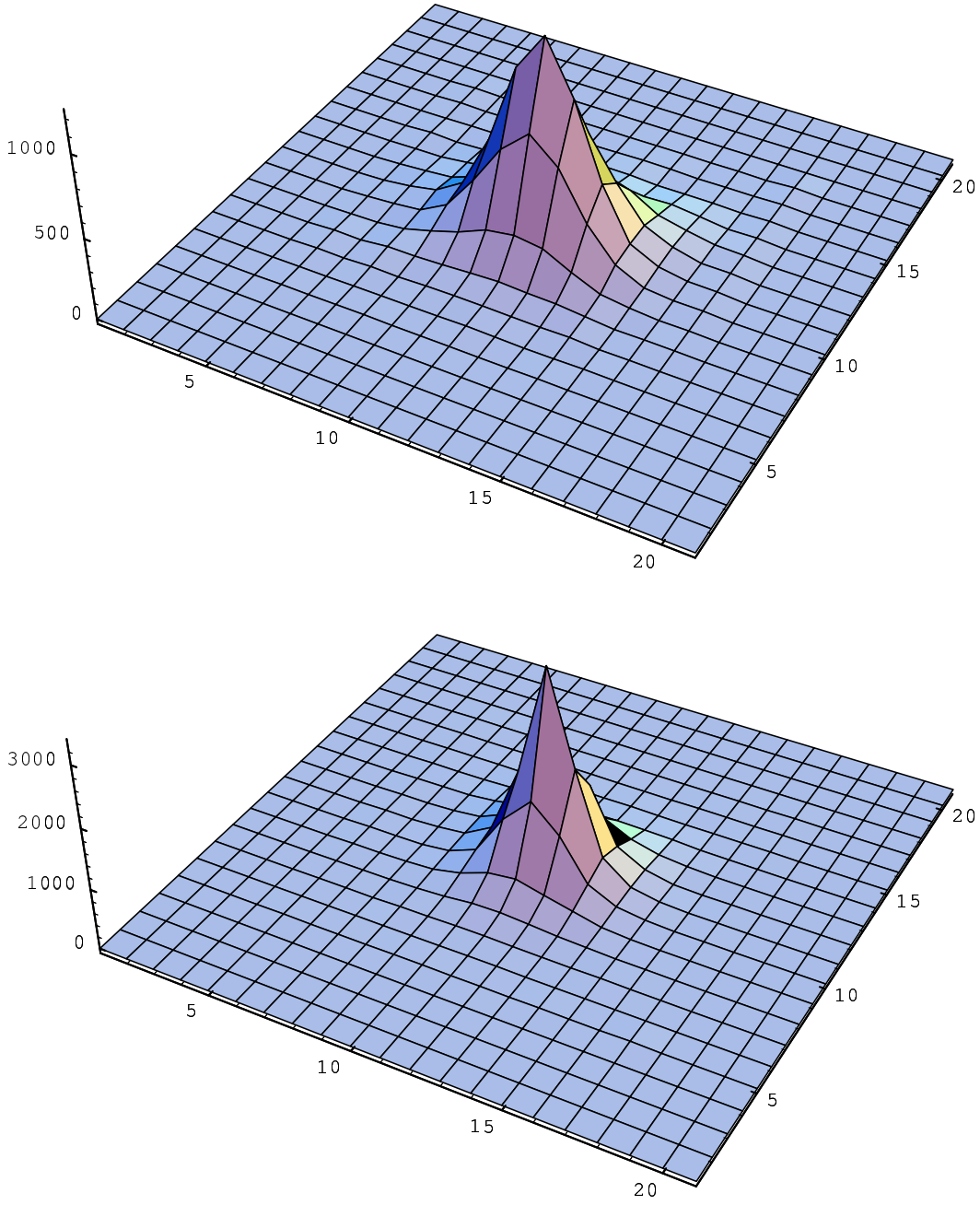

Figure 4.12: These two plots represent the residual star image size on the north (top) and south (bottom) detectors with the tilt correction servo going. The raw data used to generate these plots were taken from a sample of stars and observational sessions. Each plot displays a 1.0" by 1.0" square area, with the height of each plot representing the proportion of time spent in each area. A least squares fit of a Gaussian function to these data yields a standard deviation of 0.098 ± 0.013 arcseconds for the south system and 0.132 ± 0.010 arcseconds for the north system. The tilt correction system can therefore stabilise the star image to within approximately 0.1".

Aperture Radius on sky (cm)	Percentage Error of visibility due to residual tilt
0.9	0.1%
1.5	0.4%
2.3	0.8%
3.0	1.4%
3.8	2.3%
6.0 (Maximum)	5.7%

Table 4.5: The percentage error in visibility measurement caused by residual tilt for the range of aperture sizes currently available on SUSI. These numbers are a result of the data shown in this section and equation (1.1).

in tilt between the two beams is 0.164 ± 0.025 arcseconds. The resulting error in visibility measurement for the apertures currently available on SUSI are listed in table (4.5). Apart from the largest aperture size of 6cm, all percentage errors in this table are below 5%, showing that the tilt system to performs well within the specification set out in section (1.4). Even if the first estimates for the detector calibration constants (section (3.1.3)) are used, the system still matches the requirement specifications for most apertures. On nights of good seeing and with the largest aperture, the performance of the servo would be expected to be better than the average figure quoted above.

These experiments also provided a very good demonstration of the effect of aperture size on the performance of the tilt servo. While observing the star α Car with a sample time of 2ms the residual image motion on the south detector was measured for each possible aperture size. The results are tabulated in table (4.6) and clearly demonstrate that reducing the aperture size results in a degradation of servo performance. The reasons for this are two-fold and related to the signal to noise ratio of the detector system described in equation (3.11). By reducing the aperture size one reduces the amount of light reaching the detector, thereby reducing its signal to noise ratio. Apart from the reduction of light intensity, a smaller aperture means a larger Airy disc on the detector and therefore less detector sensitivity. This is equivalent to reducing the C_1 servo parameter and results in a reduction of servo performance. The aperture size should be the largest possible which is not much greater than the current value of Fried's coherence length r_0. Methods for determining the value of r_0 will be

Aperture Diameter (mm)	Residual Tilt Standard Deviation (arcseconds)
20	0.185 ± 0.070
25	0.158 ± 0.063
30	0.144 ± 0.044
35	0.113 ± 0.032
40	0.104 ± 0.032

Table 4.6: While observing the star α Car the residual beam tilt was measured for a range of aperture sizes. The aperture sizes quoted above refer to sizes on the optical table of the interferometer. Due to the BRT they are $\frac{1}{3}$ the size of the equivalent aperture on the sky. Clearly, the performance of the tilt servo is coupled to aperture size.

discussed in the following Chapter.

As a final demonstration of the performance of the tilt servo, refer to figure (4.13). Using the same configuration as that used for the servo analysis, a square wave was tracked in autocollimation on all four axes of the system simultaneously. A square wave signal contains many high frequency components and is an excellent test of a servo system. The results of this demonstration showed good tracking performance with a standard deviation of only 0.02". It is interesting to compare this figure with figure (8) in the paper by Clark et al. (1986), where a similar test is performed on the tilt correction device used in the Mark III interferometer. The tilt correction system described in this thesis performs at least as well, if not better, than the Mark III system, for which standard deviations no less than 0.11" are quoted at a bandwidth of 10-15 Hz.

It is difficult to compare these results with other adaptive optics systems as most are for much larger apertures and are a part of larger adaptive optics systems. A bigger aperture allows more light to reach the detector and thereby increases the signal to noise ratio. The Airy disc formed on the tilt detector will also be much smaller for large apertures, increasing angular sensitivity. Nevertheless, the tilt correction system for SUSI compares favourably to other image stabilisation systems, such as the DISCO project (Maaswinkel et al, 1987), the MARTINI device (Doel et al, 1990) and the E.S.O. adaptive optics programme (Merkle et al, 1990).

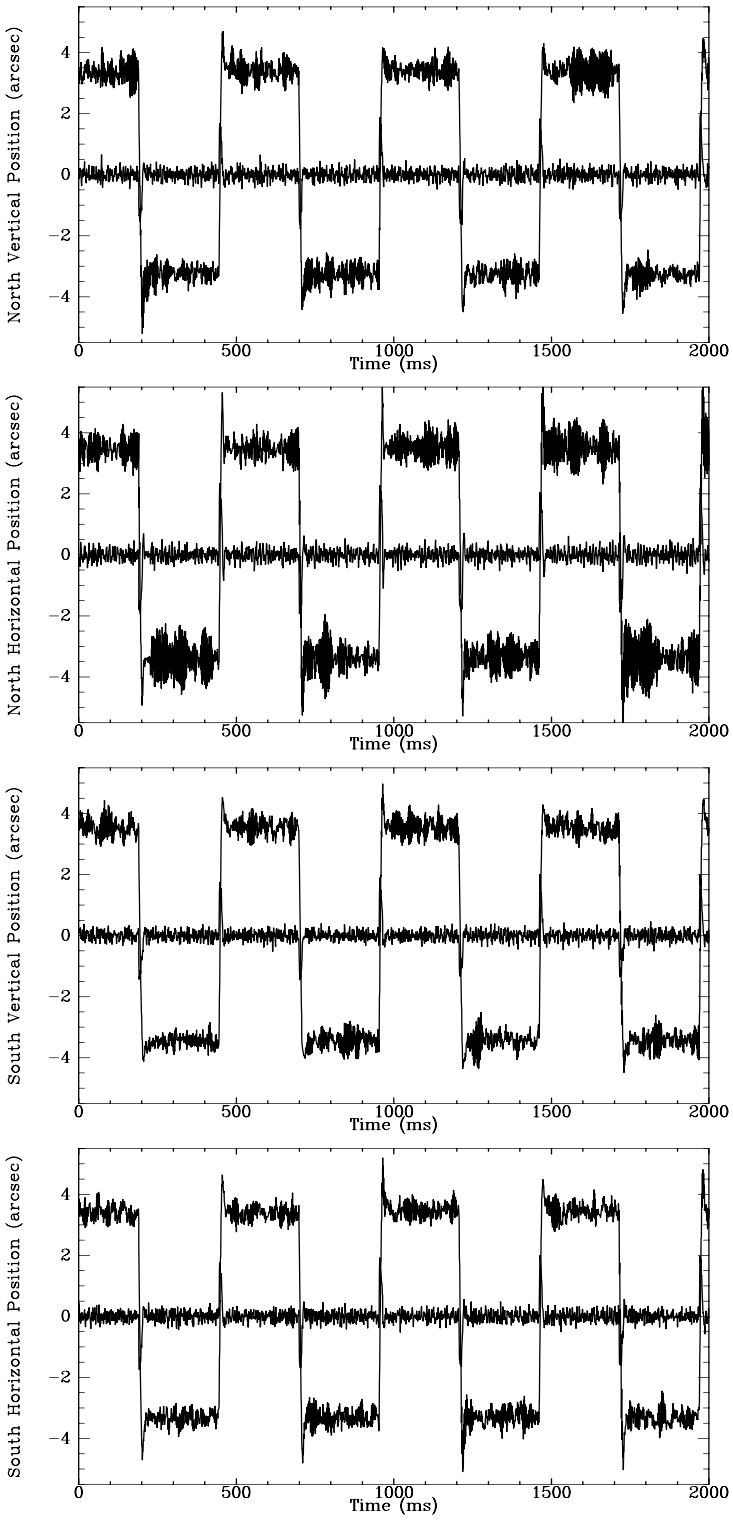

Figure 4.13: The mirror positions (large movement in each plot) and detector positions (small movement in each plot) are shown for all four axes simultaneously tracking a square wave signal with an amplitude of approximately 2.5". The residual error as measured by the detectors has an average standard deviation of 0.02" across all axes.

Chapter 5

STELLAR OBSERVATIONS

To correctly track and correct for wavefront tilt the servo must move an adaptive mirror to match the angular error of the incoming beam. With the analysis presented in the preceding chapter, showing that the system will perform this function to within 0.1", we can now go on and use the mirror position data as a measurement of wavefront tilt from which 'seeing' and the first order Zernike coefficient data are obtained.

The control software, described in section (4.2.2), will log detector and mirror positions for later processing. A spare pair of digital to analogue converters also exists in the system hardware. A combination of these and the control software allows the real time monitoring of signals internal to the control computer. These outputs can then be connected to a signal analyser to find power spectra, frequency response measurements and so on.

Measurements using both of these methods have been performed to establish a reliable seeing monitor system and to investigate the turbulence theory discussed in Chapter 2. To illustrate the kind of data collected, two examples of mirror position data are given in figure (5.1), one representing 'bad' seeing with a full width half maximum of 2.0 ± 0.1 arcseconds while the other represents average to good seeing of 0.9 ± 0.1 arcseconds. All the results and analysis to follow are derived from data such as that shown in figure (5.1), which were all collected on site at Narrabri.

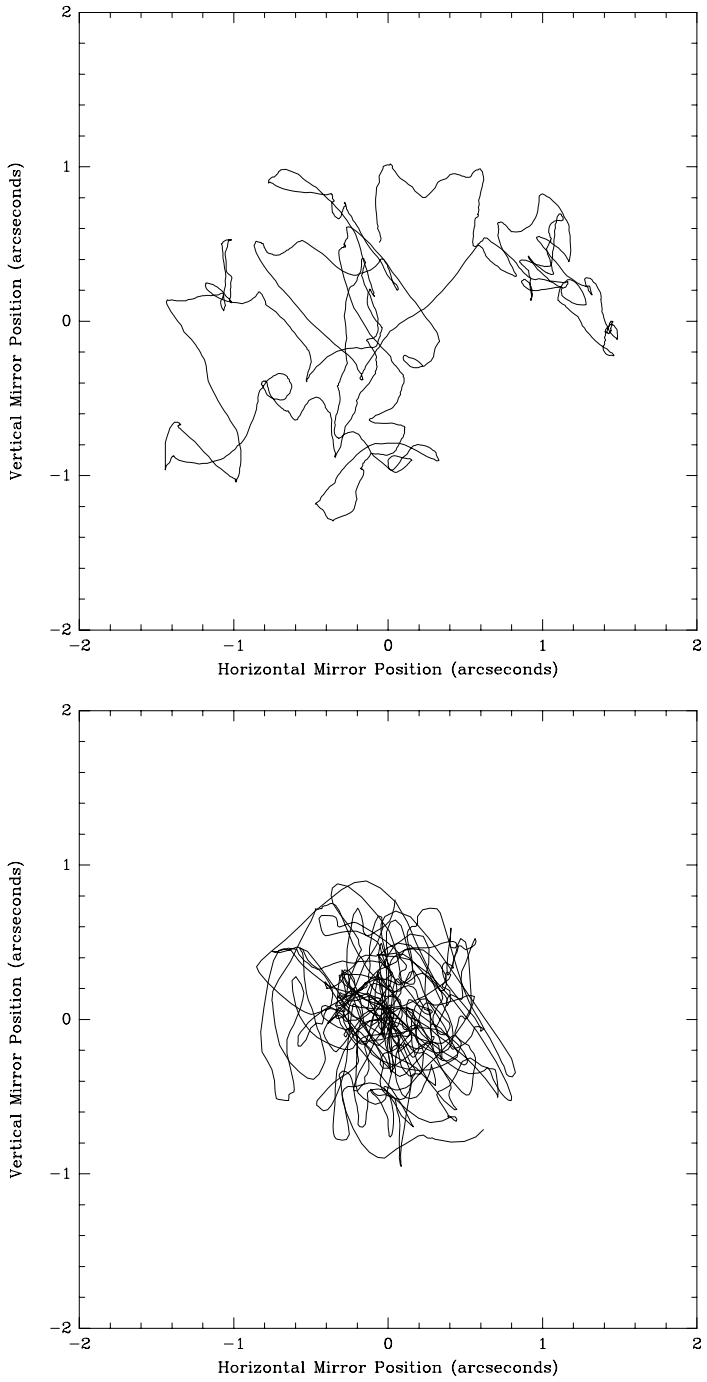

Figure 5.1: The two plots above show the mirror movement required to track a stellar image for two separate 2 second samples. The top plot is an example of 'bad' seeing conditions and corresponds to a seeing disc size of 2.0 ± 0.1 arcseconds. Note how the image moves over a large area and has a mixture of low and high spatial frequencies. As a contrast, the lower plot represents a seeing disc of only 0.9 ± 0.1 arcseconds. In this case the mirror position is more concentrated in one area.

5.1 Seeing Disc Measurements

The most common form of measurement of turbulent effects on telescopes is seeing disc size. Rather than form a diffraction-limited image in the focal plane of a telescope, the image moves about, largely as a result of the tilt of the incoming beam. Long exposures of these images form smeared-out discs whose size depends on the atmospheric conditions at the time of the measurement. A measurement of the size of this disc is a good indicator of current observational conditions.

The tilt correction servo can be used to measure seeing disc size. Using one of the spare digital to analogue converters the position of one axis of one mirror can be monitored and measured using the HP dynamic signal analyser. This produces histograms of stellar image position, two examples of which are given in figure (5.2). The fact that a Gaussian distribution fits these data so well indicates that the assumption made in Chapter 2, that the changes in the Zernike coefficients are random and distributed normally, is valid. The size of the seeing disc can be defined as the full width at half maximum of the resulting Gaussian function. A related parameter, the standard deviation of image position, can then be used along with equation (2.78) to achieve an estimate for r_0 at a given wavelength. Seeing measurements of this kind have now been automated and are a regular part of the observational programme for SUSI.

As the coherence length at the observational wavelength is of more direct relevance to the use of the tilt servo all results will be quoted in terms of the coherence length at a wavelength of 440nm. Due to the scaling of r_0 with the $\frac{6}{5}$ power of wavelength the values found were lower than those often quoted in the literature, in which a reference wavelength of 500nm is typical. Care should be taken while examining references on this subject to ensure that the wavelength is noted when accessing site performance using r_0 values. In this thesis the symbol r_0^* will be used when raw values are quoted and r_0 will be used for those values for a wavelength of 500nm.

5.1.1 Internal Stability of Enclosure

Before going on to use data collected by the tilt correction system, the level of internal seeing in the instrument enclosure should be established. If the wavefront distortion introduced into the beam inside this enclosure is of the same order as that produced by the atmosphere, any results derived from these

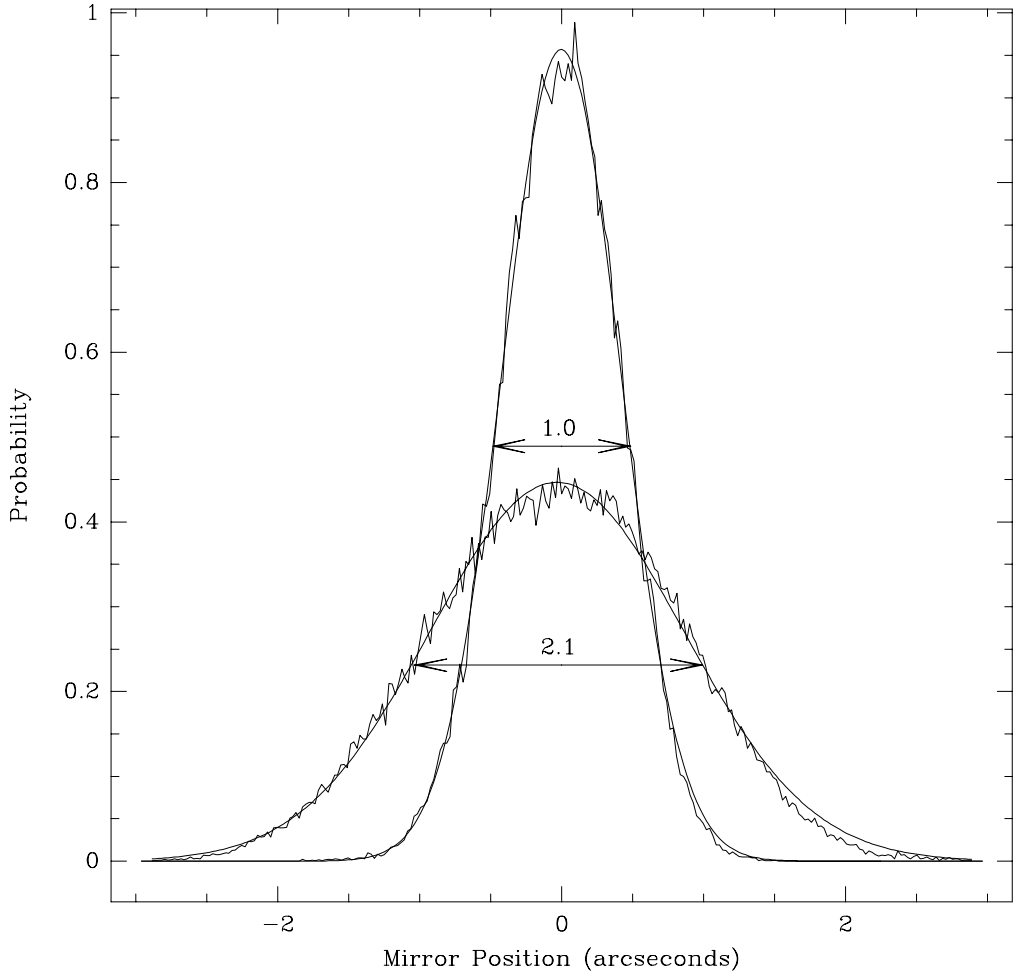

Figure 5.2: While tracking a star, a spare digital to analogue converter channel is set so it's output reflects mirror position on one axis. This signal can then be connected to a signal analyser to record the normalised histograms shown above. Two examples have been plotted, one for 'bad' and one for 'good' seeing conditions. A Gaussian curve fits these plots very well, allowing the measurement of the full width half maximum of the curves, the equivalent of a seeing disc measurement, and thereby the current coherence length via equation (2.78). These sorts of measurements are now routine and part of the normal functioning of SUSI.

measurements will have little meaning. Experience gained during the frequency response measurements required for the analysis in Chapter 4 indicated that the internal housing does not contribute a great deal to the characteristics of measured seeing. To further check this a series of tests of seeing in the instrument housing was performed by Prof. J. Davis[1].

Using only the northern beam with the reference laser as light source, an autocollimating mirror was once again placed in front of the BRT and the beam aligned with the reference quadrant detector. The tilt correction servo was then locked onto this laser beam. Since large count rates could be used because of the high intensity of the laser light, the signal to noise ratio of the detector was much greater than that when tracking a star. The precision of these measurements is therefore greater than similar measurements on stellar objects.

To ensure no external effects would interfere with the experiment all electronics, including the air conditioning, were switched off more than twelve hours prior to the measurements. Furthermore, a minimum of time was spent inside the enclosure during the optical alignment of the northern beam. All measurements quoted derive from histograms such as those shown in figure (5.2). Seeing disc size was measured for a range of conditions that might occur during an observational run of the interferometer: with the OPLC carriage stationary with its power both on and off; with the carriage moving at tracking rate and slewing rate; immediately after a long slew; after someone had walked through the internal housing; and even with a cup of hot water placed underneath the beam. The measurements are summarised in table (5.1).

These measurements show the seeing effects caused by the instrument enclosure not to be significant since the numbers quoted in table (5.1) are largely dominated by noise in the detector and servo system. The only action that did cause a measurable change in internal seeing was placing the cup of hot water underneath the beam. Conditions settled within minutes of removing the cup. As this is not likely to occur during a normal observation we conclude that any seeing caused by the internal housing is not significant. Having so concluded, we can proceed to use data from the tilt correction servo as measurements of atmospheric conditions rather than a convolution of atmospheric and instrumental effects.

[1] Unpublished internal report.

Carriage Status	OPLC Power	Seeing (arcseconds)
Stationary in centre.	Off	0.07 ± 0.03
	On	0.07 ± 0.03
Moving South at tracking rate	On	0.05 ± 0.03
Slewed back and forward 2 metres to stir air	On	0.06 ± 0.03
Power left on for 23 hours	On	0.06 ± 0.03
After walking through housing.	On	0.06 ± 0.03
Cup of hot water placed under beam.	On	0.11 ± 0.03
Five minutes after cup is removed.	On	0.05 ± 0.03

Table 5.1: A series of measurements of seeing inside the internal housing of the interferometer. It is clear that the only thing affecting the seeing enough to cause a measurable difference was the cup of hot water placed underneath the beam. As this is unlikely to occur during standard observational practice we conclude that the seeing effects in the housing are very small when compared to the atmosphere.

5.1.2 Seeing Disc Measurements at SUSI

Although a limited amount of seeing data has been gathered for the Narrabri site, enough is available for a preliminary investigation of seeing statistics. The 412 measurements of Fried's coherence length using the seeing disc size method, and corrected to equivalent zenith values[2], are summarised in figure (5.3). The data gathered so far indicate that the value of r_0 is not distributed normally and so simply calculating a mean value will not be sufficient. The mode r_0^* value was found to be $6.5 \overset{\times}{\div} 1.2\text{cm}$[3] for a wavelength of 440nm. At a wavelength of 500nm, the wavelength normally used when quoting coherence lengths for optical telescopes, this becomes $7.6 \overset{\times}{\div} 1.2\text{cm}$, corresponding to a seeing disc of 1.2 ± 0.1 seconds of arc. The median values found were $6.1 \overset{\times}{\div} 1.2\text{cm}$ for r_0^* and 1.4 ± 0.1 arcseconds for the seeing disc. As figure (5.3) shows, seeing conditions better than this are not uncommon and coherence lengths of up to $18.5 \overset{\times}{\div} 1.4\text{cm}$ have been observed.

The histogram of r_0^* measurements contains two obvious peaks. The smaller peak is probably an artifact of the measurement process and not a characteristic of the atmosphere above the site. When the star position requires the siderostat to move relatively quickly in one axis, for example in the azimuth axis when the star is near zenith, the star guidance servo causes low frequency oscillations in the tilt system. While this does not affect the visibility measurements it can cause distortions in the seeing data such as asymmetrical and double peaked curves. The data so affected has not been removed from this sample, however in future seeing data will only be collected using a channel of the tilt servo not affected by the siderostat movement. A second point to consider is that most of the data were collected during the first half of the night and consequently the sample is biased towards evening rather than early morning conditions.

The median value of r_0 measured for Narrabri can be compared to values found in other studies (which have all been converted to their equivalent values at a wavelength of 500nm). Using a shearing interferometer on the prototype site in Lindfield, Sydney, O'Byrne (1988) found a mean value of $5.5 \overset{\times}{\div} 1.7\text{cm}$, which is significantly lower. This is probably due to the fact that the data were collected on a site very close to a city. A much larger median r_0 of $10.2 \overset{\times}{\div} 1.36\text{cm}$

[2]Zenith corrections were performed using the $\cos^{\frac{3}{5}} \gamma$ relationship shown in equation (2.47) and confirmed experimentally by O'Byrne (1988) and Walters et al (1979).

[3]The errors associated with r_0 are given as a $\overset{\times}{\div}$ factor rather than the more usual $\pm$. This is because the measurement process gives an estimate for the seeing disc size which is related to r_0 via a power law. We are therefore really estimating the log of r_0 and not r_0 directly and therefore the associated errors become $\overset{\times}{\div}$ rather than $\pm$.

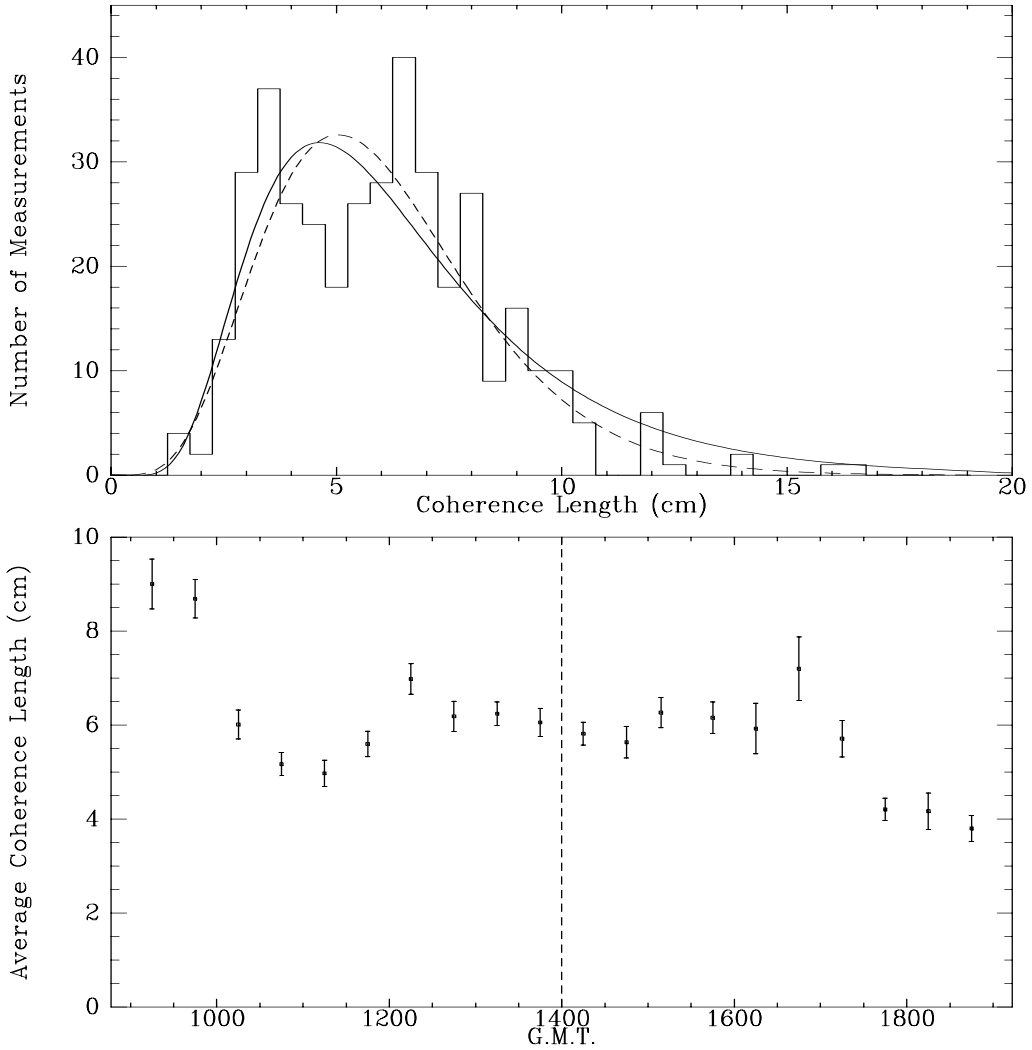

Figure 5.3: The seeing data corrected for zenith angle to date for the Narrabri site. These measurements were taken over a period of less than one year and are shown as a histogram (above) and binned into and averaged over time slots (below), where local midnight has been marked with a dashed line. It is clear that the mode coherence length is $6.5^{\times}_{\div}1.2$cm while both the mean and median values are 6.1 ± 0.6cm. This corresponds to a median seeing disc of 1.4 ± 0.1 arcseconds, a mode seeing disc of 1.2 ± 0.1 arcseconds and a coherence length of $7.6^{\times}_{\div}1.2$ arcseconds at a wavelength of 500nm. The topmost plot also shows a fit of a log/normal distribution (solid line) and a gamma distribution (dotted line).

has been observed at the Kitt Peak observatory (Fried and Mevers, 1974). This corresponds to exceptional seeing and confirms this site's good reputation. A similarly good result was found at the AMOS observatory in Hawaii, where the mean r_0 value is quoted as 9.6cm (Miller and Zieske, 1977). Walters (1981) measured a large range of r_0 values under different conditions and found median values of $8.2^{\times}_{\div}1.4$cm for mountain locations and $4.7^{\times}_{\div}1.3$cm above a desert in New Mexico. The combined results show that mean r_0 values of greater than 10cm are very unlikely except at the very best observational sites; indeed, Walters et al (1979) state that such large r_0 values are virtually non-existent. A more recent seeing study for the U.S. Naval observatory in Flagstaff, Arizona by Harris and Vrba (1992) cites a median seeing disc size of 1.3 seconds of arc, corresponding to an r_0 value of 7.6cm. The preliminary result for Narrabri, $7.6^{\times}_{\div}1.2$cm, is consistent with these other measurements. One would not expect the seeing on a flat, low altitude site to match the best mountain locations, and being far from any artificial influences it should be better than that found in the O'Byrne study.

Many of the papers cited above also discuss a log-normal probability distribution for coherence length. There is no obvious physical explanation of this distribution, except that as r_0 can never be negative a standard normal distribution could not possibly suffice. Furthermore, a log-normal distribution contains two free parameters. A statistical distribution function that may serve just as well, and which only contains one free parameter, is the gamma distribution. Figure (5.3) shows the result of fitting these two distributions to the data collected so far. A Chi squared test on these data results in less than a 0.1% probability that either fit is correct. More data is required at Narrabri before we can safely confirm or deny any such probability distribution. Data collected by the authors cited above do, however, seem to confirm a log-normal distribution, although it is likely that a gamma distribution would be just as successful. Consequently, the probability of a given value for r_0 at SUSI can be found using a gamma distribution with a mean value of

$$r_{0\text{mode}} \sim 7.1 \times \left(\frac{\lambda}{500 \times 10^{-9}}\right)^{\frac{6}{5}} \cos^{\frac{3}{5}}\gamma. \tag{5.1}$$

A more detailed analysis of site statistics should be undertaken when more data are available.

When binned and averaged over time, the data also shows that a coherence length for a wavelength of 440nm of around 6cm can be expected during most of an observational run. The graph of r_0^* with time contains data collected at different times of the year, however, due to the size of the sample, seasonal

variations have not been investigated. One obvious trend displayed in these data is that of good seeing shortly after sunset which stabilises during the night to a lower value. Just before sunrise the seeing quality improves and then decreases rapidly. This can be understood in terms of changes in the vertical temperature gradient. In the late afternoon, about an hour before sunset, the vertical temperature gradient is low and the refractive index structure constant is at a minimum (Walters and Kunkel, 1981). While this does not mean the atmosphere is not mechanically turbulent it does imply that seeing conditions will be good early in the evening. As the night progresses the air temperature falls below that of the ground causing a decrease in the vertical temperature gradient and a reduction in seeing quality. Good seeing conditions return approximately one hour before sunrise when low magnitude temperature gradients exist and last until the sun rises. At that time the air becomes very turbulent and seeing conditions deteriorate rapidly. The same general trend is evident in many other studies of this kind including Nightingale and Buscher (1991), Walters (1981), Walters et al (1979) and Miller and Zieske (1977). The paper by Harris and Vrba (1992) contains data collected over 5 years and a discussion of seasonal variations of seeing.

5.2 Power Spectrum Measurements

As discussed in section (2.3.3), measuring the full width half maximum or standard deviation of image position is equivalent to summing the total power in the tilt spectrum. If there are instrumental effects at some frequencies these will also be included in the seeing disc measurements. Since we know the star guidance servo introduces erroneous tilt at low frequencies (section (4.3)), and the servo has a finite bandwidth (section (4.2.5)), a better way to estimate r_0 may be to use only the range of frequencies for which we know the tilt servo reflects atmospheric effects.

The HP signal analyser was used to measure the power spectrum of the mirror movement in an axis of one of the tilt mirrors. Most of the power spectra data collected to date reflect the early evening seeing conditions, that is, when seeing is usually best, although some samples reflecting bad seeing were also examined.

In general the data supports the single turbulent layer Kolmogorov model discussed in Chapter 2. The values found for r_0^* and $v_\perp$ (the average perpendicular wind speed) are consistent with the seeing disc measurements in the previous

section and with other values published.

5.2.1 Basic Power Spectrum Fitting Techniques

After sampling the power spectrum of the mirror movement in one axis the results were converted into their corresponding Zernike coefficients using equation (2.59). Any data corresponding to frequencies lower than 1Hz were removed, as the star guidance servo is active at these frequencies and can cause distortions in the measurements. Data corresponding to frequencies above the maximum frequency of the current tilt servo parameters were also culled. As most of these measurements were performed on bright stars, small sample times could be used and a correspondingly large bandwidth was available.

In order to achieve an estimate of the coherence length the data was fitted, in the least squares sense, to equation (2.71) by varying r_0^* and $v_\perp$. A simple 'power law' fit could also be performed on the data to check the turbulence model. An example of data collected for the star α Car can be found in figure (5.4). Errors quoted are either due to the 0.1" uncertainty in mirror position measurement or the change required to double the r.m.s. residual error, whichever is greater.

The data in figure (5.4) once again demonstrates that turbulence theory works well at low frequencies and fails to predict atmospheric behaviour at high frequencies. The top-most plot shows that simple power laws can be used to model the spectrum. Below the 'knee' frequency the slope is very close to the predicted value of $-\frac{2}{3}$. This has also been confirmed by other studies, including those by Nightingale and Buscher (1991) and Doel et al (1990). Although no comment is made in the text in Colavita et al (1987) concerning these power laws, an analysis of figures (10) and (11) in this paper also shows good correspondence to the $-\frac{2}{3}$ power law.

At frequencies above the knee frequency the model predicts too little energy in the spectra. There exists a wide range of predictions for the high frequency behaviour, indicated by the dotted lines in figure (5.4), ranging from $-\frac{8}{3}$ (Hogge and Butts, 1976), through to the $-\frac{14}{3}$ prediction of the theory presented in Chapter 2. The only area of agreement seems to be that all Zernike coefficients should have similar high frequency behaviour. The data collected in this experiment indicate that the $-\frac{11}{3}$ power law[4] best models the high frequency

[4]Predicted by Tango and Twiss (1980), who use a different definition of tilt, and Fields (1983).

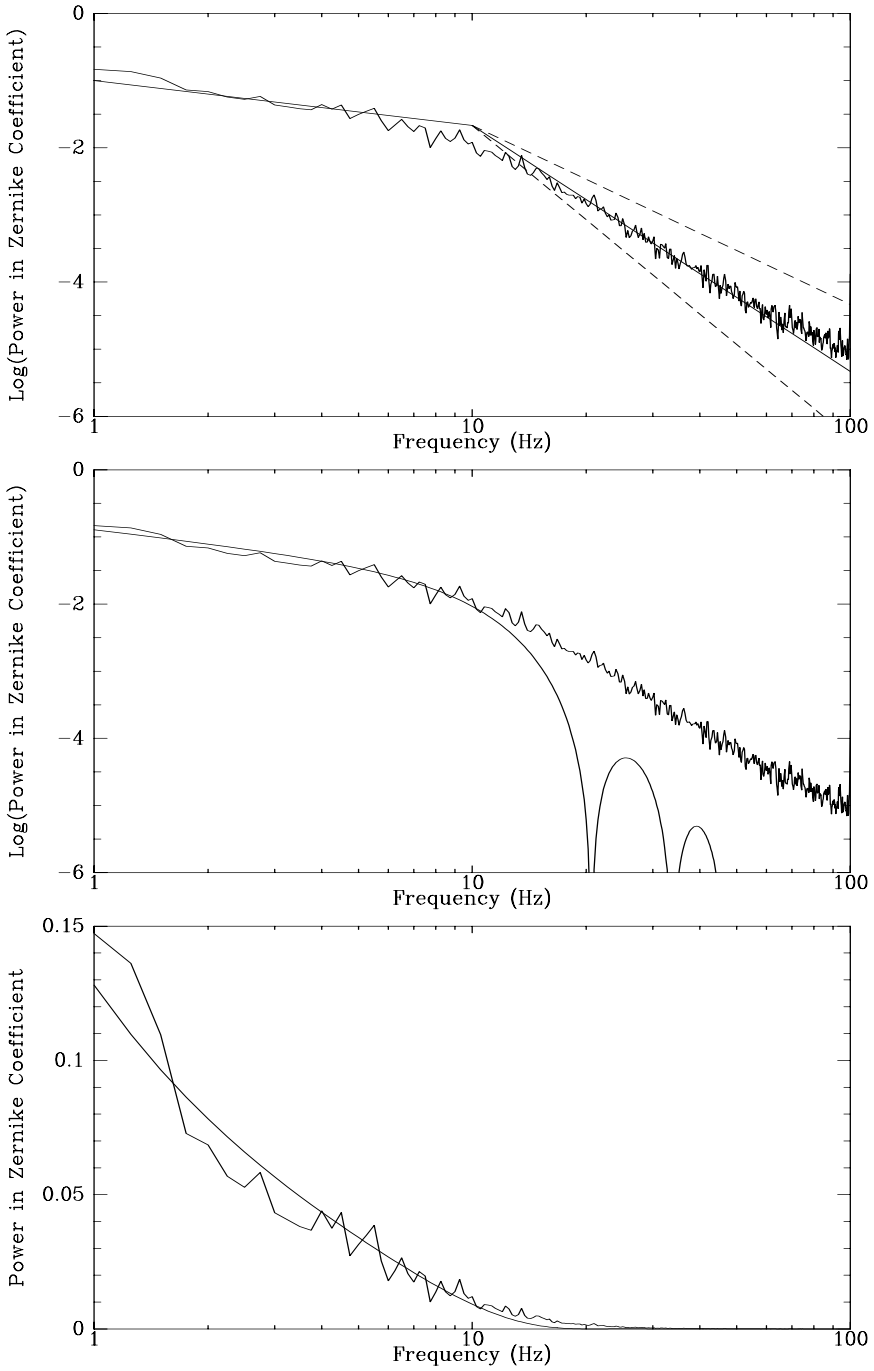

Figure 5.4: The power spectra of the $a_{2,3}$ Zernike coefficients measured for the star α Car during 'typical' seeing conditions of $r_0 = 7.6 \overset{\times}{\div} 1.2$cm at 440nm and an average perpendicular wind speed of 1.3 ± 0.2 m/s. The top-most plot shows the measured spectra along with a simple 'power law' fit. At low frequencies the $-\frac{2}{3}$ power law fits well. At higher frequencies there is some argument about the correct slope (see text); A $-\frac{8}{3}$, a $-\frac{11}{3}$ and a $-\frac{14}{3}$ slope are all displayed. Clearly the $-\frac{11}{3}$ slope fits best. The other two plots show the same data fitted to equation (2.71), displayed on log (middle) and linear (bottom) graphs. While the high frequency part has not been fitted well, the plot on a linear scale shows that, in the context of the tilt correction servo, it contains so little power that we may ignore it.

part of Zernike coefficient power spectra. Recent measurements by Acton et al (1992) also confirm the $-\frac{11}{3}$ power law for frequencies above the knee frequency. Their data also suggest a steeper slope above 150 Hz, beyond the response of SUSI's tilt servo, which they attribute to the effect of a large inner scale length.

Other measurements of high frequency tilt spectra find that the $-\frac{8}{3}$ power law is more suitable. Again, one should be careful how any particular author has defined tilt, for example, Colavita et al (1987) define tilt as the phase difference between two small apertures divided by the baseline. Other studies use apertures much larger than those in SUSI and are consequently measuring some average tilt or phase difference across the diameter of the aperture. In either case the statistics of piston phase are as important as those of tilt. It is not surprising therefore that the piston phase power law of $-\frac{8}{3}$ is found in these data sets.

The middle and lower plot in figure (5.4) show the same data along with the fitted theoretical power spectra on both logarithmic and linear scales. Once again it is clear that high frequencies are not modelled well; however, the linear plot demonstrates that so little energy is actually contained in this part of the spectra that we may ignore this problem in the context of the tilt servo. As the data to be presented in section (5.2.3) will demonstrate, estimates of coherence length using this technique yield results consistent with other seeing measurements.

While a majority of the data collected so far support the single turbulent layer Kolmogorov model, some spectra taken showed markedly different properties. Occasionally two 'knee' frequencies were apparent, indicating that two turbulent layers may be present, each with their own characteristic wind speed. At other times no knee frequency was seen, showing that the inertial subrange assumption had broken down and much more complex turbulence was present. The failure of the inertial subrange is also evident in the linear plot of the power spectrum. At low frequencies the theory predicts larger and larger amounts of energy, corresponding to an infinite outer scale length. The real data shows that the energy starts to go towards some asymptotic value for zero hertz. This low frequency asymptote has also been noted by Colavita et al (1987), who use it to estimate the size of the outer scale lengths. As the low frequency response of any system such as this must be affected by the star guidance system, these results are unreliable. They do, however, clearly demonstrate that some outer scale length of turbulence does exist.

The paper by Bester et al (1992) contains a good review of recent measurements and how they compare to the predictions of turbulence models. They

conclude that the Kolmogorov-Taylor model is a good approximation during poor seeing conditions, for very short sample times or high above the effects of the ground. At other times models such as a random walk may be more suitable. The data so far collected at Narrabri favours the Kolmogorov-Taylor model, however, as with the seeing statistics, much more data is required to definitively resolve this question.

5.2.2 Effect of Aperture on Power Spectra Measurements

All of the theory and data reduction techniques used herein contain the aperture radius explicitly. We can therefore expect the current size of aperture to have significant effects on these measurements. Not only is aperture size coupled with the calibration of these data, as shown in sections (3.1.3) and (3.1.4); it also largely determines detector calibration and servo performance. Other authors have noted the effect of aperture size on power spectrum measurements, including Nightingale and Buscher (1991) who state that the knee frequency depends on the aperture size. This is also clear from equation (2.71).

An experiment was performed to investigate the effect of aperture size on these measurements. While tracking the star α Car, once again during relatively good seeing conditions, power spectra were obtained using each of the available aperture sizes. Power spectra were then fitted, providing the estimates of r_0^*, $v_\perp$ and seeing disc size shown in table (5.2).

While seeing conditions did vary through the run, the data in this table show the knee frequency to be strongly coupled to aperture size, decreasing with increasing radius. Since the Taylor hypothesis of frozen turbulence was used to develop this model it is not surprising that smaller apertures display more high frequency energy; the 'frozen' eddies are blown past a smaller aperture faster than a larger one. The implied wind velocities and measured seeing conditions did not show any significant correlation to aperture radius. As the frequency depends inversely on aperture size, which we can change, and is proportional to wind speed, which we cannot change, the advantage of using large aperture sizes is reinforced. Not only is more light allowed to reach the detector, increasing detector signal to noise ratio and sensitivity, the required tilt servo bandwidth is reduced.

Aperture Radius (cm)	r_0 (cm)	$v_\perp$ m/s	f_{knee} Hz	FWHM Seeing Disc arcseconds
3.00	$10.6^{\times}_{\div}1.6$	1.7 ± 0.3	18.0 ± 2.2	0.9 ± 0.1
3.75	$10.5^{\times}_{\div}1.6$	2.0 ± 0.3	17.0 ± 2.2	0.9 ± 0.1
4.50	$10.3^{\times}_{\div}1.6$	2.4 ± 0.3	17.6 ± 2.2	0.8 ± 0.1
5.25	$7.8^{\times}_{\div}1.4$	2.2 ± 0.3	13.6 ± 2.2	1.0 ± 0.1
6.00	$10.2^{\times}_{\div}1.6$	2.3 ± 0.3	12.0 ± 2.2	0.8 ± 0.1

Table 5.2: The results of measurements taken over the space of approximately one hour on the same star using different aperture sizes. While the seeing did change throughout this run, the assumption that the knee frequency depends on aperture size, while seeing and wind velocity do not, is supported by these data.

	r_0 cm	$v_\perp$ m/s	f_{knee} Hz	FWHM seeing disc arcseconds
mean	$8.2^{\times}_{\div}1.2$	2.4 ± 0.3	14.6 ± 1.8	0.9 ± 0.1
mode	$7.6^{\times}_{\div}1.2$	1.4 ± 0.3	8.6 ± 2.2	0.9 ± 0.1
median	$7.8^{\times}_{\div}1.2$	1.6 ± 0.3	8.6 ± 2.0	0.9 ± 0.1

Table 5.3: While too few measurements are available for a complete statistical investigation, the mean, mode and median values of the results are shown in the table above. These results are consistent with the seeing disc size measurements made in the last section.

5.2.3 Power Spectrum Measurements at SUSI

Only some 44 power spectra samples have been collected to date, so an involved statistical analysis is inappropriate. Nevertheless, the data so far collected is consistent with similar measurements in the literature and with the seeing disc measurements presented in section (5.1). As most of the power spectra measurements were collected during the early part of the night, they favour relatively good seeing conditions. The mean, mode and median values found are presented in table (5.3). The total power in the spectrum was also calculated, to provide an estimate for the current seeing disc size. The mode value of $7.6^{\times}_{\div}1.2$ cm for coherence length is larger than was found in the survey based on seeing disc size, reflecting the bias towards good seeing in the collection process. While this

method is not as straightforward or as easily automated as measurements of the seeing disc, it should provide more reliable results as it does not include the low frequency parts affected by the star guidance system or the high frequency parts where the tilt servo starts to fail.

The range of wind speeds found in these data extended from nearly zero up to some 18m/s, with the majority lying between 2 and 10 m/s. This is in good agreement with values quoted by Nightingale and Buscher (1991) and with direct wind speed measurements on site. The largest, and probably most unphysical, values tended to match those times when Kolmogorov turbulence broke down, that is, when the power spectra did not fit the simple power laws.

While more data are required to derive more useful statistics, one fact confirmed by the measurements to date is that the majority of tilt energy lies in the low frequency part of the spectra, up to a few tens of hertz at maximum. This confirms the predictions made in section (2.3.2). Regular measurements of the tilt power spectra will be useful for choosing optimal aperture size and servo parameters. The possible response of the tilt servo is much greater than is required to track turbulence, but can always easily be reduced to match the current atmospheric conditions. A larger bandwidth may be required in future when the OPLC carriage is fully commissioned and the piezo controlled mirrors in it are operational. Movement of these mirrors will introduce small amounts of horizontal tilt which must be tracked and removed by the tilt correction system. Vibrations in the carriage itself can also introduce high frequency tilt components. It is for these reasons, apart from allowing high frequency power spectra measurements, that the tilt servo bandwidth should be increased beyond the bandwidth normally required simply to track atmospherically induced tilt.

Chapter 6

FUTURE WORK AND CONCLUSION

The major thrust of the work documented in this thesis has been to construct a wavefront tilt correction servo for use with a stellar interferometer to meet the requirement specification set out in section (1.4). The system not only exceeds these criteria, but is also capable of producing useful data for the study of atmospheric seeing and turbulence.

Before describing this system in detail, a review of basic atmospheric turbulence was undertaken in Chapter 2, where the concepts of the *inertial subrange*, *structure functions*, the *Kolmogorov Spectrum* and *single turbulent layer models* were introduced. This led to the definition of a single parameter measurement of seeing, r_0, called *Fried's coherence length*, which represents the largest diameter telescope that will be diffraction-limited at a given wavelength. In the final section of Chapter 2 a method is described for wavefront analysis using an orthogonal set of normalised polynomials defined on the unit circle, called *Zernike polynomials*. Noting the correspondence between the lower order Zernike coefficients and standard aberration terminology such as piston phase and tilt, a temporal analysis of the variation of the Zernike coefficients was performed using the *Taylor hypothesis of frozen turbulence* and Fourier analysis. A number of predictions based on this model of the power spectra for Zernike coefficients due to Kolmogorov turbulence were then investigated, including simple power law relationships, the relationship between seeing disc size and r_0, the total power in the tilt spectrum and spectra bandwidths. This new formulation of Zernike coefficient power spectra was shown to correspond well to previous models in the literature while offering simpler calculation methods. The model was also shown to fit experimental results obtained using the tilt servo.

The hardware and software developed for the tilt tracking system were described in Chapter 3. The detectors used are *optical pyramids*, a form of quadrant detector with high quantum efficiency and small dead zones due to its use of the *knife edge* criterion. A noise analysis and rough calibration was also presented to show that these detectors could achieve the precision and linearity required for the tilt servo. The mirrors are flat mirrors mounted on three piezo electric actuators and were calibrated using interferometric techniques.

With the hardware constructed, calibrated and mounted, along with the theoretical understanding of the behaviour of wavefront tilt due to atmospheric turbulence, an analysis of servo behaviour and performance was undertaken in Chapter 4. Using *Laplace transforms*, $\mathcal{Z}$ *transforms* and *transfer functions* a model of the servo system was constructed and fitted to experimental data. This showed that the bandwidths predicted by the atmospheric model could easily be accommodated by the tilt servo. Further experimental results demonstrated that the servo performs well within the tolerances specified. The residual tilt in the beams after passing through the tilt correction system (that is about 0.1") should contribute no more than 2% error to the visibility measurements made by SUSI for all but the largest aperture sizes available.

Having described the servo system and demonstrated that it more than meets its design criteria, some preliminary results based on data collected while tracking stellar objects were presented in Chapter 5. A small sample of seeing disc measurements was analysed, yielding a median r_0 value of $7.1^{\times}_{\div}1.3$cm at 440nm for the Narrabri site, a value consistent with similar seeing studies at other observatories. Tilt spectra were also measured and compared to the theoretical predictions in Chapter 2. While the theory fails at high frequencies, excellent correspondence was found amongst the low frequencies, the component that contains a majority of the power in the spectrum.

6.1 Hardware Improvements

Even though the tilt servo performs within specification, a number of areas remain in which the hardware could be improved. The first, and probably most important, of these is the area of quantum efficiency. As discussed in section (3.3.1), the number of photons registered in each cycle is an order of magnitude less than the predicted value for both the visibility and wavefront tilt detectors. As both of these systems display this behaviour we must assume that this is a problem of telescope throughput rather than detector quantum efficiency. It is

very likely that the old and faulty surfaces of the tilt correction mirrors are responsible for a large part of the losses. In future these mirrors should be replaced with one of the more modern tip/tilt mirrors now available. This would have the added advantage of incorporating piezos with hysteresis correction which, while probably not improving the bandwidth, would improve the phase response of the entire system. Experiments are planned to determine where losses are taking place within SUSI by using the reference laser and measuring light intensities at different points along the optical chain.

As well as replacing the mirrors themselves, the mounts used and mounting position can also be improved. Adding micrometer adjusters to the mount to enable the fine positioning of the mirrors' central position would significantly aid in interferometer adjustment. It would also be of benefit to move the mirrors themselves to a position immediately after the BRT. In this way the alignment of the central position would be less critical and this would mean that the beams are tilt corrected as early in the optical path as possible. This was where these mirrors were originally intended to go. Unfortunately, however, the size of the mirrors meant that they interfered with the OPLC carriage.

Performance improvements are also possible with minor changes to other parts of the system. The polarising cubes on the optical table can create multiple images of the reference pin hole during optical alignment, forcing us to purposefully misalign these cubes (refer to Appendix A). Replacing these cubes with standard beam splitters or some other device could solve this problem and simplify many alignment procedures. Many software additions are also possible, principally the automation of servo tuning and alignment of both beams to the reference detector.

6.2 Future Work

Due to time constraints on the interferometer and research time for this thesis there remain a number of areas in which more work would be advantageous. These can be broken up into theoretical and experiment areas as set out below.

6.2.1 Theoretical Investigation

The power spectra analysis presented in Chapter 2, while providing simple and useful expressions for Zernike coefficient temporal power spectra, fails at very

low and high frequencies. This is a result of the simplifying assumptions made in order to achieve these results, primarily those of the inertial subrange and Taylor's hypothesis. The theory predicts infinite energy at zero hertz in the low order power spectra. This is because we have let the outer scale length approach infinity. At high frequencies the Taylor hypothesis breaks down, as the smallest eddies will not remain 'frozen' as they pass by the aperture. While other authors, including Colavita et al (1987), have investigated these effects, a reformulation of these ideas in the mathematical framework of the theory in section (2.3) would perhaps produce a model that is easier to apply directly to adaptive optical systems.

One way of adapting these power spectra models would be to use more complex expressions for the spatial power spectrum of refractive index changes. Since the Kolmogorov model used in this thesis produced more than adequate results for the production of the tilt correction servo and data analysis, a more complex model was not investigated. Turbulence models including finite inner and outer scale lengths and multiple turbulent layers (for example McKechnie (a) (1991), McKechnie (b) (1991) and Andrews (1992)) would improve the predictive power of this theory. As pointed out in section (2.3.2), any suitable expression could be used and the same method followed to achieve a solution.

6.2.2 Experimental Investigation

More long term seeing data, using either of the methods described in Chapter 5, will be collected as part of the normal observational routine of the interferometer. When a large amount of such data have been acquired, over at least one full year of regular observation, a more detailed statistical analysis of seeing at the Narrabri site should be undertaken. Understanding the characteristics of the site will aid in preparing observational schedules and planning individual runs.

Along with the standard measurements of seeing disc, more data concerning the temporal power spectra of wavefront aberrations would aid in the theoretical work outlined above. More power spectra measurements, including piston phase, will help test these models as well as provide r_0 and $v_\perp$, and perhaps L_0 and l_0, estimates which can be compared to more direct measurements of wind speed and current seeing disc size.

Due to limited access to the interferometer, it was not possible to measure the affect of wavefront tilt on the visibility measurements obtained by SUSI directly. When SUSI is fully operational, experiments should be performed to

estimate the effect of changing tilt servo bandwidth, including servo parameter and sample time changes, on visibility. An empirical confirmation of equation (1.1) would also be of benefit.

6.3 Conclusion

Even with the limitations of the theoretical model and the hardware problems discussed above, it is clear that the wavefront tilt correction servo described in this thesis meets, and even exceeds, the design criteria set out in Chapter 1. The theoretical methodology developed in Chapter 2 is flexible and easily applied to empirical data and, while at present implemented using simple Kolmogorov spectra, is open to any model of spatial refractive index statistics at ground level.

The servo has performed well in good and bad seeing, has been used to track stars of up to magnitude 6.5 and is predicted to reach magnitudes of up to 8.5. This performance compares favourably with other similar systems. The device was also shown to be capable of producing data for use in simple seeing studies and more complex investigations of turbulence theory. So, not only is the system capable of tracking a stellar image to within 0.1" at bandwidths of up to 70 Hz, aid in star guidance and optical alignment of the interferometer; it also produces data useful for studying seeing and testing predictions of atmospheric turbulence theory.

The methods used to analyse and build this device, most notably in the areas of turbulence theory, the design of the quadrant detectors, the control algorithm and the servo model, have immediate application for other existing and proposed adaptive optics systems, not only in stellar interferometers, but in all types of modern astronomical telescopes.

Appendix A

Optical Pyramid Alignment

The optical arrangement used to align the detectors is shown in figure (A.1). Note that a number of flats between the aperture and the tilt mirror are left out of this diagram. The 140m of optical path at this point includes the optical path length compensator (OPLC). This is necessary due to the placement of the tilt mirrors on the piers at the ends of the OPLC. While the long path length through air does introduce some beam distortion due to turbulence inside the enclosure, it also increases the precision of autocollimation adjustment. This setup allows two methods of looking at the beam. The theodolite is focussed on the image plane of the pinhole in the spatial filter, while the CCD will either display an image of the aperture plane or the pin hole, depending on the position of the lens in front of it.

Before alignment of the detectors it is necessary to ensure that the polarising cube, the autocollimating flat and the theodolite are in the correct positions. With the cube removed the autocollimating flat should be placed into the beam. By monitoring the aperture plane with the CCD this mirror can be adjusted until the reflected beam is superimposed onto the image of the aperture. The aperture size used originally was 35mm imaged across approximately 400 pixels of the CCD. Assuming superimposition of these images to within 10 pixels, the very long optical path length of 140m then means that the flat mirror will be autocollimating to within approximately one arcsecond. The lens in front of the CCD should then be moved so an image of the pinhole can be seen on the monitor screen.

Now that the reference beam is properly autocollimating the polarising cube can be put onto the table. Using the three vertical mounting screws under the cube an iterative approach must be used to ensure that it is aligned properly.

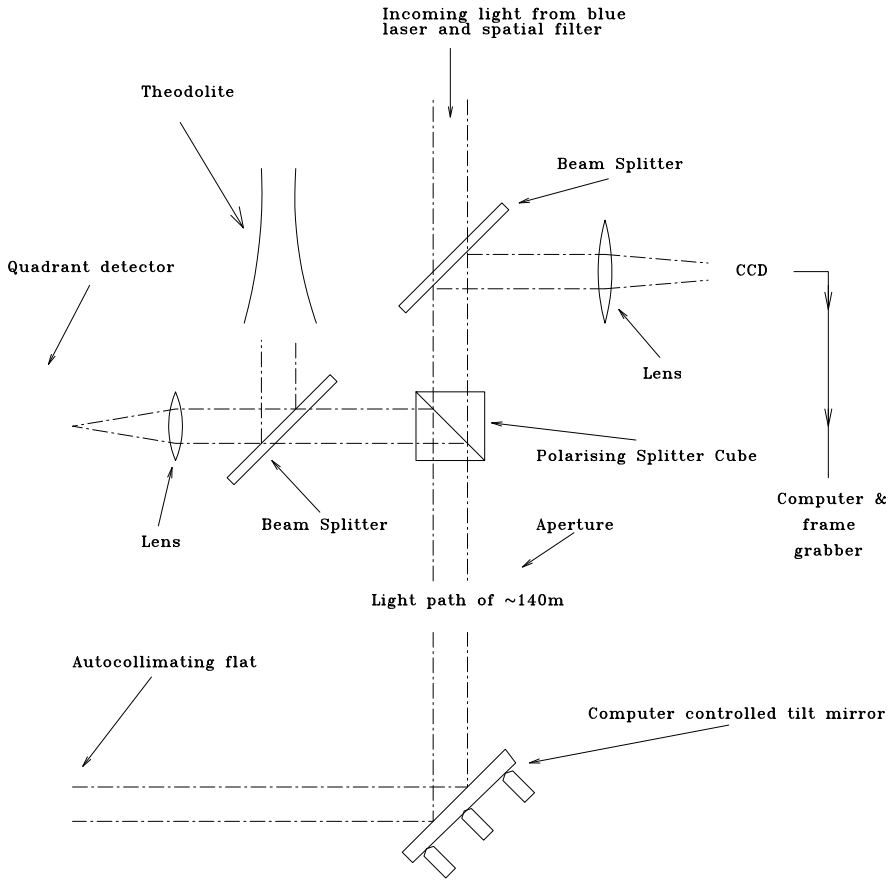

Figure A.1: The optical layout used to adjust the optical pyramids. The incoming light source has been passed through an optical spatial filter and is the same reference beam used to align all the optics of the interferometer. The extra light path of 140m includes the optical path length compensator. The beam is folded a number of times (not shown above) and some flats have been left out of the diagram. The CCD allows inspection of the pinhole image or the aperture plane while the theodolite is focussed on the pinhole image plane.

The two steps are:

1. Adjust the vertical face until the reflection from the side facing the spatial filter and pinhole is correctly autocollimating. The CCD image can be used to check this.

2. Ensure that the beam going out to the quadrant detector is parallel to the optical table surface. This can be done using a height gauge.

Repeat these two steps until both criteria are satisfied.

Two problems were encountered using these cubes. The reflection from the side of the cube facing the spatial filter can cause confusion during alignment. The cube was therefore rotated so that this reflected beam was offset slightly with respect to the laser beam. In this way it is possible to distinguish between the very bright image due to the autocollimating flat and the faint spot due to the cube surface. This slight misalignment of the cube does not affect the image quality, although it may shift the beam slightly to one side as the two faces of the cube are parallel. This should have no bearing on the operation of the tilt system or the interferometer as a whole. Secondly, when the reference laser is sent through the cube an extra beam is reflected onto the detectors via the splitting surface from the face of the cube opposite the detector. This extra beam was removed by placing a dispersive gel (petroleum jelly) on the outside of this face. Thus the beam hitting this surface is dispersed rather than reflected.

Once the cube is installed and properly aligned the theodolite has to be positioned and centred on the pinhole. Place another flat mirror in the position of the quadrant detector and remove the lens from in front and adjust it until it is autocollimating. With the CCD still focused on the pinhole, multiple images can be seen if the second flat mirror is not in the correct position. These extra images are due to the fact that a light path exists via the cube such that the two flat mirrors face one another. The second flat should be adjusted until only one image of the pinhole is present on the CCD display. The theodolite can now be put in place and set so that the cross hairs are centred on the image of the pinhole. Note that you should *always* place neutral density filters into the beam *before* looking through the theodolite. These cross hairs become the reference position for all further alignment. At this point the alignment optics are ready, and the alignment of the detectors themselves can commence.

The first stage of detector adjustment is to ensure that the horizontal knife edge is parallel to the optical table and that the front face of the prism

containing the horizontal edge is correctly autocollimating. Illuminate the detector from behind using a diffuse light source and remove the lens and vertical edge assembly from the detector table. Using a microscope on a sliding assembly set at the correct height of 182mm, view the horizontal edge through the two input holes at the front of the box containing the horizontal prism. The two adjustment screws at the rear of the levelling table can be used to set the horizontal edge at the cross-hairs of the microscope on both sides. With the diffuse light source and the microscope removed, place the detector onto the table with the central front input hole in the centre of the collimated beam. While looking through the theodolite, centre the reflected light from the prism onto the cross hairs by

1. rotating the detector bodily,
2. using the microcontrol screw on the front of the detector assembly to tilt the prism.

These steps must be repeated until the horizontal edge is at the correct height, parallel to the optical table, and the front surface is autocollimating. The entire assembly should then be clamped onto the table.

Stage two of detector alignment is to place the vertical edge assembly into position and ensure that the vertical edge is imaged onto the horizontal edge and the prism containing the vertical edge is autocollimating. Once again a two step iterative procedure is used. The first step is to focus the microscope onto the horizontal edge through one of the four output holes at the back of the detector with the diffuse light source at the front of the detector. The vertical edge assembly can slide backwards and forwards. Move the vertical edge assembly until the vertical edge is also in focus. The next step is to twist the vertical edge assembly while observing the image in the theodolite, until the prism is autocollimating in azimuth. If the elevation is incorrect the vertical assembly can be levelled using the three adjustment screws on the mounting frame. These steps must be repeated until the two edges, as viewed from the rear of the detector, are sharply in focus with both prisms autocollimating.

A final adjustment of the vertical edge prism is required to ensure that the optical axes of the two small lenses connected to the rear of the assembly block are on axis in a vertical direction and that the vertical edge is perpendicular to the horizontal edge. The microscope cross hairs should be set to the same height used while adjusting the horizontal edge. View the two detector edges from the front while back-lighting the pyramid with the diffuse light source. Two possible

problems can be found in this manner. Firstly, the horizontal edge can appear to be at the wrong height. This is caused by the lenses being off-axis in the vertical direction. The three adjustment screws on the vertical assembly can be used to correct this error. Secondly, the horizontal edge may appear to be discontinuous through the vertical edge. This error is due to a tilt of the vertical prism and is also corrected by using the three adjustment screws on the vertical edge assembly. Once again these steps are repeated until the horizontal edge appears at the correct position and is continuous through the vertical edge and the vertical edge prism remains correctly autocollimated.

The last remaining step in detector alignment is to put into place the lens that images the star onto the vertical edge. Care must be taken to ensure that the collimated beam goes through the centre of this lens and that the lens is not tilted with respect to the beam. Place the lens roughly in the correct position and, using the micrometer slides, move the detector until all the light is going through one quadrant. Use the microscope to view the two edges through the output hole for this quadrant and focus it onto the two edges. Adjust the lens to give a sharply focussed image. As a final check the detector assembly can be moved around to ensure that the image is rapidly extinguished as the edge is moved across it.

This entire procedure was performed on all three detectors. In the case of the reference detector care was taken to centre the pyramid on the image. This detector was never moved again and became the position reference for the entire interferometer.

Appendix B

Circuit Diagrams

All circuit diagrams for the electronics of the system are presented below except for those of the power supplies. The VH to XYZ conversion and high voltage amplifiers were designed by Stephen Owens and came directly from the prototype interferometer. The preamplifier circuit comes from the Radio Shack data sheet (Radio Shack, 1988). The rest of the circuits were designed by the author with the aid of Stephen Owens. The address decoding section is for use with the AV68000 computer used in the system manufactured by Interrupt Systems, Melbourne Australia. All diagrams were drawn using the 'Protel' software suite. After the circuit diagrams there follows a tabulation of connecters used. Refer to figure (3.13) for a schematic representation of how the components fit together.

Read Address (HEX)	Device	Write Address (HEX)	Device
420000	Counter 0	420020	DAC 0
420002	Counter 1	420022	DAC 1
420004	Counter 2	420024	DAC 2
420006	Counter 3	420026	DAC 3
420008	Counter 4	420028	DAC 4
42000A	Counter 5	42002A	DAC 5
42000C	Counter 6		
42000E	Counter 7		
420010	Counter 8		
420012	Counter 9		
420014	Counter 10		
420016	Counter 11		

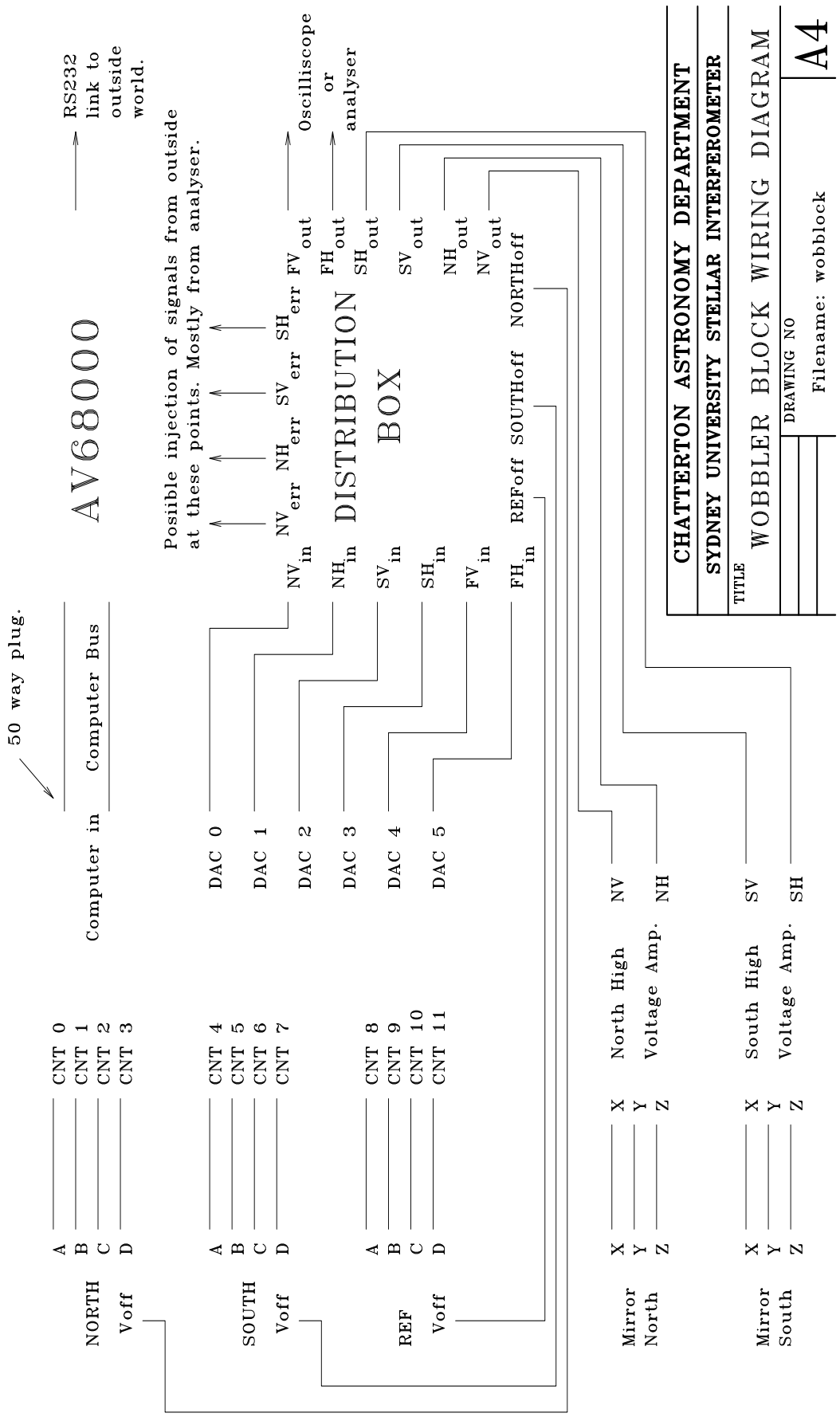
50 way plug.
Computer in
Computer Bus
AV68000
RS232 link to outside world.
Posiible injection of signals from outside at these points. Mostly from analyser.
NORTH
Voff
SOUTH
Voff
REF
Voff
Mirror North
Mirror South
A CNT 0
B CNT 1
C CNT 2
D CNT 3
A CNT 4
B CNT 5
C CNT 6
D CNT 7
A CNT 8
B CNT 9
C CNT 10
D CNT 11
X North High NV
Y Voltage Amp. NH
Z
X South High SV
Y Voltage Amp. SH
Z
DAC 0
DAC 1
DAC 2
DAC 3
DAC 4
DAC 5
NV_in
NH_in
SV_in
SH_in
FV_in
FH_in
NV_err
NH_err
SV_err
SH_err
FV_out
FH_out
SH_out
SV_out
NH_out
NV_out
REFoff
SOUTHoff
NORTHoff
DISTRIBUTION BOX
Oscilliscope or analyser
CHATTERTON ASTRONOMY DEPARTMENT
SYDNEY UNIVERSITY STELLAR INTERFEROMETER
TITLE
WOBBLER BLOCK WIRING DIAGRAM
DRAWING NO
Filename: wobblock
A4

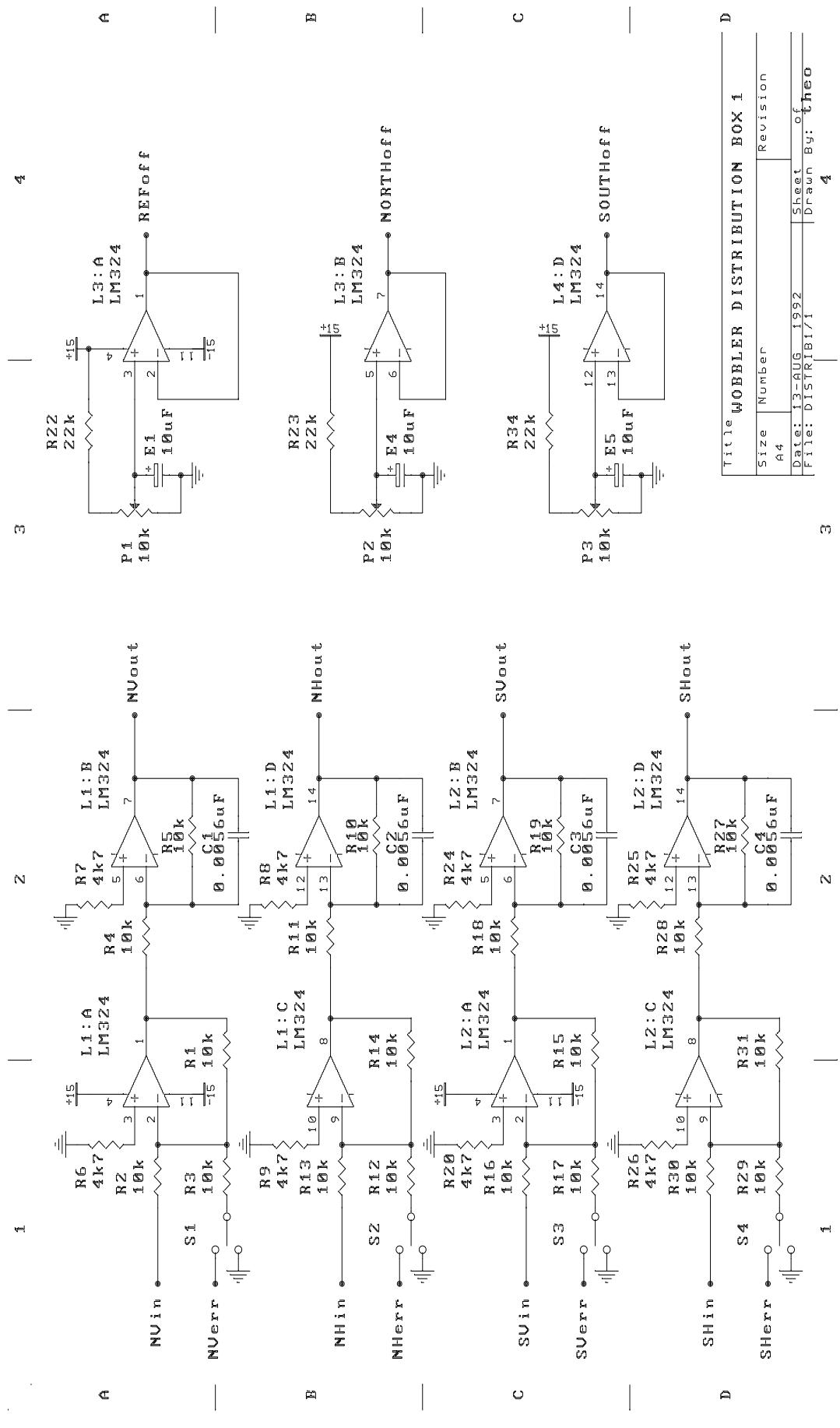
L3:A
LM324
REFoff
R22
22k
E1
10uF
P1
10k
L3:B
LM324
NORTHoff
R23
22k
E4
10uF
P2
10k
L4:D
LM324
SOUTHoff
R34
22k
E5
10uF
P3
10k
WOBBLER DISTRIBUTION BOX 1
Size
A4
Number
Revision
Date: 13-AUG 1992
File: DISTRIB1/1
Sheet of
Drawn By: theo
L1:A
LM324
L1:B
LM324
L1:C
LM324
L1:D
LM324
L2:A
LM324
L2:B
LM324
L2:C
LM324
L2:D
LM324
NVout
NHout
SVout
SHout
NVin
NVerr
NHin
NHerr
SVin
SVerr
SHin
SHerr
S1
S2
S3
S4
R1 10k
R2 10k
R3 10k
R4 10k
R5 10k
R6 4k7
R7 4k7
R8 4k7
R9 4k7
R10 10k
R11 10k
R12 10k
R13 10k
R14 10k
R15 10k
R16 10k
R17 10k
R18 10k
R19 10k
R20 4k7
R24 4k7
R25 4k7
R26 4k7
R27 10k
R28 10k
R29 10k
R30 10k
R31 10k
C1 0.0056uF
C2 0.0056uF
C3 0.0056uF
C4 0.0056uF

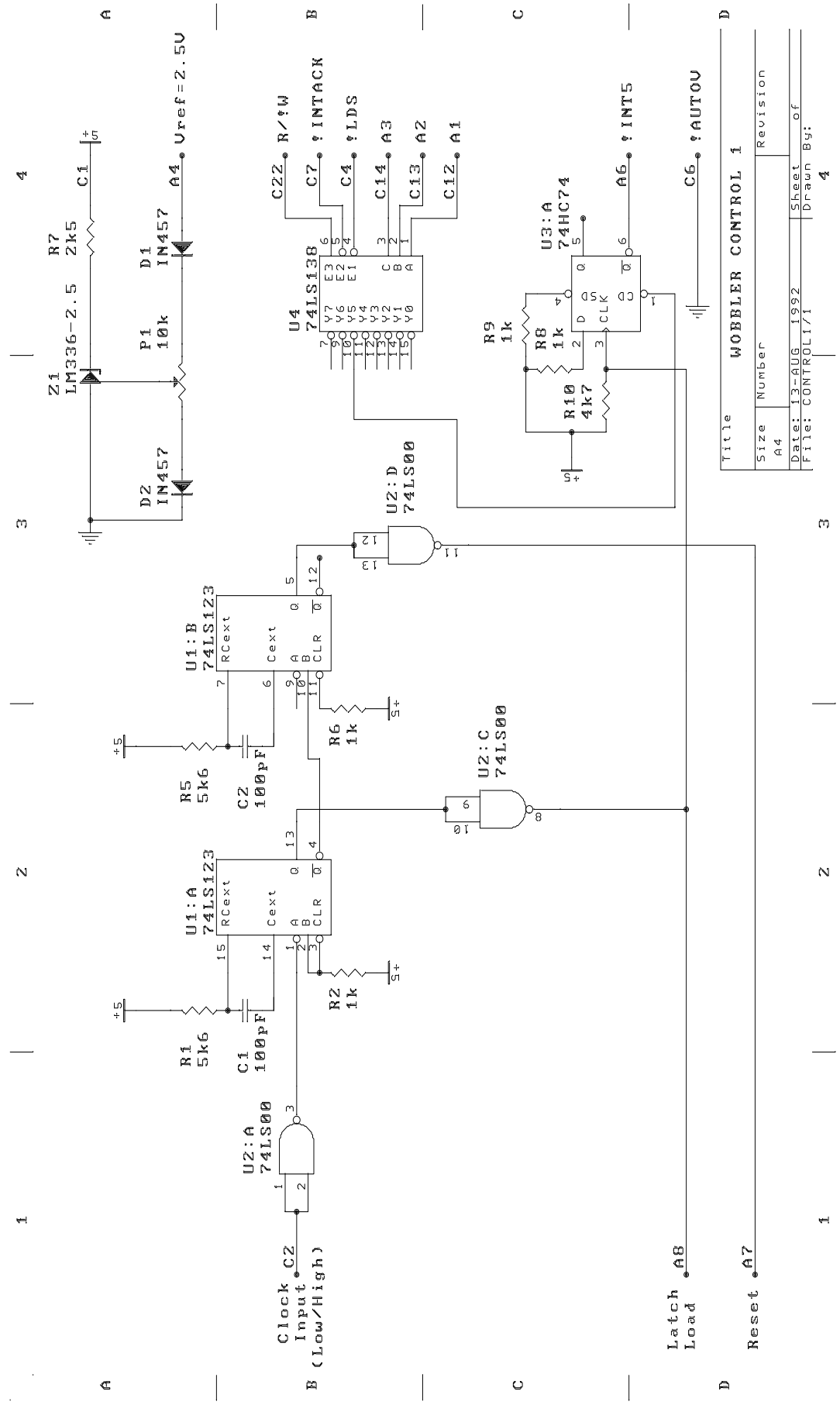
WOBBLER CONTROL 1
Title
Number
Revision
Size A4
Date: 13-AUG 1992
Sheet of
File: CONTROL1/1
Drawn By:
Z1 LM336-2.5
R7 2k5
P1 10k
D1 IN457
D2 IN457
Vref=2.5V
C1
U4 74LS138
C22 R/!W
C7 !INTACK
C4 !LDS
C14 A3
C13 A2
C12 A1
U3:A 74HC74
R8 1k
R9 1k
R10 4k7
A6 !INT5
C6 !AUTOV
U2:D 74LS00
U1:B 74LS123
R6 1k
C2 100pF
R5 5k6
U2:C 74LS00
U1:A 74LS123
R2 1k
C1 100pF
R1 5k6
U2:A 74LS00
Clock Input (Low/High)
C2
Latch Load
A8
Reset
A7

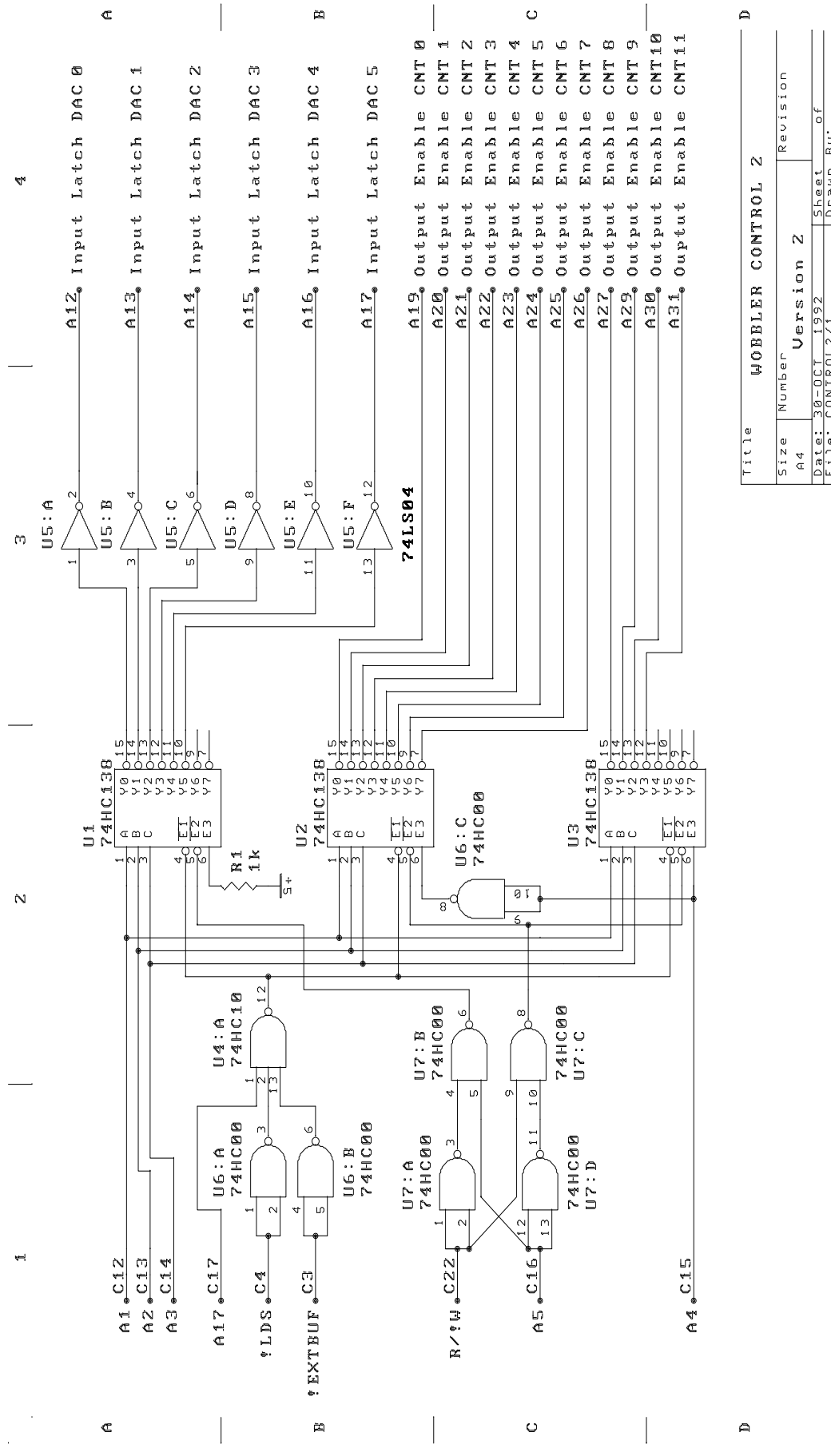
A12 Input Latch DAC 0
A13 Input Latch DAC 1
A14 Input Latch DAC 2
A15 Input Latch DAC 3
A16 Input Latch DAC 4
A17 Input Latch DAC 5
A19 Output Enable CNT 0
A20 Output Enable CNT 1
A21 Output Enable CNT 2
A22 Output Enable CNT 3
A23 Output Enable CNT 4
A24 Output Enable CNT 5
A25 Output Enable CNT 6
A26 Output Enable CNT 7
A27 Output Enable CNT 8
A29 Output Enable CNT 9
A30 Output Enable CNT10
A31 Ouptut Enable CNT11
U5:A
U5:B
U5:C
U5:D
U5:E
U5:F
74LS04
U1 74HC138
U2 74HC138
U3 74HC138
R1 1k
+5
U6:C 74HC00
U4:A 74HC10
U6:A 74HC00
U6:B 74HC00
U7:A 74HC00
U7:B 74HC00
U7:C 74HC00
U7:D 74HC00
A1 C12
A2 C13
A3 C14
A17 C17
!LDS C4
!EXTBUF C3
R/!W C22
A5 C16
A4 C15
Title WOBBLER CONTROL 2
Size A4
Number Version 2
Revision
Date: 30-OCT 1992
Sheet of
File: CONTROL2/1
Drawn By:

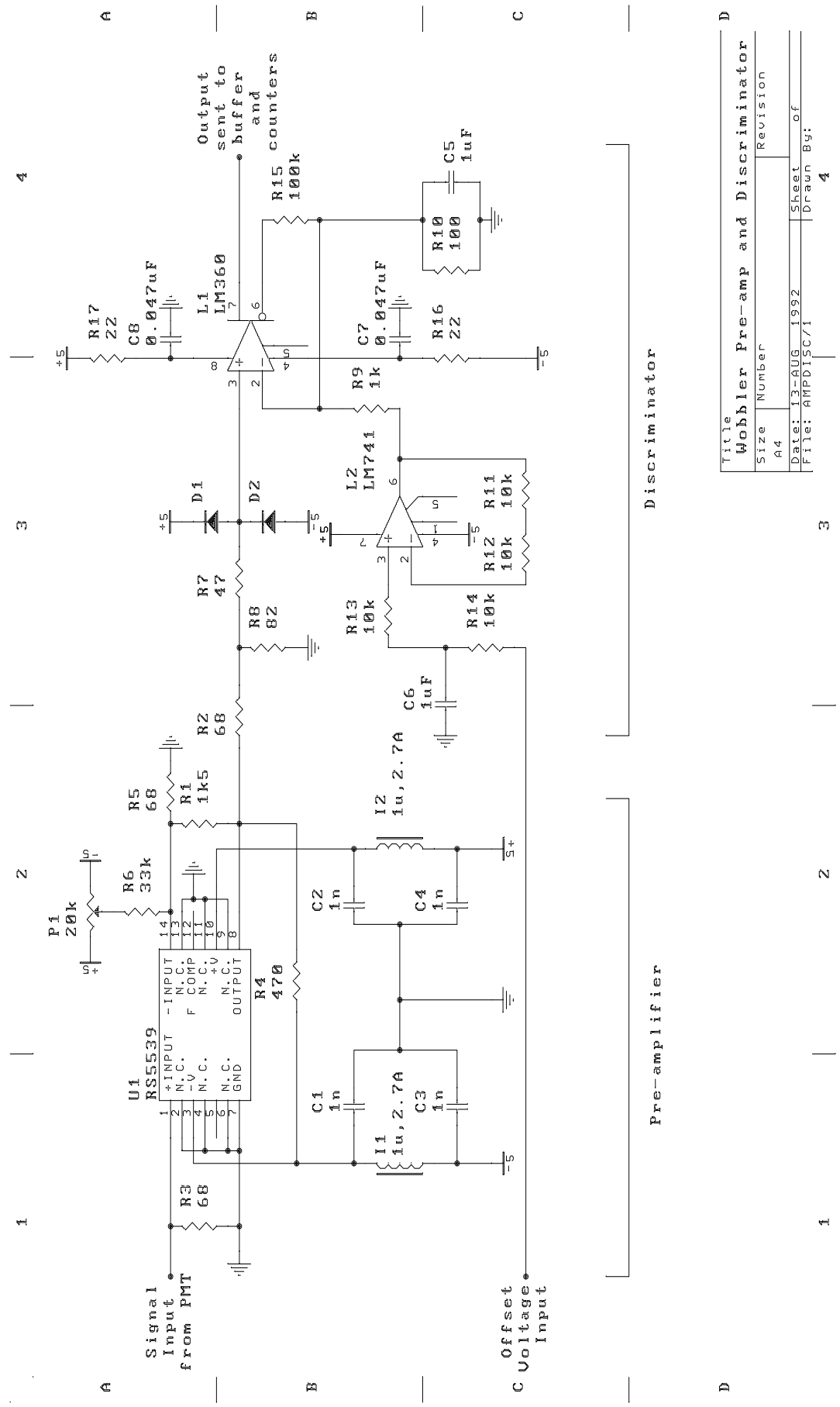
Output sent to buffer and counters
Signal Input from PMT
Offset Voltage Input
Pre-amplifier
Discriminator
U1 RS5539
L1 LM360
L2 LM741
P1 20k
R1 1k5
R2 68
R3 68
R4 470
R5 68
R6 33k
R7 47
R8 82
R9 1k
R10 100
R11 10k
R12 10k
R13 10k
R14 10k
R15 100k
R16 22
R17 22
C1 1n
C2 1n
C3 1n
C4 1n
C5 1uF
C6 1uF
C7 0.047uF
C8 0.047uF
D1
D2
I1 1u,2.7A
I2 1u,2.7A
Title Wobbler Pre-amp and Discriminator
Size A4
Number
Revision
Date: 13-AUG 1992
Sheet of
File: AMPDISC/1
Drawn By:

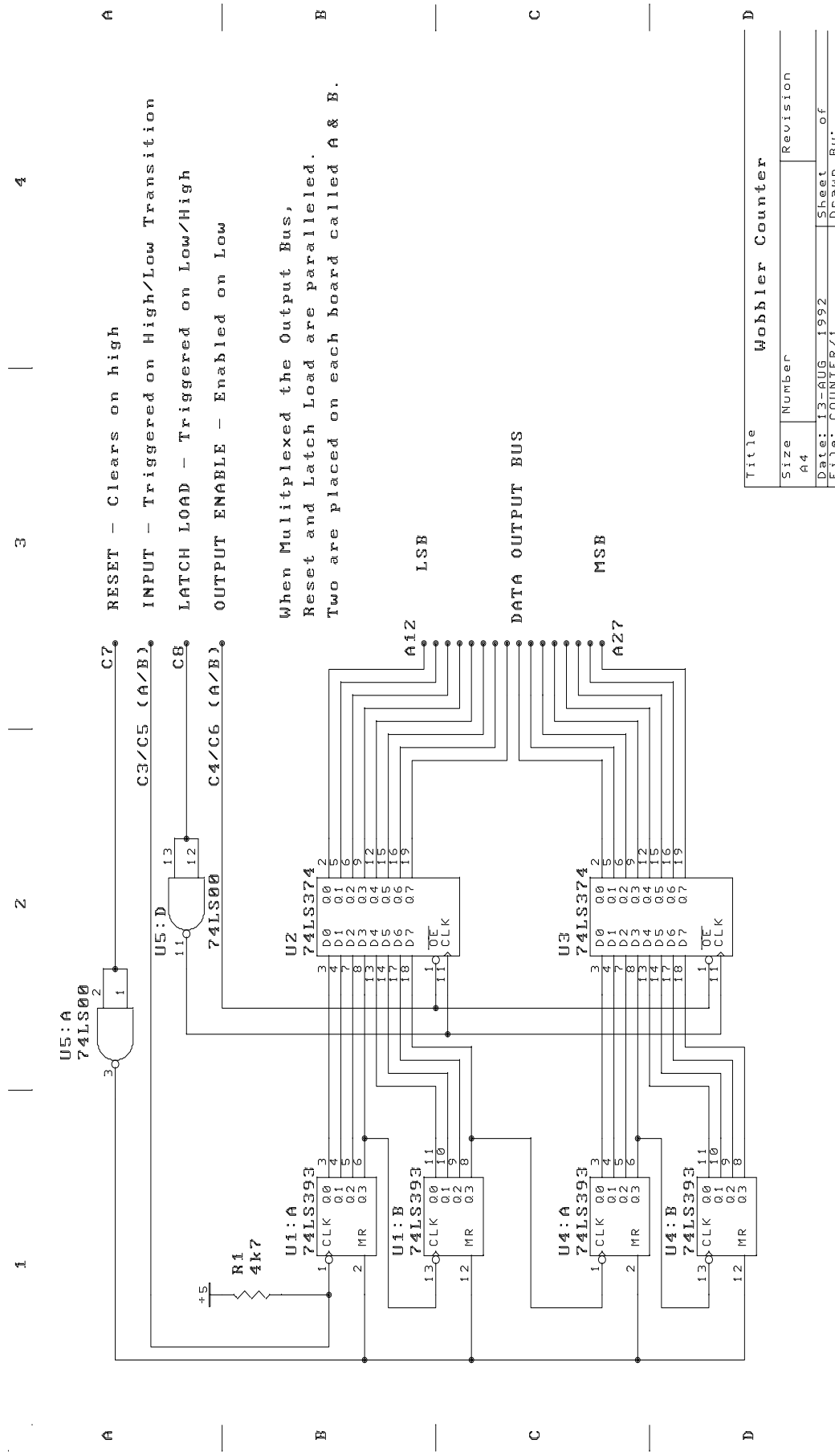
RESET - Clears on high
INPUT - Triggered on High/Low Transition
LATCH LOAD - Triggered on Low/High
OUTPUT ENABLE - Enabled on Low
When Mulitplexed the Output Bus,
Reset and Latch Load are paralleled.
Two are placed on each board called A & B.
DATA OUTPUT BUS
LSB
MSB
C7
C3/C5 (A/B)
C8
C4/C6 (A/B)
A12
A27
U5:A 74LS00
U5:D 74LS00
U2 74LS374
U3 74LS374
U1:A 74LS393
U1:B 74LS393
U4:A 74LS393
U4:B 74LS393
R1 4k7
+5
Title Wobbler Counter
Number
Revision
Size A4
Date: 13-AUG 1992
Sheet of
File: COUNTER/1
Drawn By:

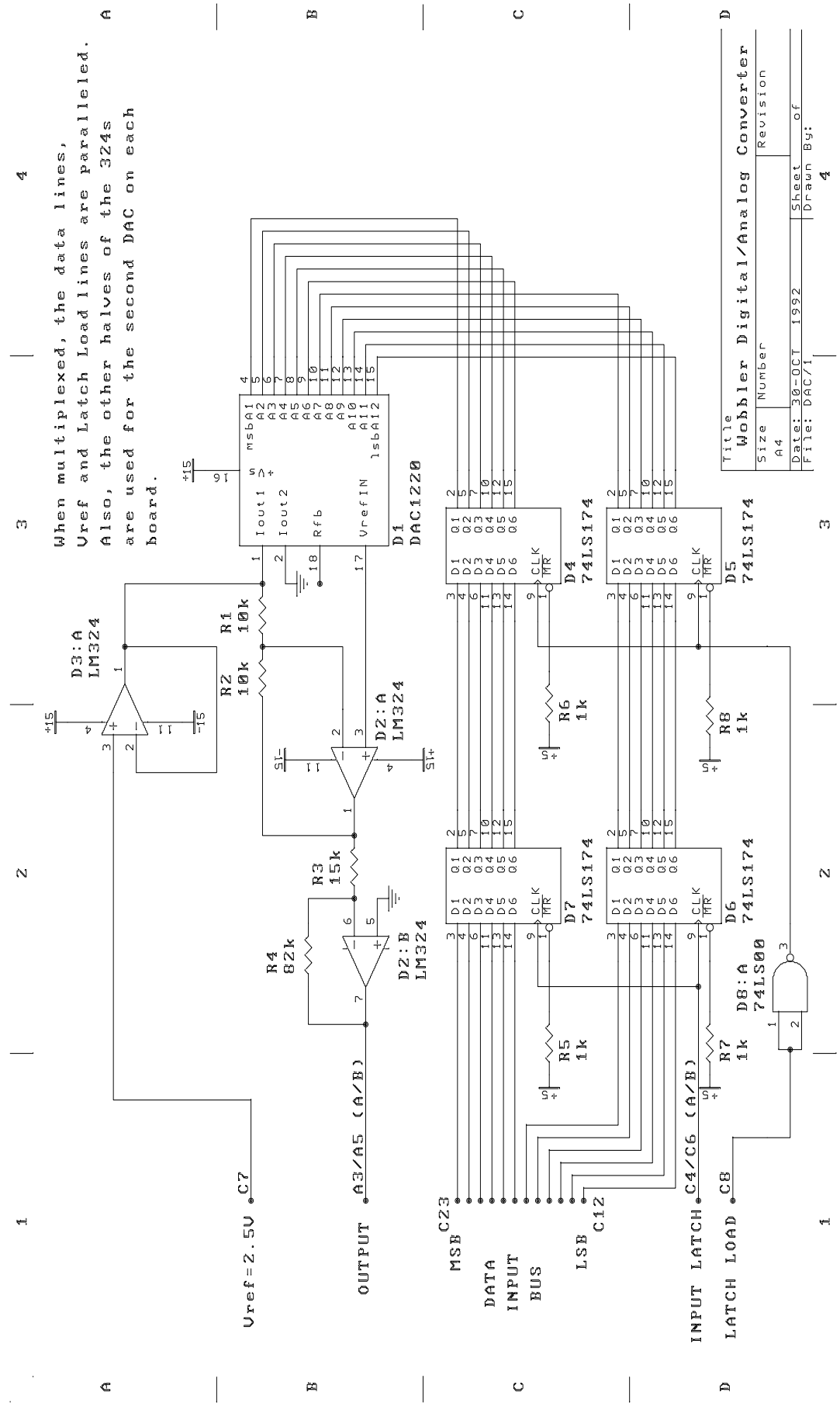
When multiplexed, the data lines,
Vref and Latch Load lines are paralleled.
Also, the other halves of the 324s
are used for the second DAC on each
board.
Title
Wobbler Digital/Analog Converter
Size
A4
Number
Revision
Date: 30-OCT 1992
Sheet of
File: DAC/1
Drawn By:
D1 DAC1220
D2:A LM324
D2:B LM324
D3:A LM324
D4 74LS174
D5 74LS174
D6 74LS174
D7 74LS174
D8:A 74LS00
R1 10k
R2 10k
R3 15k
R4 82k
R5 1k
R6 1k
R7 1k
R8 1k
Vref=2.5V C7
OUTPUT A3/A5 (A/B)
MSB C23
DATA INPUT BUS
LSB C12
INPUT LATCH C4/C6 (A/B)
LATCH LOAD C8

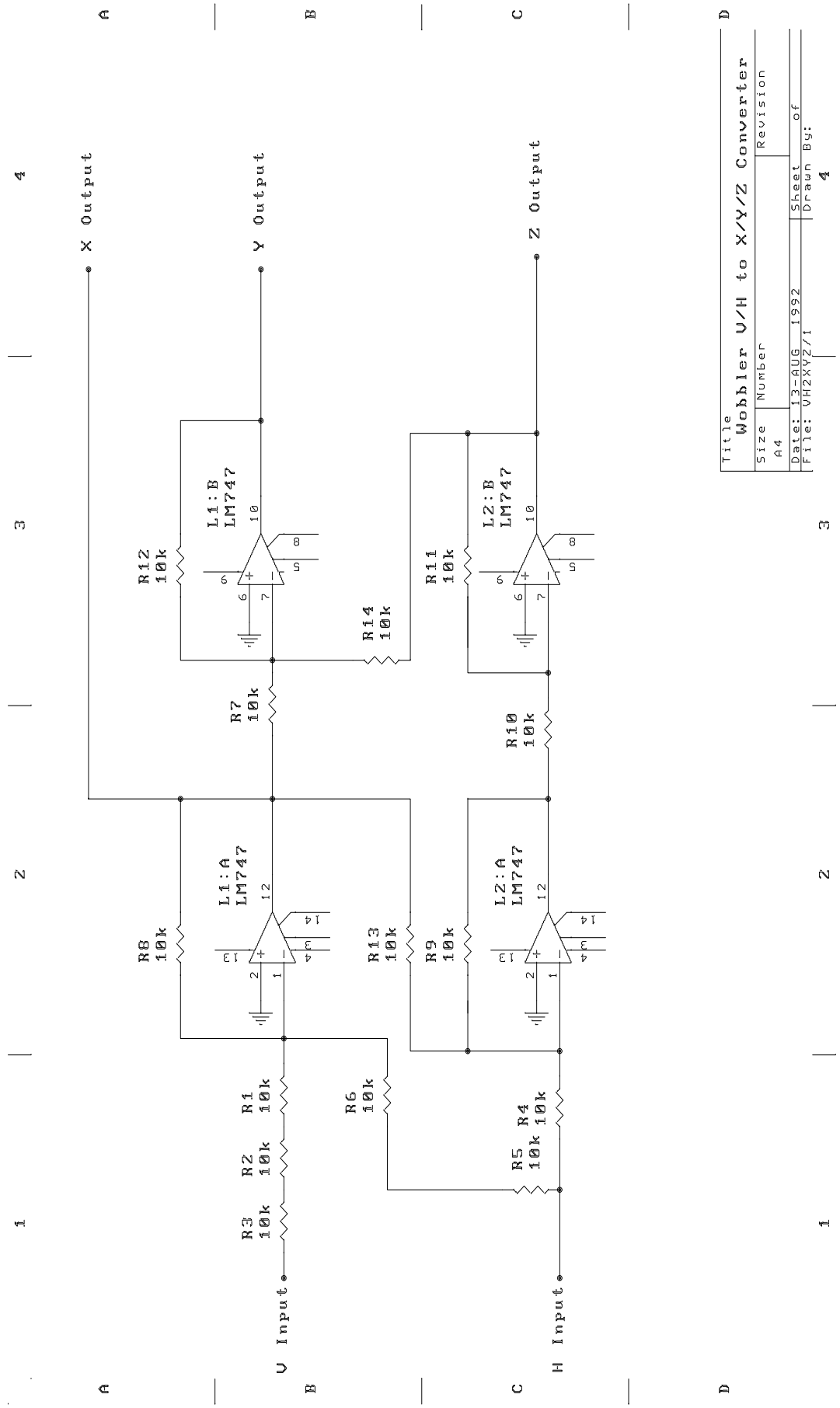
X Output
Y Output
Z Output
U Input
H Input
L1:B LM747
L2:B LM747
L1:A LM747
L2:A LM747
R12 10k
R11 10k
R14 10k
R7 10k
R10 10k
R8 10k
R13 10k
R9 10k
R6 10k
R3 10k
R2 10k
R1 10k
R5 10k
R4 10k
Title
Wobbler U/H to X/Y/Z Converter
Size A4
Number
Revision
Date: 13-AUG 1992
Sheet of
File: VH2XYZ/1
Drawn By:

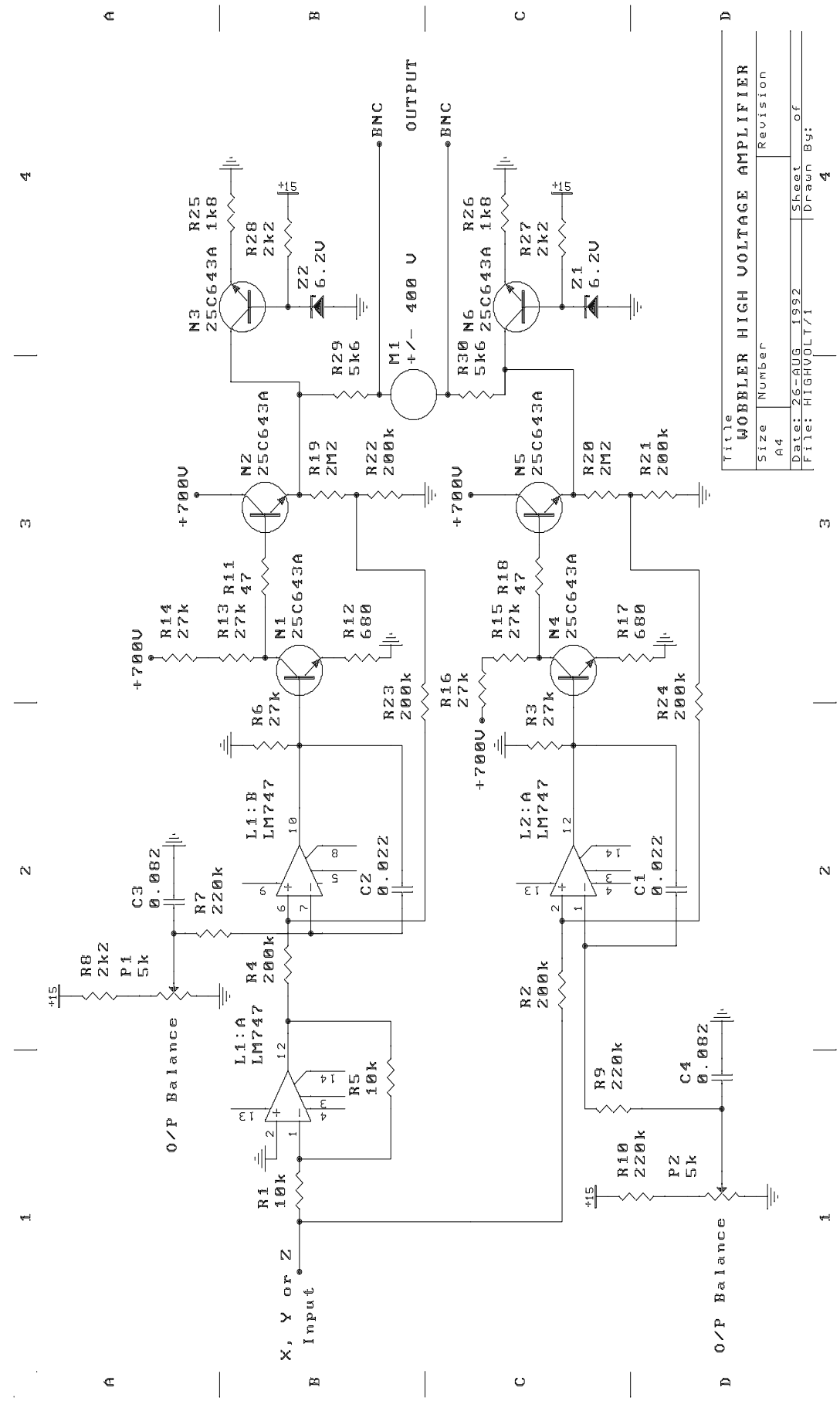
WOBBLER HIGH VOLTAGE AMPLIFIER
Size A4
Number
Revision
Date: 26-AUG 1992
File: HIGHVOLT/1
Sheet of
Drawn By:
OUTPUT
+/- 400 V
BNC
BNC
M1
N1 25C643A
N2 25C643A
N3 25C643A
N4 25C643A
N5 25C643A
N6 25C643A
L1:A LM747
L1:B LM747
L2:A LM747
Z1 6.2V
Z2 6.2V
+700V
+15
R1 10k
R2 200k
R3 27k
R4 200k
R5 10k
R6 27k
R7 220k
R8 2k2
P1 5k
R9 220k
R10 220k
P2 5k
R11 47
R12 680
R13 27k
R14 27k
R15 27k
R16 27k
R17 680
R18 47
R19 2M2
R20 2M2
R21 200k
R22 200k
R23 200k
R24 200k
R25 1k8
R26 1k8
R27 2k2
R28 2k2
R29 5k6
R30 5k6
C1 0.022
C2 0.022
C3 0.082
C4 0.082
O/P Balance
O/P Balance
X, Y or Z Input

Control Board

Pin	Outputs	Pin	Inputs
A1	+5 Volts	C1	+5 Volts
A2		C2	Clock Input
A3		C3	!EXTBUF
A4	V ref Output	C4	!LDS
A5		C5	
A6	!INT5	C6	!AUTOVECT
A7	Reset Counters	C7	!INTACK
A8	Latch Counters	C8	
A9		C9	
A10	+15 Volts	C10	+15 Volts
A11		C11	
A12	DAC 0 Latch	C12	A1
A13	DAC 1 Latch	C13	A2
A14	DAC 2 Latch	C14	A3
A15	DAC 3 Latch	C15	A4
A16	DAC 4 Latch	C16	
A17	DAC 5 Latch	C17	A17 (Module Address)
A18		C18	
A19	Counter 0 Enable	C19	
A20	Counter 1 Enable	C20	
A21	Counter 2 Enable	C21	
A22	Counter 3 Enable	C22	
A23	Counter 4 Enable	C23	
A24	Counter 5 Enable	C24	
A25	Counter 6 Enable	C25	
A26	Counter 7 Enable	C26	
A27		C27	
A28	-15 Volts	C28	-15 Volts
A29		C29	
A30		C30	
A31		C31	
A32	GROUND	C32	GROUND

Dual Counter Boards

Pin	Outputs	Pin	Inputs
A1	+5 Volts	C1	+5 Volts
A2		C2	
A3		C3	Input A
A4		C4	Output Enable A
A5		C5	Input B
A6		C6	Output Enable B
A7		C7	Reset Counters
A8		C8	Latch Load
A9		C9	
A10	+15 Volts	C10	+15 Volts
A11		C11	
A12	ED0 (LSB)	C12	Do Not Use
A13	ED1	C13	Do Not Use
A14	ED2	C14	Do Not Use
A15	ED3	C15	Do Not Use
A16	ED4	C16	Do Not Use
A17	ED5	C17	Do Not Use
A18	ED6	C18	Do Not Use
A19	ED7	C19	Do Not Use
A20	ED8	C20	Do Not Use
A21	ED9	C21	Do Not Use
A22	ED10	C22	Do Not Use
A23	ED11	C23	Do Not Use
A24	ED12	C24	Do Not Use
A25	ED13	C25	Do Not Use
A26	ED14	C26	Do Not Use
A27	ED15 (MSB)	C27	Do Not Use
A28	-15 Volts	C28	-15 Volts
A29		C29	
A30		C30	
A31		C31	
A32	GROUND	C32	GROUND

Dual Dac Boards

Pin	Outputs	Pin	Inputs
A1	+5 Volts	C1	+5 Volts
A2		C2	
A3	Output Voltage A	C3	
A4		C4	Input Latch A
A5	Output Voltage B	C5	
A6		C6	Input Latch B
A7		C7	
A8		C8	V ref Input
A9		C9	
A10	+15 Volts	C10	+15 Volts
A11		C11	
A12	Do not use	C12	ED0 (LSB)
A13	Do not use	C13	ED1
A14	Do not use	C14	ED2
A15	Do not use	C15	ED3
A16	Do not use	C16	ED4
A17	Do not use	C17	ED5
A18	Do not use	C18	ED6
A19	Do not use	C19	ED7
A20	Do not use	C20	ED8
A21	Do not use	C21	ED9
A22	Do not use	C22	ED10
A23	Do not use	C23	ED11 (MSB)
A24		C24	
A25		C25	
A26		C26	
A27		C27	
A28	-15 Volts	C28	-15 Volts
A29		C29	
A30		C30	
A31		C31	
A32	GROUND	C32	GROUND

50 Way Connecter

Pin	Data lines	Pin	Address lines
1	GROUND	26	GROUND
2		27	
3	ED0	28	!AUTOVECT
4	ED1	29	
5	ED2	30	!INTACK
6	ED3	31	
7	ED4	32	!INT5
8	ED5	33	
9	ED6	34	
10	ED7	35	A1
11	ED8	36	A2
12	ED9	37	A3
13	ED10	38	A4
14	ED11	39	
15	ED12	40	
16	ED13	41	
17	ED14	42	
18	ED15	43	
19		44	A17 (Module Address)
20		45	
21	!EXTBUF	46	
22		47	
23	!LDS	48	
24		49	
25	GROUND	50	GROUND

Appendix C

Discriminator Weighting Factors

In order for the tilt correction servo to function correctly, the weighting factors described in section (3.3.1) must be measured and put into the software. The procedure for setting these calibration factors can be broken up as follows: Setting all defaults to 1 for the weighting factors, measuring the new weight factors and implementing them as software defaults. These steps will be discussed in order.

C.1 Measuring the Weighting Factors

The procedure for measuring the weighting factors is identical in all three detector systems, so only the reference system will be discussed. With a piece of white card placed between the photomultiplier housing and the optical pyramid, use a flat mirror, as close as possible to the detector to avoid internal turbulence problems, to auto-collimate the beam. This mirror should be adjusted until the four spots of light appear to have the same intensity on the white card. Now place some neutral density into the beam (at least ND 4, ND 5 is a safe place to start) and remove the white card. With the wobbler software running, all the lights off and the high voltage on, put the wobbler software into `test` mode. This can be done via the menu system or by typing `test` on the command line. Ensure both the north and south systems are `OFF`. The function you require to measure and adjust weighting factors is called `monitor`. To look at the reference system, type `monitor reference`. You will be faced with a display showing the current counts, raw weighting factor (expressed as a factor of 256 in brackets)

and the normalised weighting factors (a floating point number) for each channel. The follow keys are also active:

- `=` Set number of samples over which to average count rates. The default is 1. It is recommended that you use an average over a large number of samples to measure weighting factors. An average over 1000 samples, that is 1 second, seems to work well. Remember that the software only polls the keyboard between each of these averages so if you have set the averaging time to a large number the computer will not respond to any key strokes for some time. The best way I have found to do this is to set the averaging time to the required value and then immediately type the `=` key again. In this way the computer will collect the required number of samples and return to this function. You can then write down the resulting numbers and reset the sample period to 1 to allow other functions to be used.
- `ESCAPE` exits the monitor function.
- `k` increases the weighting factor for the channel currently highlighted.
- `j` decreases the weighting factor for the channel currently highlighted.
- `RETURN` changes channels.

Before taking any measurements, set all the weighting factors to 1.0. This must be done with a combination of the `j`, `k` and `RETURN` keys. Alternatively, write 256 directly to the appropriate RTP registers listed below. You are now ready to measure the weighting factors. Take a sample of the counts in all four channels over a large number of samples. If the weights are correct the counts should be the same in all four channels. If the counts are not the same the new weighting factors are given by

$$\begin{aligned} W_B &= \frac{N_A}{N_B} \\ W_C &= \frac{N_A}{N_C} \\ W_D &= \frac{N_A}{N_D} \end{aligned} \tag{C.1}$$

where N_X are the counts received in channel X. The weighting factor of channel A is 1.0 by definition. In order to test these new values, set the weight factors in the software to the new values by again using the `j`, `k` and `RETURN` keys, take a new sample of the count rates and check that all four channels produce the same values. Before leaving this function, write down the raw weighting factors

printed in brackets below those you have just entered. These are required for inserting into the software to implement these new values as the defaults.

Repeat this procedure for all three detector systems. A good test of the new weighting factors is to move the detector up and down and left and right while checking that the detector output reports only vertical or horizontal movement. Any axis coupling is the result of incorrect weighting factors.

C.2 Setting New Default Values in the Software

Now that the new weighting factors are known they should be inserted into the software, otherwise you will have to manually set them every time the system is booted up or add them to the autolist. You will need the un-normalised values written down in the last section. If you do not have these values simply multiply the normalised weighting factors by 256. The procedure is then:

- Go to the `/home/susi/wobble/av68k` directory and use `sccs` to check out the file `wobble.c` for editing.
- The first function in this file is called `set_up_initial_values()` and contains the code that sets up the weight factor defaults. Edit this function and insert the new values. The piece of code should look like:

```
#ifdef TEST
        WGHT_B_N = 256; /* Weight of 1.0 (*2^8) */
        WGHT_C_N = 256; /* Weight of 1.0 (*2^8) */
        WGHT_D_N = 256; /* Weight of 1.0 (*2^8) */

        WGHT_B_S = 256; /* Weight of 1.0 (*2^8) */
        WGHT_C_S = 256; /* Weight of 1.0 (*2^8) */
        WGHT_D_S = 256; /* Weight of 1.0 (*2^8) */

        WGHT_B_R = 256; /* Weight of 1.0 (*2^8) */
        WGHT_C_R = 256; /* Weight of 1.0 (*2^8) */
        WGHT_D_R = 256; /* Weight of 1.0 (*2^8) */
#else
        WGHT_B_N = 161;
        WGHT_C_N = 259;
```

```
            WGHT_D_N = 164;

            WGHT_B_S = 409;
            WGHT_C_S = 256;
            WGHT_D_S = 410;

            WGHT_B_R = 64;
            WGHT_C_R = 359;
            WGHT_D_R = 64;
    #endif
```

where the numbers above are the weighting factors at the time of writing.

- Recompile and release the software.
- If all has gone well check the file `wobble.c` back into `sccs`.

The new weighting factors are now the default values. It is probably best to check the new software by completely re-booting the wobbler system.

Remember that these weighting factors can be changed at any time by using the `monitor` command or by simply writing the raw normalisation factors directly to the appropriate `RTP` registers. These registers are:

```
#define N_WGHT_B_N 5  /* Weight factor (* 256) for North B */
#define N_WGHT_C_N 6  /* Weight factor (* 256) for North C */
#define N_WGHT_D_N 7  /* Weight factor (* 256) for North D */
#define N_WGHT_B_S 9  /* Weight factor (* 256) for South B */
#define N_WGHT_C_S 10 /* Weight factor (* 256) for South C */
#define N_WGHT_D_S 11 /* Weight factor (* 256) for South D */
#define N_WGHT_B_R 13 /* Weight factor (* 256) for Reference B */
#define N_WGHT_C_R 14 /* Weight factor (* 256) for Reference C */
#define N_WGHT_D_R 15 /* Weight factor (* 256) for Reference D */
```

Appendix D

Optimised Servo Parameters

Tabulated below are the optimised servo parameters for a range of sample times. These values have been chosen to yield a specified frequency response while having a resonance no greater than 3dB. Bandwidths move up in steps of 5Hz, except for the last maximum bandwidth for each sample time. Refer to section (4.2.5) for a detailed discussion on how these numbers can be generated. The results tabulated below are for use with the (recommended) 35mm aperture. If another aperture is used, multiply the C_1 value by the appropriate correction value, tabulated in table (D.1).

Aperture (mm)	C_1 correction term
20	1.69
25	1.39
30	1.17
35	1.00
40	0.87

Table D.1: The multiplicative correction factor of servo parameter C_1 for different aperture diameters. The numbers here are a result of the calculations in section (3.1.3).

Bandwidth f_{-45^o} Hz	C_1	C_2	Track Gain$_{\text{res}}$ dB	Track f_{res} Hz	Track f_{-3dB} Hz	Measure Gain$_{\text{res}}$ dB	Measure f_{-3dB} Hz
5.0	0.007	0.08	-0.13	< 1.0	5.9	-0.13	5.9
10.0	0.014	0.01	-0.02	< 1.0	13.9	-0.02	14.4
15.0	0.027	0.28	-0.01	< 1.0	23.5	-0.01	25.8
20.0	0.034	0.12	0.00	< 1.0	37.1	0.00	44.2
25.0	0.074	0.93	0.00	< 1.0	45.0	0.00	56.9
30.0	0.095	0.96	0.00	8.1	56.6	0.37	75.5
35.0	0.115	0.95	0.15	26.3	68.2	1.04	95.4
40.0	0.135	0.92	0.44	37.3	79.6	1.83	117.4
45.0	0.155	0.88	0.78	46.4	91.0	2.66	142.5
47.6	0.175	0.97	0.90	49.8	95.9	2.97	161.8

Table D.2: Optimal servo parameters for a range of bandwidths are shown here for a sample time of 1ms and an aperture diameter of 35mm on the optical table.

Bandwidth f_{-45^o} Hz	C_1	C_2	Track Gain$_{\text{res}}$ dB	Track f_{res} Hz	Track f_{-3dB} Hz	Measure Gain$_{\text{res}}$ dB	Measure f_{-3dB} Hz
5.0	0.014	0.05	-0.11	< 1.0	6.3	-0.11	6.4
10.0	0.034	0.21	-0.02	< 1.0	16.0	-0.01	16.8
15.0	0.047	0.05	0.00	< 1.0	31.5	0.00	35.7
20.0	0.115	0.84	0.00	4.6	44.5	0.15	53.3
25.0	0.162	0.97	0.47	28.5	59.6	1.24	74.1
30.0	0.203	0.96	1.40	40.8	73.5	2.73	94.4

Table D.3: Optimal servo parameters for a range of bandwidths are shown here for a sample time of 2ms and an aperture diameter of 35mm on the optical table.

Bandwidth f_{-45° Hz	C_1	C_2	Track Gain$_{\text{res}}$ dB	Track f_{res} Hz	Track f_{-3dB} Hz	Measure Gain$_{\text{res}}$ dB	Measure f_{-3dB} Hz
5.0	0.020	0.02	-0.09	< 1.0	6.8	-0.09	6.9
10.0	0.047	0.09	-0.01	< 1.0	19.5	-0.01	20.7
15.0	0.114	0.65	0.00	5.5	36.8	0.09	41.6
20.0	0.189	0.93	1.01	28.6	53.4	1.70	61.9
22.7	0.223	0.95	1.99	35.4	61.2	2.96	79.7

Table D.4: Optimal servo parameters for a range of bandwidths are shown here for a sample time of 3ms and an aperture diameter of 35mm on the optical table.

Bandwidth f_{-45° Hz	C_1	C_2	Track Gain$_{\text{res}}$ dB	Track f_{res} Hz	Track f_{-3dB} Hz	Measure Gain$_{\text{res}}$ dB	Measure f_{-3dB} Hz
5.0	0.027	0.00	-0.08	< 1.0	7.4	-0.08	7.5
10.0	0.061	0.01	0.00	< 1.0	24.0	0.00	25.7
15.0	0.189	0.98	0.70	21.3	41.8	1.09	46.3
18.1	0.236	0.98	2.27	30.0	51.3	2.98	61.0

Table D.5: Optimal servo parameters for a range of bandwidths are shown here for a sample time of 4ms and an aperture diameter of 35mm on the optical table.

Bandwidth f_{-45° Hz	C_1	C_2	Track Gain$_{\text{res}}$ dB	Track f_{res} Hz	Track f_{-3dB} Hz	Measure Gain$_{\text{res}}$ dB	Measure f_{-3dB} Hz
5.0	0.041	0.18	-0.07	< 1.0	7.9	-0.07	8.0
10.0	0.122	0.59	0.00	< 1.0	26.5	0.02	28.4
15.0	0.236	0.93	2.46	25.8	43.9	2.99	47.6

Table D.6: Optimal servo parameters for a range of bandwidths are shown here for a sample time of 5ms and an aperture diameter of 35mm on the optical table.

Bandwidth f_{-45° Hz	C_1	C_2	Track Gain$_{\text{res}}$ dB	Track f_{res} Hz	Track f_{-3dB} Hz	Measure Gain$_{\text{res}}$ dB	Measure f_{-3dB} Hz
5.0	0.047	0.12	-0.05	< 1.0	8.8	-0.05	8.9
10.0	0.182	0.95	0.39	13.4	29.0	0.54	30.7
12.8	0.243	0.95	2.55	22.6	38.3	2.96	40.8

Table D.7: Optimal servo parameters for a range of bandwidths are shown here for a sample time of 6ms and an aperture diameter of 35mm on the optical table.

Bandwidth f_{-45° Hz	C_1	C_2	Track Gain$_{\text{res}}$ dB	Track f_{res} Hz	Track f_{-3dB} Hz	Measure Gain$_{\text{res}}$ dB	Measure f_{-3dB} Hz
5.0	0.054	0.08	-0.04	< 1.0	9.7	-0.04	9.9
10.0	0.216	0.94	1.43	17.0	30.5	1.67	31.9
11.2	0.243	0.92	2.65	20.1	34.0	2.97	35.7

Table D.8: Optimal servo parameters for a range of bandwidths are shown here for a sample time of 7ms and an aperture diameter of 35mm on the optical table.

Bandwidth f_{-45° Hz	C_1	C_2	Track Gain$_{\text{res}}$ dB	Track f_{res} Hz	Track f_{-3dB} Hz	Measure Gain$_{\text{res}}$ dB	Measure f_{-3dB} Hz
5.0	0.061	0.04	-0.03	< 1.0	11.0	-0.03	11.2
10.0	0.250	0.96	2.64	17.9	30.4	2.90	31.6

Table D.9: Optimal servo parameters for a range of bandwidths are shown here for a sample time of 8ms and an aperture diameter of 35mm on the optical table.

Bandwidth f_{-45^o} Hz	C_1	C_2	Track Gain$_{\rm res}$ dB	Track $f_{\rm res}$ Hz	Track f_{-3dB} Hz	Measure Gain$_{\rm res}$ dB	Measure f_{-3dB} Hz
5.0	0.068	0.01	-0.02	< 1.0	12.2	-0.02	12.5
8.9	0.216	0.68	2.78	16.2	27.5	2.99	28.4

Table D.10: Optimal servo parameters for a range of bandwidths are shown here for a sample time of 9ms and an aperture diameter of 35mm on the optical table.

Sample time ms	Band-width f_{-45^o}Hz	C_1	C_2	Track Gain$_{\rm res}$ dB	Track $f_{\rm res}$ Hz	Track f_{-3dB} Hz	Measure Gain$_{\rm res}$ dB	Measure f_{-3dB} Hz
0.010	8.1	0.230	0.77	2.77	14.8	25.2	2.95	25.9
0.015	5.6	0.216	0.62	2.90	10.4	17.7	2.99	17.9
0.020	4.3	0.236	0.74	2.95	8.0	13.6	3.00	13.7
0.030	2.9	0.149	0.09	2.96	5.4	9.2	2.98	9.2
0.035	2.5	0.142	0.04	2.91	4.6	7.9	2.93	7.9
0.040	2.2	0.142	0.03	2.98	4.1	7.0	2.99	7.0
0.045	2.0	0.162	0.17	2.97	3.6	6.3	2.99	6.3
0.050	1.8	0.142	0.03	2.90	3.3	5.6	2.90	5.6

Table D.11: Optimal servo parameters for and an aperture diameter of 35mm on the optical table and sample times of 10ms and greater. As the bandwidth becomes so small at these sample times, only the 'best' servo parameters have been listed.

Appendix E

Time Line and Important Dates

February 1988	Research work commenced.
April 1988	Counters/DACs and interface electronics constructed.
July 1988	PMT housing modified and wired up.
December 1988	Preamp/Discriminator design and PC board layout finalised.
January-August 1989	AV68000 computer integrated into system and the programming platform developed.
September 1989	Quadrant detector alignment procedure developed.
October 1989	High voltage amplifiers complete. Test system installed on optical table.
November 1989	First successful test of tilt servo on optical table.
January 1990	Begin installation of tilt system at Narrabri.
May 1990	System installation at Narrabri begins. Mirror calibration experiments performed.
January 1991	SUSI first light. Acquisition system and siderostats working.
March 1991	Tilt system first used to track stellar image of α Cen.
August 1991	Tilt servo and star guidance system fully integrated. Extensive tests of acquisition and tilt servo system performed. First stellar fringes obtained with SUSI.
December 1991	Quadrant detector noise tests performed.
January-April 1992	Seeing data collection at Narrabri.

REFERENCES

Acton, D.S., Sharbaugh, R.J., Roehrig, J.R. and Tiszauer, D., (1992) "Wave-Front Tilt Power Sprectral Density from the Image Motion of Solar Pores," *Applied Optics*, **31**, 4280-4284.

Allen, C.W., (1973) *Astrophysical Quantities* (University of London Athlone Press: London) .

Andrews, L.C., (1992) "An Analytic Model for the Refractive Index Power Spectrum and its Application to Optical Scintillations in the Atmosphere," *Journal of Modern Optics*, **39(9)**, 1849-1853.

Babcock, H.W., (1953) "The Possibility of Compensating Astronomical Seeing," *Pub A.S.P.*, **65**, 229-236.

Barbe, E.C., (1963) *Linear Control Systems* Ed: Lambert, R.F. (International Textbook Company: Scranton, Pennsylvania) .

Bedding, T.R., Robertson, J.G., Marson, R.G., Gillingham, R.H, Frater, R.H. and O'Sullivan, J.D., (1992) "MAPPIT: Interferometry with Non-Redundant Masks and Wavelength Dispersion," *Proceedings: High Resolution Imaging by Interferometry II*, **Ed: Merkle, F.**, E.S.O.

Bester, M., Danchi, W.C., Degiacomi, C.G., Greenhill, L.J. and Townes, C.H., (1992) "Atmospheric Fluctuations: Empirical Structure Functions and Projected Performance of Future Instruments," *The Astrophysical Journal*, **392**, 357-374.

Beyer, W.H., (1979) *CRC Standard Mathematical Tables* Ed: Beyer (CRC Press Inc.: Boca Raton, Florida) .

Born, M. and Wolf, E., (1987) *Principles of Optics* (Pergammon Press: Oxford) .

Bracewell, R.N., (1986) *The Fourier Transform and its Applications* (McGraw-Hill: New York) .

ten Brummelaar, T.A., (1985) *A Microthermal Array for Measuring Local Contributions to Seeing* Honours Year Thesis (Chatterton Astronomy Department, University of Sydney: Sydney) .

Buffington, A., Crawford, F.S., Pollaine, S.M., Orth, C.D. and Muller, R.A., (1978) "Sharpening Stellar Images," *Science*, **200**, 489-494.

Buscher, D.F., (1988) *Getting the most out of C.O.A.S.T.* Ph.D. Thesis (Cambridge University: Cambridge) .

Clark, L.D., Shao, M. and Colavita, M.M., (1986) "A Photon-Camera Star Tracker for Stellar Interferometry," *SPIE Instrumentation in Astronomy*, **627**, 838-845.

Clifford, S.F., (1971) "Temporal-Frequency Spectra for a Spherical Wave Propagating through Atmospheric Turbulence," *J. Opt. Soc. Am.*, **61**, 1285-1292.

Colavita, M., Shao, M. and Staelin, D.H., (1987) "Atmospheric Phase Measurements with the Mark III Stellar Interferometer," *Applied Optics*, **26**, 4106-4112.

Coulman, C.E., (1969) "A Quantitative Treatment of Solar 'Seeing', I," *Solar Physics*, **7**, 122-143.

Coulman, C.E., (1974) "A Quantitative Treatment of Solar 'Seeing', II," *Solar Physics*, **34**, 491-506.

Coulman, C.E., (1985) "Fundamental and Applied Aspects of Astronomical 'Seeing'," *Ann. Rev. Astron. Astrophys.*, **23**, 19-57.

Coulman, C.E., (1987) "Some Thoughts on Seeing: Mainly what we still do not know.," *Proceedings: Workshop on Adaptive Optics in Solar Observations*, **Ed: Merkle, F., Engvold, O. and Falomo, R.**, 205-211.

Cubalchini, R., (1979) "Modal Wave-Front Estimation from Phase Derivative Measurements," *J. Opt. Soc. Am.*, **66**, 972-977.

Davis (a), J. and Tango, W.J., (1985) "The Sydney University 11.4m Prototype Stellar Interferometer," *Proc. A.S.A.*, **6**, 34-38.

Davis (b), J. and Tango, W.J., (1985) "A New Very High Angular Resolution Stellar Interferometer," *Proc. A.S.A.*, **6**, 38-43.

Davis, J. and Tango, W.J., (1986) "New Determination of the Angular Diameter of Sirius," *Nature*, **323**, 234-235.

Davis (a), J., Tango, W.J., Booth, A.J., a, R.A.rMinard, ten Brummelaar, T.A. and T.A. Shobbrook, R.R, (1992) "An update on SUSI," *Proceedings: High Resolution by Interferometry II*, **Ed: Merkle, F.**, E.S.O.

Davis (b), J., Tango, W.J., Booth, A.J., ten Brummelaar, T.A., Minard, R.A., Owens, S.M. and Shobbrook, R.R., (1992) "The Sydney University Stellar Interferometer," , , In preparation.

Doel, A.P., Dunlop, C.N., Major, J.V., Myers, R.M., Purvis, A. and Thompson, M.G., (1990) "Stellar Image Stabilization using Piezo-driven Active Mirrors," *S.P.I.E. Advanced Optical Telescopes IV*, **1236**, 179-192.

Dorf, R.C., (1974) *Modern Control Systems* (Addison-Wesley: Philippines) .

DuPuy, D.L., (1981) "An Integrated-Circuit Pulse Amplifier for use with Photomultipliers," *Pub. A.S.P.*, **93**, 144-146.

Dyson, F.J., (1975) "Photon Noise and Atmospheric Noise in Active Optical Systems," *J.Op.Soc.Am.*, **65**, 551-558.

Fields, D.R., (1983) "High Frequency Behavior of the Tilt Spectrum of Atmospheric Turbulence," *Applied Optics*, **22**, 645-647.

Forbes (b), F.F., (1983) *Acoustic and Microthermal Atmospheric Soundings at Kitt Peak and Mt. Graham* (Draft Copy: USA) .

Forbes, F.F, Barker, E.S., Peterman, K.R., Cudaback, D.D. and Morse, D.A., (1985) "High Altitude Acoustic Soundings," *SPIE Technical Symposium East*, **551**, .

Franklin, G.F. and Powell, J.D., (1980) *Digital Control of Dynamic Systems* (Addison Wesley Pub. Comp.: Reading MA.) .

Fried, D.L., (1966) "Optical Resolution Through a Randomly Inhomogeneous Medium for Very Long and Very Short Exposures," *J. Opt. Soc. Am.*, **56**, 1372-1379.

Fried, D.L., (1965) "Statistics of a Geometric Representation of Wavefront Distortion," *J. Opt. Soc. Am.*, **55**, 1427-1435.

Fried, D.L., (1979) *The Nature of Atmospheric Turbulence Effects on Imaging and Pseudo-Imaging Systems, and its Quantification* Ed: Davis, J. and Tango, W.J. (High Angular Resolution Astronomy (I.A.U. COLL. No 50.): Chatterton Astronomy Department: Sydney) 4-1,4-44.

Fried, D.L. and Mevers, G.E., (1974) "Evaluation of r_0 for Propagation Down Through the Atmosphere," *Applied Optics*, **13**, 2620-2622.

Frisch, U. and Orszag, S.A., (1990) "Turbulence: Challenges for Theory and Experiment," *Physics Today*, **January**, 24-32.

Gilliand, Y.A., (1992) *Design and Implementation of a Variable Optical Path Length Compensation System for SUSI* Ph.D. thesis (Chatterton Astronomy Dept. University of Sydney: Sydney) .

Greenwood, D.P., (1977) "Bandwidth Specification for Adaptive Optics Systems," *J. Opt. Soc. Am.*, **67**, 390-393.

Greenwood, D.P. and Fried, D.L., (1976) "Power Spectra Requirements for Wave-Front-Compensative Systems," *J. Opt. Soc. Am.*, **66**, 193-206.

Hanbury Brown, R., Davis, J and Allen, L.R., (1974) "The Angular Diameters of Thirty Two Stars," *Mon. Not. R. Astr. Soc.*, **167**, 121-136.

Harris, H.C. and Vrba, F.J., (1992) "Seeing Measurements and Observing Statistics at the U.S. Naval Observatory, Flagstaff Station," *P.A.S.P.*, **104**, 140-145.

Hartley, M, Mcinnes, B. and Graham Smith, F., (1981) "Microthermal Fluctuations and their Relation to Seeing Conditions at Roque de los Muchachos Observatory, La Palma," *Q.Jl R. Astr. Soc.*, **22**, 272-278.

Herrmann, J., (1981) "Cross Coupling and Aliasing Modal Wave-Front Estimation," *J. Opt. Soc. Am.*, **71**, 989-992.

Hogge, C.B. and Butts, R.R., (1976) "Frequency Spectra for the Geometric Representation of Wavefront Distortions Due to Atmospheric Turbulence," *IEEE Trans. Antennas Propagat.*, **AP-24**, 144-154.

Horrit, D. and Jaschek, C., (1982) *The Bright Star Catalogue* (Yale University Observatory: New Haven) .

Hrynevych, M., (1992) *Diffraction Effects in Michelson Stellar Interferometry* Ph.D. Thesis (Chatterton Astronomy Dept. University of Sydney: Sydney) .

Jorgenson, M.B., Aitken, G.J.M. and Hege, E.K., (1991) "Evidence of a Chaotic Attractor in Star-Wander Data," *Optics Letters Opt. Soc. Am.*, **16**, 64-66.

Jorgenson, M.B. and Aitken, J.M., (1992) *Prediction of Turbulence Induced Wavefront Degradations* Ed: Merkle, F. (Proceedings: High Resolution Imaging by Interferometry II:) E.S.O.

Kolmogorov (a), A., (1941) *The Local Structure of Turbulence in Incompressible Viscous Fluid for Very Large Reynolds' Numbers* Ed: Friedlander, S.K. and Topper, L. (Reprinted 1961 in 'Turbulence', Interscience Publishers, Inc.: New York) 151-155.

Kolmogorov (b), A., (1941) *On Degeneration of Isotropic Turbulence in an Incompressible Viscous Fluid* Ed: Friedlander, S.K. and Topper, L. (Reprinted 1961 in 'Turbulence', Interscience Publishers, Inc.: New York) 156-158.

Kolmogorov (c), A., (1941) *Dissipation of Energy in the Locally Isotropic Turbulence* Ed: Friedlander, S.K. and Topper, L. (Reprinted 1961 in 'Turbulence', Interscience Publishers, Inc.: New York) 159-161.

Lawrence, G.N. and Chow, W.W., (1984) "Wave-front Tomography by Zernike Polynomial Decomposition," *Optics Letters*, **9**, 267-269.

Lee, R.W. and Harp, J.C., (1969) "Weak Scattering in Random Media, with Applications to Remote Probing," *Proc. I.E.E.E.*, **57**, 375-406.

Lopez, B., (1991) "Last Mission at La Silla, April 19 to May 8, on the Measure of the Wavefront Evolution Velocity," *E.S.O. Internal Report*, , .

Maaswinkel, F., Bortoletto, F., D'Odoico, D and Huster, G, (1987) *Image Stabalisation at the ESO 2.2-Meter Telescope with DISCO in 'Instrumentation for Ground Based Optical Astronomy'* Ed: R, L.B.obinson (Springer-Verlag: New York) 360-365.

McKechnie (a), T.S., (1991) "Propagation of the Spectral Correlation Function in a Homogeneous Medium," *J. Opt. Soc. Am. A.*, **8**, 339-345.

McKechnie (b), T.S., (1991) "Light Propagation Through the Atmosphere and the Properties of images formed by Large Ground-Based Telescopes," *J. Opt. Soc. Am. A.*, **8**, 346-365.

Merkle, F., Rousset, G., Kern, P. and Gaffard, J.P., (1990) "First Diffraction-Limited Astronomical Images with Adaptive Optics," *S.P.I.E. Advanced technology telescopes IV*, **1236**, 193-202.

Merrill, B.R., (1991) "Equivalence of Two Theories of Beam Tilt," *J. Opt. Soc. Am. A.*, **8**, 1316-1318.

Miller, M.G. and Zieske, P.L., (1977) "Measurement of the Atmospheric Correlation Scale," *J. Opt. Soc. Am.*, **67**, 1680-1685.

Muller, R.A. and Buffington, A., (1974) "Real-Time Correction of Atmospherically Degraded Telescope Images Through Image Sharpening," *J. Opt. Soc. Am.*, **64**, 1200-1210.

Newton, I., (1730 (Re-printed 1952)) *Optics, a Treatise of the Reflections, Refractions, Inflections and Colours of Light.* (Dover Publications: London) .

Nightingale, N.S., (1991) "A New Silicon Avalanche Photodiode Photon Counting Detector for Astronomy," *Experimental Astronomy*, **1(6)**, 407-422.

Nightingale, N.S. and Buscher, D.F., (1991) "Interferometric seeing measurements at La Palmer," *Mon. Not. R. astr. Soc.*, **251**, 155-166.

Noll, R.J., (1976) "Zernike Polynomials and Atmospheric Turbulence," *J. Op. Soc. Am.*, **66**, 207-211.

O'Byrne, J.W., (1988) "Seeing Measurements using a Shearing Interferometer," *Proc. Ast. Soc. Pac.*, **100**, 1169-1177.

Palmer, G., (1988) *Sunlab Discriminator: An adventure in Electronics* Honours Year Report (University of Sydney: Sydney) .

Papaliolios, C. and Mertz, L., (1982) "New Two Dimensional Photon Camera," *S.P.I.E. Instrumentation in Astronomy IV*, **331**, 360-364.

Press, W.H., Falnnery, B.P., Teukolsky, S.A. and Vetterlimg, W.T, (1990) *Numerical Recipes in C: The Art of Scientific Computing* (Cambridge University Press: Cambridge) .

Radio Shack, , (1988) "Ultra High Speed Operational Amplifier 5539," *Radio Shack Data Library*, **5601**, 1-6.

Rhodes, W.T. and Goodman, J.W., (1973) "Interferometric Technique for Recording and Restoring Images Degraded by Unknown Aberrations," *J.Opt.Soc.Am.*, **6**, 647-657.

Richardson, L.F., (1922) *Weather Prediction by Numerical Process* Intro: S. Chapman. (Cambridge Uni. Press (Reprinted 1965, Dover Pub. Inc.): New York) .

Roddier, F., (1981) "The Effects of Atmospheric Turbulence in Optical Astronomy," *Progress in Optics*, **XIX**, 281-376.

Roddier, F., Graves, J.E. and Limburg, E., (1990) "Seeing Monitor Based on Wavefront Curvature Sensing," *S.P.I.E.: Advanced technology Optical Telescopes IV*, **1236**, 474-479.

Roddier, F., Northcott, M. and Elon Graves, E., (1991) "A Simple Low-Order Adaptive Optics System for Near-Infrared Applications," *Pub. Ast. Soc. Pac.*, **103**, 131-149.

Seneta, E.B., (1991) *A Video Acquisition System for the Sydney University Stellar Interferometer* M.Sc. Thesis (Chatterton Astronomy Dept. University of Sydney: Sydney) .

Spiegel, M.R., (1968) *Mathematical Handbook of Formulas and Tables* (McGraw-Hill Book Company:) .

Stull, R.B., (1991) *An Introduction to Boundary Layer Meteorology* First Published 1988 (Kluwer Academic Press: Dordrecht) .

Tango, W.J., (1990) "Dispersion in Stellar Interferometry," *Applied Optics*, **29**, 516-521.

Tango, W.J., (1979) *High Angular Resolution Stellar Interferometry* I.A.U. Colloquium No. 50, Ed: Davis, J. and Tango, W.J. (Chatterton Astronomy Dept, University of Sydney: Sydney) 12.1.

Tango, W.J. and Twiss, R.Q., (1980) "Michelson Stellar Interferometry," *Progress in Optics*, **XVII**, 239-277.

Tatarski, V.I., (1971) *The Effects of the Turbulent Atmosphere on Wave Propagation* (Israel Program for Scientific Translations: Jerusalem) .

Tatarski, V.I., (1961) *Wave Propagation in a Turbulent Medium* (Dover: New York) .

Taylor, D.J., (1980) "A Simple Repetitive Filter Cycle Photometer with Sky Background Compensation," *Pub. A.S.P.*, **92**, 108-144.

Taylor, G.I., (1935) *Statistical Theory of Turbulence* Ed: Friedlander, S.K. and Topper, L. (Reprinted 1961 in 'Turbulence', Interscience Publishers, Inc.: New York) 18-75.

Taylor, G.I., (1937) *The Spectrum of Turbulence* Ed: Friedlander, S.K. and Topper, L. (Reprinted 1961 in 'Turbulence', Interscience Publishers, Inc.: New York) 100-114.

Taylor, G.I, (1921) *Diffusion by Continuous Movements* Ed: Friedlander, S.K. and Topper, L. (Reprinted 1961 in 'Turbulence', Interscience Publishers, Inc.: New York) 1-17.

Thorvaldson, E.D., (1991) *Pointing the Siderostats of SUSI* Honours Year Thesis (Chatterton Astronomy Department, University of Sydney: Sydney) .

Tokovinin, A.A and Shcheglov, P.V., (1979) "Achieving High Resolution in Earth-based Optical Astronomy," *Sov. Phys. Usp.*, **22**, 960-974.

Tyler, G.A. and Fried, D.L., (1982) "Image-Position Error Associated with a Quadrant Detector," *J. Opt. Soc. Am.*, **72**, 804-808.

Tyson, R.K., (1991) *Principles of Adaptive Optics* (Academic Press Inc: Boston) .

Walkup, J.F. and Goodman, J.W., (1973) "Limitations of Fringe-Parameter Estimation at Low Light Levels," *J. Opt. Soc. Am.*, **63**, 399-407.

Walters, D.L., (1981) "Atmospheric Modulation Transfer Function for Desert and Mountain Locations: r_0 Measurements.," *J. Opt. Soc. Am.*, **71**, 406-409.

Walters, D.L., Favier, D.L. and Hines, J.R., (1979) "Vertical Path Atmospheric MTF Measurements," *J. Opt. Soc. Am.*, **69**, 828-837.

Walters, D.L. and Kunkel, K.E., (1981) "Atmospheric Modulation Transfer Function for Desert and Mountain Locations: the Atmospheric effects on r_0," *J. Opt. Soc. Am.*, **71**, 397-405.

Wang, J.Y. and Markey, J.K., (1978) "Modal Compensation of Atmospheric Turbulence Phase Distortion," *J. Opt. Soc. Am.*, **67**, 78-87.

Wang, J.Y. and Silva, D.E., (1980) "Wave-Front Interpretation with Zernike Polynomials," *Applied Optics*, **19**, 1510-1518.

Wilson, R.W., Baldwin, J.E., Buscher, D.F. and Warner, P.J., (1992) "High-Resolution Imaging of Betelgeuse and Mira," *Mon. Not. R. astr. Soc.*, **257**, 369-376.

Wyngaard, J.C., Izumi, Y. and Collins, S.A., (1971) "Behavior of the Refractive-Index-Structure Parameter near the Ground," *J. Opt. Soc. Am.*, **61**, 1646-1650.

Young, A.T., (1967) "Photometric Error Analysis. VI. Confirmation of Reiger's Theory of Scintillation," *Astron. J.*, **72**, 747-753.

Young, A.T., (1969) "Photometric Error Analysis. VIII. The Temporal Power Spectrum of Scintillation," *Applied Optics*, **8**, 869-885.

Young, A.T., (1970) "Saturation of Scintillation," *J. Opt. Soc. Am.*, **60**, 1495-1499.